Simulation of Ion Migration with Particle Dynamics and the Heat-Poisson-Nernst-Planck System

Dissertation

zur

Erlangung des Doktorgrades (Dr. rer. nat.)

der

Mathematisch-Naturwissenschaftlichen Fakultät

der

Rheinischen Friedrich-Wilhelms-Universität Bonn

vorgelegt von

Christian P. T. Neuen

aus

Bonn

Bonn 2016

Angefertigt mit Genehmigung der Mathematisch-Naturwissenschaftlichen Fakultät der Rheinischen Friedrich-Wilhelms-Universität Bonn

1. Gutachter: Prof. Dr. Michael Griebel

2. Gutachter: Prof. Dr. Jochen Garcke

Tag der Promotion: 18. November 2016

Erscheinungsjahr: 2016

Abstract

In this thesis we study the numerical simulation of ion migration and its coupled thermal effects. Many of the existing mathematical models in this area of research implicitly rely on thermal equilibrium conditions, despite the fact that the physical processes are almost exclusively driven by external influences, which move the ensemble away from equilibrium.

For the simulation to be self-sufficient and independent from experimental data for novel materials or structures, we adopt a multiscale approach. On the microscale we regard the dynamics of individual atoms and molecules using meshless particle dynamics methods in the form of non-equilibrium Molecular Dynamics. On the macroscale the ions are no longer considered individually, but as concentration functions, which are driven by an electro-chemical field. The resulting system of partial differential equations is known as the Poisson-Nernst-Planck equation system.

The basis of a Molecular Dynamics simulation is formed by the Hamiltonian function, from which conservation properties and the equations of motion for the particles are derived. For the first time we make use of the duality of work performed on a particle and its energy state to derive a formulation of the external energy, which allows for the inclusion of explicit external forces in the Hamiltonian function. The new approach is explicitly designed to also handle periodic boundary conditions and we further demonstrate that it can be combined with other variants of the Hamiltonian, such as those modeling thermostats and barostats. This approach allows for the exact computation of energy exchanged between the ensemble and its exterior, enabling us to compute the heat generated by the external forces on the atomistic scale, permitting the upscaling of a temperature source term to the macroscopic equations. For the measurement of the transferred heat we provide an a priori error estimate based on the transport properties. Measuring the transferred energy also allows for the detection of steady states in conjunction with other external effects such as thermostats.

On the macroscale we extend the Poisson-Nernst-Planck equation system by the heat equation, a constellation not present in the literature so far. We analyze the nature of the coupling between the different types of partial differential equations and consequently present a taylored discretization scheme based on the Finite Element method. For the first time we present a numerical solver for the extended Heat-Poisson-Nernst-Planck system with an arbitrary number of concentration functions and dynamic transport coefficients. Our implementation of this system allows for a variety of boundary conditions for all solution functions and the use a separate domain

(and finite element space) for the evolution of the temperature.

We demonstrate the capabilities of the methods on both scales on a series of numerical experiments. On the microscale we confirm the energy transfer and conservation as well as the consistency with thermostat applications. On the macroscale we determine the convergence rates for uniform, graded and adaptively refined grids. Final experiments include a well matching comparison with experimental results from an industrial application, sensitivity analysis of simulation parameters based on uncertainty quantification methods and a showcase for the solver capabilities on complex geometries.

Acknowledgements

At this point I would like to thank all those who accompanied and supported me in the completion of this thesis. I would like to thank my advisor Prof. Dr. Michael Griebel for the introduction into this exciting topic and the freedom which I enjoyed in pursuing it. I further thank Prof. Dr. Jochen Garcke for providing his opinion as the second referee.

I also thank BASF SE for permitting me to publish results from contract work in this thesis and also for providing me with experimental results for comparison.

My sincere gratitude goes towards my colleagues in the department Virtual Material design at the Fraunhofer SCAI for the comfortable working environment. Particularly I would like to thank my supervisor Dr. Jan Hamaekers for always keeping his door open and for his uncanny ability to drive a discussion by asking the right questions. I thank Ralph Thesen for keeping the computers up and running and also providing open ears when needed.

Special thanks go to Alexander Rüttgers for his feedback to parts of this thesis and the many hours of lunch which always were a bright spot during everyday work. I cannot express enough gratitude towards my wife Jutta, whose patience, encouragement and proofreading ability I taxed severely in the last several months. Last but not least I thank my friends and moreso my family for their constant encouragement in my pursuits but even more for making life enjoyable in the non-working hours.

Contents

1 Introduction

The process of ion migration has significant influence on our every day life, even if most people are not aware of it. Ion migration is not a visible phenomenon but its influence is exerted not only in diverse fields of science and technology but also in nature itself.

In biology and medicine, the transition of ions through protein channels or cell membranes is a process enabling the function of organs and signals in the nervous system and thus vital for life as we know it. The importance of this application is underlined by being the subject of the 2003 nobel prize in chemistry.

In material science, the removal or addition of ions from the material matrix may cause substantial changes to the properties of the respective material. Among others, it is known that the leaching of Calcium ions from cementitious materials degrades their stability, introducing a source of danger depending on the specific structure. Another application relying on ion fluxes is the process of electroplating or electrogalvanization, during which objects are coated by using them as an electrode in an ionic solution in order to protect them against oxidization effects.

Possibly most prominently in the public eye are batteries and capacitors which rely fundamentally on the regulated transfer of ions in electrolytes placed between different opposing electrodes. With the currently growing market of mobile electronic devices and the advent of personal electric vehicles, the performance and reliability of batteries becomes a factor in the day to day experience of many people.

Apart from personal comfort, batteries also play important roles as mobile and grid-independent power sources in control units of complex machinery. An example for the importance of understanding the phenomena surrounding ion migration in such systems are the incidents aboard the Boeing 787 Dreamliner in its first year of service through 2012/2013, leading to emergency landings, fires on the aircraft and other failures of electronic equipment[1]. The incidents, which led to the temporary grounding of all aircraft of this type, were caused by thermal runaway in the lithium ion batteries installed in the machines.

These incidents illustrate that ion migration processes are still not fully understood and they underline the exceptional value, which the qualitative description and the quantifiable prediciton of derived properties can have for many applications.

An important tool to access the relevant properties is the numerical simulation of the processes, which is able to reduce costs by replacing or aiding expensive laboratory

[1] For the official report on a single incident see [Nat14], for an overview [WHHP13].

experiments and in some cases may even allow for the investigation of processes on scales not accessible by experiments.

Besides providing additional understanding of process mechanics already observed in practice, the scope of numerical simulation is to aid in the improvement of technology by making predictions on the performance of novel configurations of parameters. The relevant parameters which characterize the performance of batteries can be measured on a continuous scale, where the ions are no longer regarded individually, but via a function of their spatial concentration. Consequently, the evolution of these functions is modeled by partial differential equations on what we will refer to as the continuous or macroscale, which require coefficients corresponding to the ion behavior. However, for new materials or innovative configurations, material or performance parameters are often not readily available and must be derived from underlying principles. This turns the path towards the independent simulation of ion migration into a multiscale problem, as the characteristics of the transport properties are determined by the particle kinetics on what we will call the atomistic or microscale.

While certainly providing more detail than the macroscopic equations, it is infeasible to perform the full simulation on the atomistic scale. Even small applications – such as consumer batteries – have a size of around 1 cm^3, containing a number of particles on the order of Avogadro's number, $6.022 \cdot 10^{23}$. Computation of the particle behavior for 1 second of real time would require at least on the order of 10^{38} floating point operations. With $2.5 \cdot 10^{15} \frac{\mathrm{flop}}{\mathrm{s}}$ available on currently leading superclusters, the required time is around 10^{15} years. This presents us with a slight problem, since the estimated remaining lifetime of our sun is only on the order of 10^9 years [SS08], leaving us unable to ever finish such simulations.

To cope with this dilemma, we need to take advantage of both, the atomistic micro- and the continuous macroscale, so that numerical simulations can sensibly contribute to further research on this topic.

Atomistic Scale

The basis of the atomistic simulations is formed by a Hamiltonian function, which determines the equations of motion and allows for access to conservation properties. As the migration of ions is driven by forces outside of the simulation domain, the ensemble can not be generally considered in equilibrium, thus non-equilibrium Molecular Dynamics must be employed. While external forces are present in several implementations of Molecular Dynamics, e.g. [SE00], they have not been incorporated into a Hamiltonian function so far. In order to address this issue, we will present a novel approach, which will make use of the work done on an individual particle to compute the change of external energy for each particle individually. This ansatz shows its merits as opposed to a coordinate based energy function when used in combination with periodic boundary conditions, as the resulting external energy is free of discontinuities which would violate the energy conservation. This allows for a consis-

tent quantification of the energy exchanged between the ensemble and external forces which we can combine with the energy exchanged with thermostats. Indeed we show that our extension to the Hamiltonian can be consistently combined with a selection of other existing non-equilibrium Hamiltonian functions which provide thermostats and a barostat.

In contrast to the continuous scale, Molecular Dynamics are based on a meshless approach. Thus we require special methods for the extraction of the relevant parameters for the macroscale from the particle trajectories. Fortunately, previous research already provides upscaling mechanisms for transport coefficients from the atomistic simulations [FS02]. Most of these upscaling equations make implicit equilibrium assumptions though, which are no longer valid for the dynamics just created. However, our new ability to quantify the energy exchange between the ensemble and its exterior will allow us to observe energy steady states. Under these steady state conditions, we will be able to utilize improved upscaling functions of transport coefficients which we previously presented in [Neu10] and also enable the computation of heat generated in the ensemble by convective ion migration on the microscale.

Continuous Scale

On the macroscale, the physical phenomenon of ion migration is mathematically decribed by the Poisson-Nernst-Planck equation system, a partial differential equation system, which takes the charge distribution of the ions as the sources and sinks of the electric field into account, while the electric field acts as a driving term of the ion convection. Apart from examples with only a single ion species which are artificially constructed for this exact purpose, this system of equations does not have any known analytical solutions.

Since the system of the Poisson-Nernst-Planck equations is at the heart of electrochemical energy storage simulations, the current interest in this and adjacent fields – such as electrical mobility – leads to perpetual advances in the art of solving the Poisson-Nernst-Planck equation system and its various extensions. These advances cover all approaches, such as extensions in modeling, model reduction, discretization and solution of the resulting linear equation system. While modeling of the temperature has been included in the literature for some time [LZ11], actual simulations of such models were only implemented for reduced phenomenological models [SDB$^+$13]. In physical systems the dynamic coupling of temperature and ion migration has been largely ignored up until recently, with the simulation generally expecting equilibrium conditions and constant temperatures. At the time of writing, only a single implementation of a physical model of such a coupling restricted to the two species case is known [LZ15]. In this thesis, we will address this issue by considering the system of the Poisson-Nernst-Planck equations, which model the diffusion and convection of an arbitrary number of ion species driven by both an electrical and a chemical potential in permeable material, coupled with the heat equation, which models the evolution

of temperature, together forming the Heat-Poisson-Nernst-Planck system. We will analyze the nature of the coupling between the different types of equations present and consequently present a taylored discretization scheme based on the Finite Element method. The resulting implementation will for the first time be able to solve the extended Heat-Poisson-Nernst-Planck system with an arbitrary number of concentration functions, where the domain of the heat equation may be extended beyond the domain of the ion migration system. Further capabilities of the solver include the simultaneous application of different boundary conditions, adaptive grid refinement and the use of dynamic transport coefficients. Based on the characteristic behavior of the solution functions we will also discuss the use of grids based on grading functions for suitable problems.

Contributions of this Thesis

At this point, we summarize the novel contributions of this thesis.

- We provide a new Hamiltonian formulation for arbitrary external forces in particle dynamics based on the individual particle trajectories and demonstrate the conformity of this new approach with several existing Hamiltonian thermostats and a barostat.

- We present formulae for the computation of the energy exchange between the ensemble and external contributions, which allow for the detection of energy steady states in non-equilibrium Molecular Dynamics simulations and the computation of heat transferred into the ensemble. Furthermore we provide an error estimate for the computation of convection velocity and external energy transfer.

- By modifying the software Tremolo-X [GKZC04, N$^+$16], we implement the computation of external work done on the particles and provide access to the relevant thermostat, external and total energy values. Tremolo-X is a Molecular Dynamics simulation software developed at the Fraunhofer Institute for Algorithms and Scientific Comuting SCAI (originally conceived at the Institute for Numerical Simulation, University of Bonn).

- We couple the extended Poisson-Nernst-Planck equation system for an arbitrary number of concentration functions with the heat equation and provide a discretization for the Heat-Poisson-Nernst-Planck system taylored to the nature of the coupling between the different types of equations.

- We implement a numerical solver for the coupled Heat-Poisson-Nernst-Planck system by writing a modular C++ program based on the Finite Element library deal.II [BHK07]. The solver is able to combine several different types of boundary conditions (Dirichlet, Neumann and Robin), perform adaptive grid

refinement, handle dynamic transport coefficients and operate on separate grids and Finite Element spaces for the different operators.

- We verify the performance of the above methods by a series of numerical simulations, in which we analyze the behavior against theoretical predictions, determine the convergence behavior on uniform, graded and adaptivily refined grids and successfully compare the numerical with experimental results. We also provide a sensitivity analysis of input parameters based on an industrial application.

Outline

The remainder of this thesis is organized as follows. We begin in chapter 2 by presenting the foundations and the current state of non-equilibrium Molecular Dynamics before we introduce our new modifications of the underlying Hamiltonian function. These modifications include possibly non-constant external forces via the work done on the individual particles and allow for the computation of external energy contributions. The chapter continues to demonstrate the conformity of the new approach with traditional thermostats and the Parinello barostat.

Chapter 3 is dedicated to the extraction of macroscopic parameters from the scale of Molecular Dynamics. We match the microscale behavior to the macroscale equations and discuss upscaling functions for transport coefficients with special emphasis on non-equilibrium corrections. The heart of this section is the discussion of the behavior of external energy contributions and the estimate on the error in measuring this variable. Furthermore we discuss the upscaling of heat/temperature generation and the possibility of steady state detection by observing the energy from external forces and thermostats at the same time.

The following chapter 4 considers the macroscopic Heat-Poisson-Nernst-Planck equation system. We introduce the modeling of the separate equations and discuss the differences in coupling between the three different types of equations before constructing a discrete representation using Finite Elements. On the basis of the different coupling properties, we construct a solver method treating the Poisson-Nernst-Planck system fully implicitly, while separating the heat equation for explicit treatment.

The theoretical results of the previous chapters are put into practice in chapter 5. We begin the chapter by observing the transfer of external energy into test ensembles with increasing complexity before finally applying external forces to physical examples. We then switch to the macroscopic system, where we analyze the coupling of the equations in dependence on the input variables. After a short comparison with an analytical approximation, we continue to an extensive study of convergence properties, where we also investigate the merit of graded grids and adaptive treatment of the solution. We present an industrial application for which we compare the numerical with experimental results and perform a sensitivity analysis on the relevant input pa-

rameters based on uncertainty quantification methods. The chapter is concluded with a demonstrator for problems in higher dimensions with multiple species on complex, non-matching grids and varying boundary conditions.

The last chapter 6 is reserved for a summary of this thesis and an outlook into possible extensions based on this work.

2 Molecular Dynamics

Within the domain of material simulation, many material properties are inherently dependent on nanostructures and nanoprocesses on a spatial scale which is no longer sufficiently described by continuum models. When the scale shrinks to the size of several nanometers (or nowadays beginning at the size of micrometers) Molecular Dynamics (MD) methods can be employed to simulate these structures and consequently predict the macroscopic properties.

The correct computation of the ensemble and the derived properties often relies on the assumption that the ensemble is in equilibrium, facilitating proper averaging over the particles and the time. However, for many processes this is a significant restriction, as researchers are often interested in the dynamic behavior of systems. Indeed, even before the term Molecular Dynamics was actually introduced into the literature, the original idea of the method was to get away from equilibrium requirements, but practical applications have long been restricted to such equilibrium ensembles [AW57, AW59].

Since then, significant results have been achieved with respect to the control of the kinetic energy and pressure of the system, however results for other external influences remain sparse. We will address this issue by introducing a scheme to treat arbitrary external forces on the particles, providing a Hamiltonian function for such systems and computing the external energy contributions.

We will begin this chapter by giving a brief introduction into Molecular Dynamics and elaborate on several aspects which will be relevant for the extension of non-equilibrium dynamics, such as statistical analysis of properties, ensembles and integrators. We continue with a short reference to previous work on non-equilibrium MD before presenting our treatment of external forces in Hamiltonian dynamics. We will derive a new formulation based on energy observations for individual particles for both Lagrangian and Hamiltonian mechanics and show the consistence of the new formulation with several existing thermo- and barostats.

2.1 Overview of Molecular Dynamics

This section is dedicated to the introduction of key concepts in Molecular Dynamics, which are relevant both in equilibrium and in non-equilibrium dynamics. We will give a short overview of concepts in Molecular Dynamics and considerations for limits in their application. Many different settings have been developed to tailor the simulation

to diverse target applications, and the large number of possible combinations of individual methods – as well as variations of the base methods – prevent us from giving an exhaustive account without going beyond the scope of this work. Nevertheless we endeavour to grant the reader an overview of the state of the art for the methods which will be used and expanded in this thesis.

To begin with, we place Molecular Dynamics in context with the scales below and above and sketch the derivation of Hamiltonian Molecular Dynamics from quantum mechanics. We continue with the relation of the microscopic states with the macroscopic variables and provide a list of statistical ensembles together with their constant macrostates. We will also mention variants of these statistical ensembles, which often lead to forms of non-equilibrium simulations. We continue the description with considerations of boundary conditions and their impact on the simulation behavior, before we turn to the choice of time integration algorithms. Prudent selections can guarantee that – despite numerical inaccuracies – the theoretical virtual entirety introduced in this section is conserved, while they may also allow the mathematical time reversibility of the simulation.

2.1.1 Derivation of Hamiltonian Dynamics

The goal of Molecular Dynamics is the simulation and ultimately the prediction of material properties on the atomistic scale of the material. Molecular Dynamics have their place in the simulation of material properties between the lower scaled quantum mechanical (QM) simulations and the larger scaled coarse grained particle methods or even continuum methods, see figure 2.1.

While the trajectories of atomic particles will generally only be subject to quantum effects under extreme conditions (consider Bose-Einstein condensates [Fal01]), their interaction is dependent on the behavior of their respective electrons, which are generally described by the Schrödinger equation. The complexity of this equation makes it impossible to obtain analytical solutions for any but the most simple and artificial systems. The degree of restriction becomes immediately apparent by considering that there are closed solutions for the description of a single Hydrogen atom, but already two electron atoms (or ions), such as the Helium atom, have no known analytical solution.

In extension to the difficulty with analytical solutions, numerical solutions are subject to several challenges and demand a large amount of computational ressources. This is due to the fact that, even under the Born-Oppenheimer assumption, the wave function of each electron requires a three dimensional solution space. If for a system of N electrons for each space dimension m degrees of freedom are used the resulting system would have $O(m^{3N})$ degrees of freedom[1]. Given that a sensible computation

[1] To give an exact example [Lub08]: The molecule CO_2 has 3 nuclei and 22 electrons, so that the wave function has the domain $\mathbb{R}^{75}$.

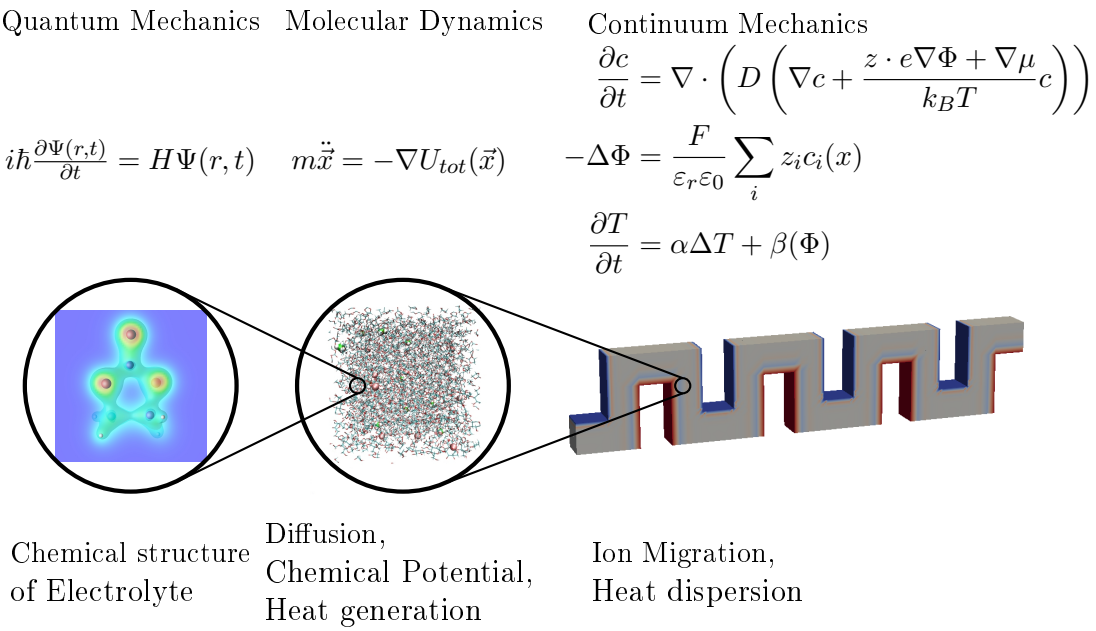

Figure 2.1: System equations on multiple states.

of material properties rather requires tens of thousands of atoms (which each have multiple electrons), it is obvious that this places us in the domain of the so-called curse of dimensionality. To cope with this curse, sparsity-based approaches exist [Ham09], which reduce the requirements on degrees of freedom, but they are still far from bringing real-world problems into the reach of quantum mechanical solutions.

These complications with the complete description of atomic materials give rise to the classical Molecular Dynamics. While the derivation can be rooted in the time dependent Schrödinger equation with the electronic Hamilton operator for atom nuclei and their associated electrons, the equations actually integrated for the time progression of the system are Newton's equations of motion.

This transition between QM and MD can be generally justified by the Ehrenfest theorem [Ehr27], which relates the acceleration of (the expectation value of the position of) a wave package with wave function Ψ by a field U to Newton's laws of motion

$$m\frac{d^2}{dt^2}\int \Psi x \bar{\Psi} d\tau = \int \Psi \left(-\frac{\partial U}{\partial x} \right) \bar{\Psi} d\tau. \tag{2.1}$$

for masses m of the order of 1g. Although this result is exact, these expectation values are accompanied by an uncertainty, the "width" of the wave package. This uncertainty will evolve in time and Ehrenfest himself gave the examples for the uncertainty evolution of an unaccelerated particle with initial mass m and original wave

function

$$\Psi(x, t = 0) = c \cdot e^{-\frac{x^2}{2\omega^2} + \imath\mu x},$$

where x is the space variable, ω determines the original width of the wave package, μ is an arbitrary real constant and c is chosen s.t. the square integral is normalized. Then the evolution of the uncertainty of the particle position is determined by its mass and original uncertainty; for $m = 1\text{g}$, $\omega = 10^{-3}\text{cm}$ the original width doubles after $T = 10^{21}\text{s}$, while for $m = 1.661e^{-24}\text{g}$ (the mass of a hydrogen atom) and $\omega = 10^{-8}\text{cm}$ we have $T = 10^{-13}\text{s}$.

While the latter result, indicating fast increasing uncertainty, might seem discouraging at first, it must be looked at for what it really is. We learn that no matter how accurate we compute the trajectories of the particles, we are confronted with an underlying uncertainty, which increases with the progression of time. As a result we can accept the accumulating numerical errors in the individual trajectories – which we discuss in section 2.1.5 – with more ease, knowing that the time at which this uncertainty doubles is clearly in the range of numerical Molecular Dynamics simulations.

We do not intend to give a full derivation here, as this would be beyond the scope of this thesis. More elaborate derivations are available in [Lub08, GKZC04]. Nevertheless, we will outline the key assumptions and their respective consequences for the method of MD.

We begin by writing the Hamilton operator H_{mol} for molecular systems for L_N nuclei (whose associated variables we will denote with the index N) of masses m_l and electric charges $z_l e$ at positions $x_l \in \mathbb{R}^3$ and L_e electrons (whose associated variables we will denote with the index e) of mass m_e and charge $-e$ at positions $y_l \in \mathbb{R}^3$. Let

$$\mathcal{H}_{mol} = T_N + T_e + V_{NN} + V_{Ne} + V_{ee},$$

where T_i is the operator for the kinetic energy of nuclei and electrons, respectively,

$$T_N = -\sum_{l=1}^{L_N} \frac{\hbar^2}{2m_l} \Delta_{x_l} \qquad T_e = -\sum_{l=1}^{L_e} \frac{\hbar^2}{2m_e} \Delta_{y_l} \tag{2.2}$$

and the potential summands are given by

$$V_{NN}(x) = \sum_{1 \le k < l \le L_N} \frac{z_k z_l e^2}{\|x_k - x_l\|} \qquad V_{ee}(y) = \sum_{1 \le k < l \le L_e} \frac{e^2}{\|y_k - y_l\|} \tag{2.3}$$

$$V_{Ne}(x, y) = -\sum_{1=k}^{L_e} \sum_{1=l}^{L_N} \frac{z_l e^2}{\|y_k - x_l\|}. \tag{2.4}$$

The fundamental step towards Molecular Dynamics is the so-called Born-Oppenheimer approximation, which separates the treatment of the nuclei and the electrons.

This separation is motivated by the difference in mass between the nuclei and electrons (a single proton/neutron is more than 1800 times heavier than an electron), which gives rise to two distinct differences in behavior. First, in light of the discussion following the Ehrenfest theorem (2.1), we note that the uncertainty of the wave function associated with an electron decays faster than that of a nucleus, the "half-life" of the uncertainty scaling linearly with the mass of a particle. Second, we note that for equal acting forces the acceleration and – via integration – the velocities and positions of the electrons change much more rapidly than those of the nuclei.[2]

As a consequence, the computations of the trajectories can be decoupled and it can be assumed that the state of the electrons follows those of the nuclei instantly, while those serve as background parameters to the electronic structure problem. This leads to the electronic Hamiltonian

$$\mathcal{H}_e(x) = T_e + U(x, \cdot)$$

which is then used to write the time dependent Schrödinger equation

$$\imath\hbar\frac{\partial\Psi_e}{\partial t} = \mathcal{H}_e(x)\Psi_e$$

with the imaginary unit $\imath$, the reduced Planck constant $\hbar = \frac{h}{2\pi}$ and the electronic wave function Ψ_e. Note that the right hand side is not explicitly dependent on time[3], leading to the general separation ansatz

$$\Psi_e(x, y, t) = f(t) \cdot \psi(x, y).$$

Via the time independent Schrödinger eigenvalue problem

$$\mathcal{H}_e(x)\psi(x, y) = E_i(x)\psi_i(x, y),$$

we can compute eigenvalues E_i and corresponding eigenfunctions ψ_i of the electronic Hamiltonian. Consequently, we obtain for the time evolution

$$f(t) = e^{\frac{-\imath E_i(x)t}{\hbar}},$$

which allows us to write the final solution as a superposition of eigenfunctions

$$\Psi_e(x, y, t) = \sum_i c_i \cdot e^{\frac{-\imath E_i(x)t}{\hbar}} \cdot \psi(x, y).$$

[2] Note that analogies to kinetic theory of gases, which are given by some authors [GKZC04], are not applicable here, specifically because of their large difference of mass and even more so because they interact via the electric potential, which is not only repulsive but also attractive between electrons and nuclei.

[3] There is an implicit time dependence of the operator via the coordinates of the nuclei. However, in this form there is no explicit time dependence as might be caused by external forces, a topic which we will discuss in 2.3.

We will not delve into solving this equation, but from now on assume that we have a solution to this equation available, for example by the means described in [Ham02, Ham09]. For the practical implementation, the results of the electronic Schrödinger equation are used to fit particle potentials to the respective position of the nuclei. There are several compilations of tables of such potentials, some of which have been developed for a very specific task [LWW06, MEA07], while others are applicable to a variety of applications with common setting [CCB+95].

With this solution we can now write the Schrödinger equation for the nuclei as

$$\mathcal{H}_N = T_N + U(x), \tag{2.5}$$

where T_N is the kinetic operator of the nuclei as in (2.2) and $U(x)$ is the evaluation of the potential energy of the nuclei positions in the state given by the electron wave function Ψ_e. Application of the Ehrenfest theorem (2.1) then yields Newton's equations of motion for the expected values of the location observables

$$m_n \ddot{x} = -\nabla_x U(x),$$

allowing the computation of the trajectories of the nuclei in the classical sense. With the Born-Oppenheimer approximation we expect the electrons to follow the motion of the nuclei instantly and can regard the trajectories of the nuclei as trajectories of the combined atom. By applying the correspondence principle established by the Ehrenfest theorem, we can replace the operators in equation (2.5) with their expectation values and obtain the classical Hamiltonian

$$\mathcal{H} = \sum_i \frac{\vec{p_i}^2}{2m_i} + U(\vec{x}), \tag{2.6}$$

where $\vec{p_i}$ is the impulse of particle i. The dynamics of the system are then described by the so-called Hamilton's equations of motion

$$\dot{x}_i = \frac{\partial}{\partial p_i}\mathcal{H} \qquad \dot{p}_i = -\frac{\partial}{\partial x_i}\mathcal{H}.$$

With this last step we have derived the fundamental equations of Molecular Dynamics from a lower scale, obtaining the particle potentials by solving the electronic Schrödinger equation. The individual trajectories of the particles, which may be computed from these equations, can then be taken as the basis for the computation of further results, which we will elaborate in the next section.

2.1.2 Statistical Analysis of Properties

While Molecular Dynamics compute the trajectories of many individual particles (atoms), generally the number of degrees of freedom involved means that a change in

a single or a few degrees of freedom does not have a significant impact on the macroscopic properties of the system. As a consequence, we are generally not interested in the detailed coordinates[4], which we will call the microstates of the system. Rather it is our objective to compute parameters which provide the respective macroscopic description and which represent the status of the ensemble in bulk by deriving them from the respective individual degrees of freedom. Hence, we will call such a property a macrostate[5].

Nevertheless, such individual "snapshot" properties are of questionable use, as the macroscopic properties may fluctuate around their actual value and individual measurements may be arbitrarily placed within the fluctuation corridor. Even worse, some macroscopic properties may not be in equilibrium or steady state with respect to the starting point of the ensemble and as a consequence the value will change qualitatively during the simulation time. For these reasons, it is necessary to take multiple values into account and analyze the overall behavior of the measurements. For the purpose of sensible statistics on the results of the ensembles, we will now discuss several aspects which influence the averaging operations, starting with the space in which we observe the ensemble.

Given a system of N particles, we can observe 3 degrees of freedom for the generalized position and 3 degrees of freedom for the generalized velocity of the particle, resulting in $6 \cdot N$ degrees of freedom. These degrees of freedom completely define the *current* state of the ensemble and thus we may interpret the vector of these degrees as a point in a $6 \cdot N$ dimensional space, which we call the phase space. Each point corresponds to a snapshot of the microscopic properties of the ensemble, often also referred to as a microstate. As the ensemble evolves in time, its microstate changes and traces a path through the phase space which we call a trajectory.

If we have points, which differ in their microstates but share one or more common macroscopic properties (e.g. a fixed volume), they are said to be in the same macrostate. We will be interested in areas of the phase space in which a particular macrostate is constant, thus coupling several of the original degrees of freedom[6]. The corresponding manifold is the *virtual entirety*[7] Γ. For certain sets of macroscopic properties, the Hamilton function describing the ensemble is independent of time. In these cases, the trajectories of the ensemble can never leave the virtual entirety, the respective macrostate is constant. Such ensembles are also known as statistical

[4] Furthermore, the prediction of individual particle behavior is prone to errors, which accumulate over large runtimes of a simulation, see section 2.1.5.

[5] An intuitive example for such a property is the temperature of the ensemble, as it is defined via the mass-weighted average of the squared velocities of all particles $T = \frac{2}{3k_B} \sum_i m_i \vec{v}_i^2$; however, there are also more elaborate relations.

[6] As a result, some specific microstates may no longer be accessible.

[7] Virtual entirety is the author's translation of the German phrase *virtuelle Gesamtheit*, which does not seem to have an equivalent expression in the English language.

ensembles. This allows us to use the virtual entirety as the sample space for further investigation of macroscopic values, which are not fixed by the respective macrostate. (Consider as an example the NVE macrostate with the temperature as a measurable macroscopic value.)

Additionally, we define a probability density

$$f_{N,\Gamma} : \mathbb{R}^{3N} \times \mathbb{R}^{3N} \to \mathbb{R}$$

for an N particle ensemble within the virtual entirety Γ, where

$$P(I) = \int_I f_N(\vec{q}, \vec{p})\, d\vec{p}\, d\vec{q}$$

denotes the probability that a physical ensemble is in the subset $I \subset \Gamma$. Under the assumption that this function is available, the prediction of a macroscopic value A under the macrostate Γ would be computed by

$$A_\Gamma := \frac{\int_\Gamma A(\vec{p}, \vec{q}) \cdot f_{N,\Gamma}(\vec{p}, \vec{q})\; d\vec{q}\, d\vec{p}}{\int_\Gamma f_{N,\Gamma}(\vec{p}, \vec{q})\; d\vec{q}\, d\vec{p}}, \tag{2.7}$$

which corresponds to the weighted average of the respective variable.

Unfortunately, the probability densities of the macrostates are for all practical purposes impossible to obtain for complex systems [FS02]. Nevertheless, predictions are possible via the time average

$$\langle A \rangle_T := \frac{1}{T} \int_{t_0}^{t_0+T} A(\vec{q}_{q_0}(t), \vec{p}_{p_0}(t)) dt,$$

where the indices q_0 and p_0 indicate the dependence of the trajectories on the starting condition. The validity of the time average is derived from the ergodic hypothesis [GKZC04, HFPH95], which states that the time average on the one hand and the average computed via the probability density (2.7) on the other hand are equal as $T \to \infty$.

This equality implies two significant facts, first that the initial state of the system is irrelevant with respect to the average macroscopic values and second that the probability of a system trajectory passing a specific point of the phase space correlates with the probability density of the respective point.

However, the application of the ergodic hypothesis has obvious limitations. Since in computational reality the time T can never be infinite, we must use some finite time not knowing, whether the sample obtained by the trajectory is sufficient. Indeed, for finite trajectories the initial state of the system may have a significant impact on the average computation.

2.1.3 Statistical Ensembles

Statistical ensembles are generally defined by the control of three macroscopic variables, which determine the constant macrostate of the virtual entirety. At times, statistical ensembles are abandoned in favor of controlled interventions into the progression of the macrostates. In these cases, the ensembles are no longer in equilibrium, but purposefully moved to a new state. While the use of such methods is relatively common, they are seldomly backed up by corresponding conclusions for the validity of their results. We will mention some examples of such control, and the purpose to which they are applied.

The most basic ensemble is the microcanonical ensemble (NVE), for which the variables particle **N**umber, **V**olume and total **E**nergy are fixed. In its basic setting, the system is completely isolated from outside influences and has its own contained equilibrium. However, it is also possible that the volume or shape of the simulation domain is directly controlled, introducing strain into the ensemble [Gal97]. This artificial introduction of strain allows us to perform targeted computations of elasticity properties of materials.

A popular enforced macrostate is the canonical ensemble (NVT). Again number of particles and volume are constant, but instead of the total physical energy the kinetic energy is controlled in NVT ensembles. For the control of the temperature many different schemes have been established, ranging from simple scaling of the velocities, via Hamiltonian-based Nosé-Hoover thermostat to stochastic thermostats. Despite their difference in practice, they all share the same general idea, that the ensemble is placed in contact with an external thermal bath and that the combined system equilibrates. The properties of different thermostats have been extensively researched [GH06], some of which we present in section 2.2.2. At times the external heat bath is not kept constant, but controlled. In this case, the equilibration between the two ensembles is broken and needs to be reaquired, another example of a non-equilibrium setting.

In the isobaric ensemble (NPE) the control of the volume is released and replaced with the control of the pressure of the ensemble. As a result the simulation domain may be deformed by the internal stress. These deformations may be free but are generally subject to constraints, which allow only limited degrees of freedom of the simulation domain to change. In addition to the common pressure, the stress tensor of the ensemble may also be specified. An often used combination is the isobaric-isothermal ensemble (NPT), combining the pressure and temperature control. Despite its complicated mechanics, this ensemble may also be described by Hamiltonian dynamics [GH06].

Finally, we mention the grand canonical ensemble (μVT), which does not keep the number of particles but the chemical potential constant. This ensemble cannot be used with classical Molecular Dynamics methods, but is generally used with Monte Carlo-based methods. Moreover, certain hybrid methods make use of this ensemble

as well.

Since the canonical and isobaric ensemble have variants which lead to Hamiltonian dynamics, we will discuss these in more detail in section 2.2.2.

2.1.4 Boundary Conditions

At this point we would like to present further considerations for challenges of Molecular Dynamics computations, namely the difference between surface and bulk properties.

General choices for boundary conditions in Molecular Dynamics are free, periodic and hard wall boundaries. Hard or heated wall boundaries would again impact the ensemble, as they provide outside interaction with an imaginary potential, which cannot be penetrated by the particles. In the case of free boundary conditions all particles on the rim of the simulated ensemble would behave as being on the surface of the material towards vacuum, while conversely periodic boundary conditions would present bulk material without any surface.

The importance of the choice of boundary conditions becomes apparent when we imagine the ratio of bulk to surface particles. If the ensemble consists of 10^3 particles which are distributed roughly uniformly throughout a cube, 48.8% of these particles would be on the direct surface of the material – not even counting those particles which are in the "second layer", which may also experience particular surface effects. When we consider an ensemble with 10^6 particles, the ratio of surface particles goes down to 6%. In real materials however, where the number of particles is of the order of Avogadro's number $6.023 \cdot 10^{23}$, the ratio of particles on the surface is of the order of 10^{-16}. Thus, in most practical applications periodic boundary conditions are best suited to produce relevant results, while the other boundary conditions are only considered in special applications. In this thesis we will consider periodic boundary conditions exclusively and in our implementation of external forces we will specifically deal with problems only encountered with periodic boundary conditions.

2.1.5 Time Integrators

One of the most important choices when performing MD simulations is the technique for time propagation, usually referred to as the time integrator. Considering the particle system as a system of coupled ordinary differential equations, a multitude of numerical solver methods is available to choose from. The choice of the solver has several far reaching consequences, among which are the order of the numerical and systematic error, the regard of conservation properties, reversibility, and adherence to the expected solution space.

Since this numerical system is a representation of a physical system, we have advanced knowledge of some of the structure of the solution space and furthermore can formulate expectations towards conservation properties and tolerance for error.

Error Propagation

In this section we will establish the error of the individual particle trajectories for arbitrary integration schemes. Error estimates for macroscopic variables will behave very differently and need to be established for each constructed variable individually. The difference is of paramount importance, as the resulting errors for macroscopic variables will actually show convergence over the time of the numerical simulation, while we will show that the errors in the trajectories of the individual particles accumulate over time, as already mentioned in 2.1.2.

We consider an arbitrary numerical updating scheme for the positions and velocities of the particles

$$\begin{pmatrix} x^{n+1} \\ v^{n+1} \end{pmatrix} = \begin{pmatrix} \Theta_x(x^n, v^n, \delta t) \\ \Theta_v(x^n, v^n, \delta t) \end{pmatrix},$$

where x^{n+1} shall be an approximation of the true progression of the position $x(t^n + \delta t)$ and v^{n+1} an approximation of the true progression of the velocity $v(t^n + \delta t)$.

If Θ is a numerical scheme of order m, we can reduce the error for a single time step arbitrarily

$$\begin{aligned} \|x^{n+1} - x(t + \delta t)\| &= \mathcal{O}(\delta t^{m+1}) \\ \|v^{n+1} - v(t + \delta t)\| &= \mathcal{O}(\delta t^{m+1}). \end{aligned}$$

While the constants involved may vary, they can be easily dealt with. This is a different matter for the global error over multiple time steps. Let $T = n \cdot \delta t$. Then we obtain the usual error estimate for explicit integrators, compare [LM15],

$$\|x^n - x(T)\| \leq C(T) \cdot \delta t^m,$$

where the constant $C(T)$ is independent of the number of steps n or the step size δt. However, it is not independent on the time domain covered by these steps, and we can obtain an estimate

$$C(T) \leq C' \cdot e^{C'' \cdot T}$$

which is exponentially dependent on the time domain T [GKZC04, BL07]. Small deviations of the starting conditions thus have to be expected to have a considerable impact on the final state of the simulations for long runtimes. In practical Molecular Dynamics applications the simulation times have indeed to be long, and the reasonable question raised by this fact is whether macroscopic variables are influenced as well. Fortunately, this question can be answered negatively, which we will outline in the following section.

Symplecticity and Reversibility

In section 2.1.3, we introduced the notion of macrostates and the virtual entirety which constrain the system of simulation. Given the numerical inaccuracies described in the previous section, it is a non-trivial question, whether the restraining macrostates are conserved by the numerical algorithms. The trajectories of the phase space satisfy the conservation property that the volume between a collection of trajectories remains invariant. Numerical integrators whose solutions satisfy the same property are called symplectic, and via backward error analysis they can be interpreted as exact solutions to distorted variants $\tilde{\mathcal{H}}$ of the original Hamiltonian $\mathcal{H}$. This interpretation results in a guarantee for the existence of the respective ensemble averages and for the non-accumulation of the inaccuracies of the trajectories in the macrostate measurements [GKZC04].

However, for the original macroscopic value A the corresponding value $\tilde{A}$ may also be distorted, introducing a different kind of error, which varies with the ensemble and the integrator used. Indeed more recent results determine that even for non-symplectic integrators, error estimates for trajectory averages can be constructed [BL07] which may have advantages depending on the exact setting in question. Specifically, the class of time reversible integrators has proven to be a viable alternative to symplectic numerical schemes. In special cases, time reversible integrators are still able to yield sensible results, even when the backwards analysis is no longer possible due to the large time step [GKZC04].

The above descriptions have generally been provided with equilibrium systems in mind. Nevertheless, both of these properties may also be transfered to non-equilibrium dynamics as long as certain conditions are fulfilled. While reversibility is a property of the integrator and only dependent on the symmetric processing of the integration variables, for the case of symplecticity the form of the Hamiltonian has to be considered. As long as it is not explicitly dependent on time, the volume preservation of the phase space may be proven as before by Liouville's theorem.[8] Finding proper integration schemes is another matter and must be established from ensemble to ensemble. Examples for such constructions for popular externally coupled systems can be found in [BLL99, GH06].

2.2 Current State of Non-Equilibrium Hamiltonian Dynamics

In the application of MD to material science, it is common to control other macroscopic variables than the particle number, volume and total energy, and to have more

[8] In fact, the Liouville equation, which is the basis of this theorem, is also an integral part in proving the fluctuation theorem, which allows our discussion of validity of non-equilibrium Molecular Dynamics in section 2.2.3.

influence than to keep these properties constant. Examples of this may be either a manual control of the volume and shape of the simulation domain (corresponding to the physical variable strain), the temperature or the pressure.

As a result of this control of macroscopic properties, work is done on the ensemble, which violates the equilibrium property of the simulation. This violation puts the ergodic hypothesis into question, which is the foundation of the determination of macroscopic physical properties via time averages.

In this section we will present different non-equilibrium settings and examine whether they have certain steady state properties. We will pay specific attention to Hamiltonian-type systems and the analysis they allow, specifically with respect to external forces. Furthermore, we will review the fluctuation theorem and its consequences for the interpretation of data generated by numerical simulation in light of the second law of thermodynamics.

2.2.1 Equilibrium vs. Steady State

Measurements carried out in equilibrium conditions in Molecular Dynamics are generally well researched and established [GKZC04, Tuc10]. With external restrictions and contraints, ensembles deviate from models which are solely based on internal physical equations. Nevertheless, those play an important role in the application of Molecular Dynamics, as they enable measurements and observations of phenomena which would otherwise be beyond the scope of such simulation.

Moreover, such ensembles can be described in terms of modified equations, which enable the analysis of the behavior in contrast to the pure physical description. One such example is the Parrinello barostat, which is often used in NPT ensembles. For this barostat, it is possible to derive a modified Hamiltonian, which allows for the computation of different but similar conservation laws [GH06].

However, when the ensemble is not in equilibrium, results for the accuracy and validity of measurements are sparse [Tuc10]. Statistical analysis for systems in flux is quite different and some results simply do not carry over from the analysis of equilibrium conditions, such as the application of auto-correlation functions [NGH12], which we also discuss in section 3.3.

With this in mind, we will investigate the influence of external forces on Molecular Dynamics ensembles.

Steady State with Tempered Color Field

Non-equilibrium steady states can be established in different ways and must not necessarily be derived from a Hamiltonian. In a non-physical example placed in a Lorentz gas[9], particles are subjected to a constant "color field", where the color charge

[9] The terminology "Lorentz gas" does not describe the particle system but the domain in which

given to the particles determines their direction of acceleration. To enable a steady state, the particles are tempered by a force proportional to their deviation from a given constant flux. This work shows the influence of the established convection on the diffusion of the parameters. The measurements of the diffusion coefficients are indeed properly modified to address convection and the velocity auto-correlation functions are not used in the presence of the field. However any theoretical discussion of the employed methods is absent [BEC93].

While this work lays good foundations for the implementation of several measurement functions, it does not properly discuss how the achievement of a steady state is controlled. The general goal of achieving a steady state, however, sets it apart from the following section, where the steady state is ignored while the focus is on modifications of the Hamiltonian function.

2.2.2 Previous Examples of Modified Hamiltonians

In section 2.1.3 we discussed the existence of various different ensembles, which each refer to the control of different macroscopic variables (generally meaning that these properties are kept constant). There are several realizations of Molecular Dynamics which already rely on successfully modified Hamiltonians. The common aspect of all instances is that the system is not closed in itself, but interacts with some form of outside "system". Generally, this interaction is enforced to gain control over a new macroscopic parameter of the original system and consequently to establish the previously in section 2.1.3 mentioned ensembles.

In the following, we will give a short review of established modifications and the macroscopic properties to which they relate.

Note that not all external interactions (and specifically not all implementations of ensembles) can be described by a Hamiltonian. In particular, the implementation of the canonical NVT ensemble via the Berendsen thermostat in its general case cannot be derived from a Hamiltonian formulation.

Nosé-Hoover Variant of Hamiltonian

As noted above, not all choices of thermostat implementations for the canonical NVT ensemble can be related to a Hamiltonian function. At the same time, the so-called Nosé-Hoover variant of the Hamiltonian [Nos84] is possibly the best-known variant to the standard Hamiltonian encountered in Molecular Dynamics. The standard Hamiltonian (2.6) is modified by a time scaling function, which in turn yields a coordinate transformation for the canonical impulses, which then no longer equal the physical

it is placed. The exact layout varies, in the described source it consists of three fixed hard-disk "scatterers" placed in a triangular pattern. While not stated in the paper itself, the referenced source therein indicates periodic boundary conditions [MZ83].

impulses of the particles. The modified Hamiltonian

$$\mathcal{H}_{\text{Nosé-Hoover}} = \sum_i \frac{\vec{p}_i^2}{2m_i s^2} + U(\vec{q}) + \frac{\pi^2}{2Q} + gk_BT\,\ln(s) \tag{2.8}$$

requires the introduction of the timescaling function s, the fictitious "mass" Q of the external heat reservoir and the kinetic energy of the reservoir π. Further, g denotes a constant equalling the number of degrees of freedom of the original system plus one ($g = 3 \cdot N + 1$). The variables s and π form a new conjugate pair of variables, with s taking the role of a coordinate and π taking the role of a momentum variable. As such, we consider the vectors

$$\begin{pmatrix}\vec{q}\\ s\end{pmatrix}, \begin{pmatrix}\vec{p}\\ \pi\end{pmatrix}$$

for Hamilton's equations of motion. While the modifications yields a new conserved quantity often referred to as the extended energy, the equations of motion

$$\begin{aligned}
\frac{\partial q_i}{\partial \tau} &= \frac{\partial \mathcal{H}}{\partial \tilde{p}_i} = \frac{\tilde{p}_i}{m_i s^2}, & \frac{\partial s}{\partial \tau} &= \frac{\partial \mathcal{H}}{\partial \pi} = \frac{\pi}{Q},\\
\frac{\partial \tilde{p}_i}{\partial \tau} &= -\frac{\partial \mathcal{H}}{\partial q_i} = -\frac{\partial U(q)}{\partial q_i}, & \frac{\partial \pi}{\partial \tau} &= -\frac{\partial \mathcal{H}}{\partial s} = \sum_i \frac{\tilde{p}_i^2}{m_i s^3} - gk_BT\frac{1}{s}
\end{aligned} \tag{2.9}$$

however are with respect to a scaled time variable which in practical applications leads to non-equally spaced points on the timeline. By introducing a scaling of the impulse variables and a so-called Sundman time-transformation, real-variable equations of motion can be established, but they are non-Hamiltonian in nature due to the non-canonical time scaling [BLL99].

Nosé-Poincaré Variant of Hamiltonian

A remedy to this problem is presented in the same paper, by extending the Hamiltonian to the so-called Nosé-Poincaré Hamiltonian

$$\mathcal{H}_{\text{Nosé-Poincaré}} = \left(\sum_i \frac{\vec{p}_i^2}{2m_i s^2} + U(\vec{q}) + \frac{\pi^2}{2Q} + \tilde{g}k_BT\,\ln(s) - \mathcal{H}_0\right) s. \tag{2.10}$$

Apart from the obvious changes, the degrees of freedom are reduced by one ($g = 3 \cdot N$) and the time variable is the correct physical time t. Consequently, we obtain equations of motion in the true time system

$$\begin{aligned}
\dot{q} &= \frac{\tilde{p}_i}{m_i s}, & \dot{s} &= s\frac{\pi}{Q},\\
\dot{\tilde{p}}_i &= -s\frac{\partial U(q)}{\partial q_i}, & \dot{\pi} &= \sum_i \frac{\tilde{p}_i^2}{m_i s^2} - gk_BT - \Delta H
\end{aligned} \tag{2.11}$$

with

$$\Delta H := \sum_i \frac{\vec{p}_i^2}{2m_i s^2} + U(\vec{q}) + \frac{\pi^2}{2Q} + \tilde{g} k_B T \ln(s) - \mathcal{H}_0.$$

For both of the above variants reversible integrators are available, but only for the latter symplecticity may be achieved. In section 2.3.4 we will demonstrate that our handling of external forces can be integrated in these thermostat formulations, making previous implementations of integrators easily convertible.

Parrinello-Rahman Variant of Hamiltonian

The control of the pressure of the system can be achieved via the so called Parrinello-Rahman barostat, which requires further changes to the Hamiltonian. Similar to the fact that the temperature is controlled via the scaling of time, the control of the pressure is achieved via the scaling of the coordinates. The coordinate scaling is performed in terms of the simulation domain, so that for vectors $\vec{a}_1$, $\vec{a}_2$ and $\vec{a}_3$ which define the parallelepiped, we define the transformation matrix by $h := [\vec{a}_1, \vec{a}_2, \vec{a}_3]$. Using this matrix, we obtain the scaled coordinates $\vec{u}_i := h^{-1}\vec{q}_i$, and the scaled impulses $p_{u,i} := h^{-1}p_i$. Further, we set $G := h^T h$ and introduce the variables external pressure P_{ext}, the barostat mass W, and the momentum of the scaling matrix p_h. The Parrinello-Rahman Hamiltonian is then written as

$$\mathcal{H}_{\text{Parrinello}} = \sum_i \frac{p_{u,i}^T G p_{u,i}}{2m_i} + U(h\vec{u}) + \frac{\text{tr}(p_h^T p_h)}{2W} + P_{ext} \cdot \det(h). \tag{2.12}$$

Consequently, we obtain the equations of motion

$$\begin{aligned}
\frac{\partial q_i}{\partial t} &= \frac{\partial \mathcal{H}}{\partial \tilde{p}_i} = \frac{G\tilde{p}_i}{m_i s^2}, & \frac{\partial h}{\partial t} &= \frac{\partial \mathcal{H}}{\partial p_h} = \frac{p_h}{W}, \\
\frac{\partial \tilde{p}_i}{\partial t} &= -\frac{\partial \mathcal{H}}{\partial q_i} = -\frac{\partial U(q)}{\partial q_i}, & \frac{\partial p_h}{\partial t} &= -\frac{\partial \mathcal{H}}{\partial h} = -\nabla_h \left(\sum_i \frac{p_{u,i}^T G p_{u,i}}{2m_i} \right) - \frac{\partial U}{\partial h},
\end{aligned}$$

where we have omitted further differentiation in the last equation. While we will provide some more details in section 2.3.4, where we show the conformity with our formulation of external forces, for further and more general information we point the reader to the original paper of Parrinello and Rahman [PR81].

Combined Parrinello-Rahman and Nosé-Hoover Variant of the Hamiltonian

Possibly more often than the above form, a variant is used, which additionally incorporates a temperature control via the previously introduced Nosé-Hoover thermostat

in order to control the NPT ensemble. When both transformations are combined, the final Hamiltonian is

$$\mathcal{H}_{NPT} = \sum_i \frac{\tilde{\vec{p}}_{u,i}^T \tilde{G} \tilde{\vec{p}}_{u,i}}{2m_i s^2} + U(\tilde{h}u, \tilde{h}) + \frac{\mathrm{tr}(\tilde{\vec{p}}_{h,i}^T \tilde{\vec{p}}_{h,i})}{2Ws^2} + P_{ext} \cdot \det(\tilde{h}) + \frac{\pi^2}{2Q} + g k_B T \ln(s), \quad (2.13)$$

where the tilde on the variables denotes the transformed variables in terms of the non-physical time τ [GH06]. Note that due to this non-physical time scale, this Hamiltonian suffers from the same shortcomings as the pure Nosé-Hoover Hamiltonian in (2.8), since the necessary transformation leads to non-Hamiltonian equations of motion. However, as before there is a true Hamiltonian variant, which makes use of very similar techniques as those presented for the Nosé-Poincaré Hamiltonian, compare [Her01]. Additionally, this work has replaced the dependency on the scaling matrix h by the metric tensor G, removing the issue of handling the orientation of the domain, which otherwise requires additional matrix constrains in the algorithms of Molecular Dynamics software [N$^+$16].

In order to demonstrate that the external forces which we introduce in the following sections will match with the equations of motions already used, we will revisit these formulations in section 2.3.4.

2.2.3 The Fluctuation Theorem and its Consequences

In the context of Non-Equilibrium Molecular Dynamics (NEMD), research was conducted into statistical distribution of entropy. While the second law of thermodynamics generally prohibits the decrease of entropy in natural processes[10], microscopic equations of motion are generally reversible. As a consequence, processes of microscopic scale and – in the current context more importantly – simulations of finite size and finite time may exhibit behavior where the entropy of a closed system is reduced, that is, they are reversions of classically irreversible processes.

This contradiction was known for some time [Bol70], but while it was accepted that the above law holds "on average" in the meaning that it holds only for macroscopic systems, the question on how the reversibility of the microscopic equations of motion corresponds to irreversible macroscopic behavior was not acceptably resolved.

In the last decade of the 20$^{\text{th}}$ century, researchers proposed a quantitative estimate for "Probability of Second Law Violations in Shearing Steady States" [ECM93], an article which despite its seemingly narrow application layed the groundwork for more general results for ensembles which are in a non-equilibrium configuration [ES94] and possibly far from equilibrium.

[10] There are several, generally equivalent formulations of this law. The one used here follows Planck [Pla22]: "Jeder in der Natur stattfindende physikalische und chemische Prozeß verläuft in der Art, daß die Summe der Entropien sämtlicher an dem Prozeß irgendwie beteiligten Körper vergrößert wird."

This came to be known later as the Fluctuation Theorem: With S as the entropy produced over the observation time t, the probability of the inverse process (which will have corresponding negative entropy production) is computed to be

$$\frac{P(\frac{S}{k_B t} = A)}{P(\frac{S}{k_B t} = -A)} = e^{At},$$

meaning that the probability for "violating" processes decreases exponentially as the average rate of entropy production or the observation time increase.

This approach proved to be successful, first being supported by computer simulations and later with experimental results, where trajectories of individual particles could be monitored in an optical trap [Ger02, WSM+02].

These results are significant in supporting the validity of Molecular Dynamics simulation results which were not computed from an equilibrium setting. While extensive descriptions of specific aspects of non-equilibrium dynamics existed before, e.g. [EM07], other aspects are still lacking. In particular, none of the current works yields a way to detect the presence of a steady state, apart from an analysis of the phase space density distribution [SPWS08].

Further disccusions on the effects of the Fluctuation Theorem consider the validity of Green-Kubo and Einstein expressions for linear transport coefficients in the case of non-equilibrium fluids with repulsive pair potentials. The results obtained suggest that in the linear regime corrected variants of the calculation can be used, while failure is observed far from equilibrium. The basis of this result are independence assumptions on the sample behavior, which can no longer be postulated for ensembles under the effect of external forces, an assumption that is also formulated in [SE00, SPWS08]. It is postulated that for averaging times larger than a so-called Maxwell time $\tau = \frac{\eta}{\mu}$, given by the fraction of dynamics' viscosity η and shear modulus μ, which characterizes correlations in the dissipative flux, the required independence will be achieved.

However, this time estimate is not applicable to all settings, in particular, when external forces act on a subset of the ensemble particles or the external forces change the alignment of the particles over time, violating a steady state setting. We will revisit these considerations in chapter 3, when we consider upscaling formulas and their requirements for validity in non-equilibrium settings.

2.3 New Approach to Incorporating Arbitrary External Forces

In this section we come to the heart of our contribution to Molecular Dynamics. We intend to formalize the interaction of the simulation ensemble with an outside energy reservoir via force interactions acting on individual particles and at the same time wish to measure the energy transferred between the outside and inside system.

Our approach will be to express the energy exchanged with the external reservoir via the work done on the particle by the force, leading to interchangable formulations of the energy via a path integral over the force and a time integral over the scalar product of velocity and force. The prior formulation will allow for the expression of the energy exchange in Hamiltonian form, while the latter formulation will allow for an implementation of computation of the accumulated energy exchange while considering periodic boundary conditions and still maintaining unique reprensentation of image coordinates.

In the context of energy conserving NVE simulations, we will then be able to observe conservation of energy with respect to the global system. At the same time, when considering other external interactions such as NVT simulations, we will be able to compute the energy transference of either type of interaction and by comparing both energy fluxes, decide whether the ensemble reaches a steady state. Furthermore, the computation of the energy added by outer interaction will enable the computation of the strength of heat sources, which can be bridged to higher scaled simulations or considered as a newly measured macroscopic value in its own right which we discuss in chapter 3.

Finally, we will connect the application of external forces with existing thermostat types.

2.3.1 External Forces on Particles

In this section we will assume that an external force $F_{i,ext}$ exists for all particles i, which is added to the forces resulting from internal interaction in the ensemble, so that

$$\vec{F}_{i,tot} = \vec{F}_{i,inter} + \vec{F}_{i,ext}.$$

Such an external force might be the result of interaction between charged particles and an electrical potential applied across the domain. When the potential is linear across the simulation domain, the result will be a constant force per particle. However, the usual assumption of periodicity causes problems with this interpretation. The position of a particle is not necessarily well-defined and leads to discontinuities in the potential measured and thus in the total energy of the particle, see figure 2.2. After summation over all particles, energy is no longer conserved.

However, when we define the field via its derivatives

$$\vec{F}_{i,ext} = \nabla_{x_i} U_{ext}$$

there is no requirement that U_{ext} is the same function for all particles i. In particular, for $i \neq j$

$$U_{ext}(\vec{x}_i(t)) \neq U_{ext}(\vec{x}_j(t')) \qquad \text{for } \vec{x}_i(t) = \vec{x}_j(t')$$

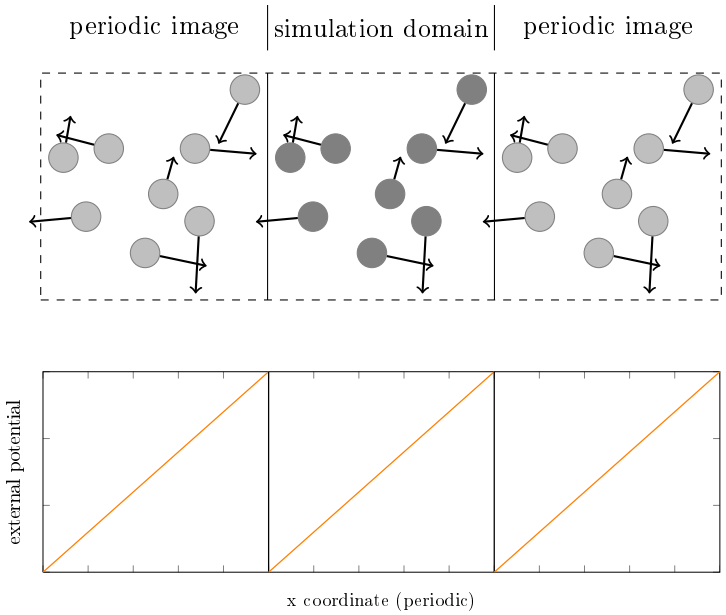

Figure 2.2: Periodic cells with a classical external potential showing discontinuities.

would not violate the conservativeness of the field.

For the special and limited case of constant external forces, we could express the external potential by

$$U_{ext} = \sum_i \vec{F}_{i,ext} \cdot (\vec{x}(t) - \vec{x}_0).$$

By this interpretation, the energy in the external potential is identically 0 for all particles at time $t = 0$, but nevertheless the change in energy due to repositioning is properly taken into account.

However, this method is limited in several ways. In addition to not being able to handle changing external forces, it encounters implementation problems for periodic boundary conditions, as upon passing a boundary the coordinates of the image of the particle no longer coincide with its position in the field. While this might be remedied by treating both positions seperately, outside interactions with the field and internal interactions with other particles would now depend on different coordinate sets. Both of these problems will be addressed in the next section.

Duality of Energy and Work

It is known from physics [Dem04a], that the work $W_i(t)$ performed on a particle in

the time interval $[0, t]$ is

$$W_i(t) = \int_0^t \vec{F}_i(\tau)\vec{v}_i(\tau)d\tau.$$

To restrict this expression to the work done by the external field, we replace the total force $\vec{F}_i$ on the particle by the external force $\vec{F}_{i,ext}$ on the particle. By the first law of thermodynamics, we know that the work done on the particle must correspond to a change of energy with respect to the external field

$$W_{i,ext}(t) = \Delta U_{i,ext} := U_{i,ext}(t) - U_{i,ext}(0)$$
$$\Leftrightarrow \int_0^t \vec{F}_{i,ext}(\tau)\vec{v}_i(\tau)\,d\tau = \int_{\vec{x}_i(0)}^{\vec{x}_i(t)} \vec{F}_{i,ext}\,dy. \tag{2.14}$$

This duality now allows us to perform proper analysis in a Molecular Dynamics environment with periodic boundary conditions. For the computation of the force acting on a particle the right hand side of equation (2.14) is used, whereas for the evaluation of the current energy of the particle the left hand side is taken into account, which is independent of the current periodic image of the particle.

2.3.2 Changes in Total Energy from External Forces

The total energy of classical systems is evaluated as the sum of the internal kinetic and potential energy

$$E = E_{kin} + E_{pot} = \sum_i \frac{1}{2} m\vec{v}_i^2 + U_0(\vec{q}).$$

When the system is subject to external forces, we observe the following change in energy

$$\begin{aligned}
\frac{dE}{dt} &= \frac{dE_{kin}}{dt} + \frac{dE_{pot}}{dt} \\
&= \sum_i \left[m_i\vec{v}_i\dot{\vec{v}}_i + \sum_k \frac{\partial U}{\partial x_{i,k}}\frac{\partial x_{i,k}}{\partial t} \right] \\
&= \sum_i \left[m_i\vec{v}_i\dot{\vec{v}}_i + \nabla_{x_i}U_0 \cdot \vec{v}_i \right] \\
&= \sum_i \left(m_i\dot{\vec{v}}_i + \nabla_{x_i}U_0 \right)\vec{v}_i \\
&= \sum_i \left(m_i\frac{-\nabla_{x_i}U_0 + \vec{F}_{i,ext}}{m_i} + \nabla_{x_i}U_0 \right)\vec{v}_i \\
&= \sum_i \vec{F}_{i,ext}\vec{v}_i.
\end{aligned}$$

The energy contribution $\tilde{U}$ of this force to the system is then given by

$$\tilde{U}(\vec{x}, \dot{\vec{x}}, t) = \sum_i \int_{x_i(0)}^{x_i(t)} \vec{F}_{ext,i}(\vec{y})\, d\vec{y}.$$

If we take into account that work performed on the system corresponds to a reduced energy of the surrounding system (which yields the work), we are able to observe the conservation of energy. By setting

$$U := U_0 - \tilde{U}$$

we obtain

$$\begin{aligned}\frac{dE}{dt} &= \sum_i \left(m_i \vec{v}_i \dot{\vec{v}}_i + \nabla_{x_i} U_0 \cdot \vec{v}_i - \vec{F}_i(\vec{x}_i(t)) \vec{v}_i \right) \\ &= \sum_i \left(m_i \dot{\vec{v}}_i + \nabla_{x_i} U_0 - \vec{F}_i(\vec{x}_i(t)) \right) \vec{v}_i \\ &= 0.\end{aligned}$$

2.3.3 From Lagrangian to Hamiltonian Dynamics

In the following section we will show that the addition of external forces can be set into a Hamiltonian formulation of the ensemble, while still taking periodic domains into account. To this end, we must place requirements on both the trajectories of the particles and the structure of the external forces.

- We require that the simulation time can be partitioned into intervals, such that the coordinate functions of the particle trajectories are injective in the simulation domain Ω.

$$\begin{aligned}\text{For } [t_0, t_{end}],\ \forall i\, \exists\, \{t_k\}_{k=0}^m \text{ with } t_m = t_{end},\ t_k < t_{k+1},\ I_k = [t_k, t_{k+1}], \\ \text{s.t. } \vec{x}_i : I_k \to \Omega \text{ is injective.}\end{aligned} \tag{2.15}$$

Note that we only require a partition of the time interval for each trajectory by itself. A suitable partition for the whole ensemble is simply obtained by collecting the intersections of intervals for all particles, since these will always be a finite number. This requirement ensures that we can make the transformation from the energy integral in time to the corresponding line integral along the trajectory of the particle. On the individual trajectory the function is now even bijective and we obtain an inverse function

$$\tau_{i,k} : \Omega \to I_k;\ \tau_{i,k}(\vec{x}_i(t)) := t$$

and as a consequence we will use the time and space arguments of $\vec{F}_i$ interchangeably by defining

$$\vec{F}_{i,k}(\vec{x}_i) := \vec{F}_i(\vec{x}_i, \tau_{i,k}(\vec{x}_i))$$
$$\vec{F}_i(t) := \vec{F}_i(\vec{x}_i(t), t).$$

We use these definitions to formulate our requirement on the external forces.

- We require that the vector field $\vec{F}_{i,k}(\vec{x}_i) := \vec{F}_i(\vec{x}_i, \tau_{i,k}(\vec{x}_i))$ must be conservative on Ω so that the following holds

$$\exists \Phi_{i,k}(\vec{y}), \text{ s.t. } \vec{F}_{i,k}(\vec{y}) = \nabla \Phi_{i,k}(\vec{y}). \tag{2.16}$$

From now on without loss of generality, let $x_i : [t_0, t] \to \Omega$ be injective for all i on the complete time domain, which allows us to drop the index k of the time intervals. Should this not be the case we will create a set of intervals, which exist by requirement (2.15), and treat each of the intervals in turn. Now we may rewrite the energy integral

$$\int_{t_0}^{t} \vec{F}_i(\tau) \frac{\vec{p}_i}{m_i} \, d\tau = \int_{t_0}^{t} \vec{F}_i(\tau) \dot{\vec{x}}_i \, d\tau = \int_{\vec{x}_i(0)}^{\vec{x}_i(t)} \vec{F}_i(\vec{y}) \, d\vec{y},$$

where we do not specify a path in the last integral. This is permissible due to requirement (2.16), as the fact that the forces are defined by a gradient field make the line integral independent of the actual path taken. With this version of the energy contribution of the external forces we write the Lagrange function

$$\mathcal{L} := \sum_i \frac{1}{2} m_i \dot{\vec{x}}_i^2 - U(\vec{x}) + \sum_i \int_{x_i(0)}^{x_i(t)} \vec{F}_i(\vec{y}) \, d\vec{y}.$$

From this function we are able to obtain the equations of motion of the particles via the general ansatz of the Euler-Lagrange differential equations

$$\begin{aligned}
\frac{d}{dt} \frac{\partial \mathcal{L}}{\partial \dot{\vec{x}}_i} &= \frac{\partial \mathcal{L}}{\partial x_i} \\
\Rightarrow \qquad m \ddot{\vec{x}}_i &= -\frac{\partial U(\vec{x})}{\partial x_i} + \frac{\partial}{\partial x_i} \int_{x_i(0)}^{x_i(t)} \vec{F}_i(\vec{y}) \, d\vec{y} \\
&\overset{(2.16)}{=} -\frac{\partial U(\vec{x})}{\partial x_i} + \frac{\partial}{\partial x_i} \int_{x_i(0)}^{x_i(t)} \nabla \Phi_i(\vec{y}) \, d\vec{y} \\
&= -\frac{\partial U(\vec{x})}{\partial x_i} + \frac{\partial}{\partial x_i} \left(\Phi_i(\vec{x}_i(t)) - \Phi_i(\vec{x}_i(0)) \right) \\
&\overset{(2.16)}{=} -\frac{\partial U(\vec{x})}{\partial x_i} + \vec{F}_{i,ext}(\vec{x}_i(t)),
\end{aligned} \tag{2.17}$$

where we can apply the fundamental theorem of calculus [BSMM01] to the line integral due to its path independence as a gradient field. Indeed we obtain the usual equations of motions with added external forces.

Following the successful formulation in Lagrangian dynamics, we turn to the transformation into a Hamiltonian function. To this end, we perform a Legendre transformation [ZRM09] of the Lagrange function

$$\frac{\partial \mathcal{L}}{\partial \dot{\vec{x}}_i} = m\dot{\vec{x}}_i =: \vec{p}_i,$$

which, since the line integral is not directly dependent on the velocity of the particles, results in the transformed variable $\vec{p}$. We will refer to this parameter as the *canonical impulse*. This leads to the Hamiltonian function

$$\begin{aligned}
\mathcal{H} &= \sum_i \frac{\vec{p}_i}{m_i} \frac{\partial \mathcal{L}}{\partial \dot{\vec{x}}_i} - \mathcal{L} \\
&= \sum_i m_i \dot{\vec{x}}_i \dot{\vec{x}}_i - \frac{1}{2} m_i \dot{\vec{x}}_i^2 + U(\vec{x}) - \int_{\vec{x}_i(0)}^{\vec{x}_i(t)} \vec{F}_i(\vec{y})\, d\vec{y} \\
&= \sum_i \frac{\vec{p}_i^2}{2m_i} + U(\vec{x}) - \int_{\vec{x}_i(0)}^{\vec{x}_i(t)} \vec{F}_i(\vec{y})\, d\vec{y}.
\end{aligned}$$

To conform to the notation in standard literature, we substitute $\vec{q}_i(t) := \vec{x}_i(t)$, leaving us with

$$\mathcal{H} = \sum_i \frac{\vec{p}_i^2}{2m_i} + U(\vec{q}) - \int_{\vec{q}_i(0)}^{\vec{q}_i(t)} \vec{F}_i(\vec{y})\, d\vec{y}.$$

Now we check whether we obtain identical equations of motion

$$\begin{aligned}
\dot{\vec{p}}_i &= -\frac{\partial \mathcal{H}}{\partial \vec{q}_i} \\
&= -\frac{\partial U(\vec{q})}{\partial \vec{q}_i} + \frac{\partial}{\partial \vec{q}} \int_{\vec{q}_i(0)}^{\vec{q}_i(t)} \vec{F}_i(\vec{y})\, d\vec{y} \\
&= -\frac{\partial U(\vec{q})}{\partial \vec{q}_i} + \vec{F}_i(\vec{q}_i(t)),
\end{aligned}
\qquad
\begin{aligned}
\dot{\vec{q}}_i &= \frac{\partial \mathcal{H}}{\partial \vec{p}_i} \\
&= \frac{\vec{p}_i}{m_i},
\end{aligned}$$

and find that both the Lagrangian and Hamiltonian approach produce the same results, which also coincied with our initial conjecture.

Gains from this Method

We are now able to accurately compute the energy contribution to the ensemble instead of just estimating it via mean velocities. As a first result, this allows us

to observe non-equilibrium NVE ensembles, since we can take the reduction of the external potential energy in the computation of the total energy into account.

Of even larger interest is the combination with thermostats and barostats. It is now possible to check whether a steady state has been reached, e.g in the thermostat case by observing and comparing the rate of energy exchange between the external field and the heat bath. This is a criterion for the evaluation of macroscopic variables, since for ensembles in a transient state they may change by definition. These macroscopic variables can be evaluated from our provided Hamiltonian function; in particular, we can combine our method with ensembles which interact with the temperature and/or pressure. Additionally, this method conforms with mathematical reversibility, as long as suitable integration schemes are used. While the modeled macroscopic physical processes are generally not reversible, the implementation of external forces as described here satisfies the requirements on the equations of motion of the Fluctuation Theorem as presented in [SPWS08], justifying that we obtain microscopic reversibility of the trajectories.

As the external forces result in a change of energy in the ensemble, heat is transfered between the internal system and its outside. Heat generation terms may be evaluated, as the energy flux from the field has influence on internal potential energy and kinetic energy. This may be measured in isolation or even in concert with thermostats and allows for the computation of the amount of heat extracted from the ensemble volume over a set time frame. Further discussion of this upscaling will take place in chapter 3.

2.3.4 Conformity of External Forces with Thermo- and Barostats

In section 2.2.2 we presented already existing modifications of Hamiltonians which established temperature and pressure control of the ensemble. We will now revisit these Hamiltonians and add our external forces, demonstrating that the respective methods can be combined with our new approach.

Although we have established that the classical Nosé-Hoover Hamiltonian ultimately does not lead to a Hamiltonian formulation, we will nevertheless prove the conformity with our new approach as this thermostat still plays a significant role in many implementations of Molecular Dynamics software [P$^+$16, N$^+$16].

Conformity with Nosé-Hoover

We begin with the Hamiltonian (2.8), adding the path integrals of external forces

$$\mathcal{H}_{\text{Nosé}} = \sum_i \frac{\vec{p}_i^2}{2m_i s^2} + U(\vec{q}) - \sum_i \int_{\vec{q}_{i,0}}^{\vec{q}_i} \vec{F}_{ext,i}\, dx + \frac{\pi^2}{2Q} + g k_B T \ln(s). \tag{2.18}$$

As before we derive Hamilton's equations for the non-physical time scale

$$\frac{\partial q_i}{\partial \tau} = \frac{\tilde{p}_i}{m_i s^2}, \qquad \frac{\partial s}{\partial \tau} = \frac{\pi}{Q},$$
$$\frac{\partial \tilde{p}_i}{\partial \tau} = -\frac{\partial U(q)}{\partial q_i} + \vec{F}_{ext,i}, \qquad \frac{\partial \pi}{\partial \tau} = \sum_i \frac{\tilde{p}_i^2}{m_i s^3} - g k_B T \frac{1}{s},$$

before we introduce the transformations

$$p = \frac{\tilde{p}}{s}, \qquad \hat{\pi} = \frac{\pi}{s}, \qquad \frac{d\tau}{dt} = s,$$

resulting in the non-Hamiltonian equations

$$\dot{q}_i = \frac{p_i}{m_i}, \qquad \dot{s} = s^2 \frac{\hat{\pi}}{Q},$$
$$\dot{p}_i = -\frac{\partial U(q)}{\partial q_i} + \vec{F}_{ext,i}, \qquad \dot{\hat{\pi}} = \frac{1}{s}\left(\sum_i \frac{p_i^2}{m_i} - g k_B T\right) - s\frac{\hat{\pi}^2}{Q}.$$

As we can see, these equations conform to the standard equations of motion for the Nosé-Hoover formulation with the inner potential extended by the external forces.

Conformity with Nosé-Poincaré

We continue to the Nosé-Poincaré extension, where we will be able to construct a full Hamiltonian setting. As before we start with the Nosé-Poincaré Hamiltonian (2.10) with the addition of external energy

$$\mathcal{H}_{\mathcal{NP}} = \left(\sum_i \frac{\vec{p}_i^2}{2m_i s^2} + U(\vec{q}) - \sum_i \int_{\vec{q}_{i,0}}^{\vec{q}_i} \vec{F}_{ext,i}(x)\, dx + \frac{\pi^2}{2Q} + \tilde{g} k_B T \, \ln(s) - \mathcal{H}_0\right) s. \tag{2.19}$$

The derivation of Hamilton's equations of motion is straightforward, resulting in

$$\dot{q} = \frac{\tilde{p}_i}{m_i s}, \qquad \dot{s} = s\frac{\pi}{Q},$$
$$\dot{\tilde{p}}_i = -s\left(\frac{\partial U(q)}{\partial q_i} - \vec{F}_{ext,i}\right), \quad \dot{\pi} = \sum_i \frac{\tilde{p}_i^2}{m_i s^2} - g k_B T - \Delta H$$

with

$$\Delta H := \sum_i \frac{\vec{p}_i^2}{2m_i s^2} + U(\vec{q}) - \sum_i \int_{\vec{q}_{i,0}}^{\vec{q}_i} \vec{F}_{ext,i}\, dx + \frac{\pi^2}{2Q} + \tilde{g} k_B T \, \ln(s) - \mathcal{H}_0.$$

We see that two equations are affected, the update of the reduced impulse variable and the update of the Nosé-Poincaré impulse. It is trivial to see that the scaling of both, the forces from the inner potential and the external forces, is identical in the update of the particle impulses. Furthermore, inner and outer forces appear in the update of the thermostat impuls $\dot{\pi}$ in the same form as they did in the Hamiltonian, this time both without scaling. We conclude that the addition of external forces conforms to the Nosé-Poincaré variant of the thermostat as well.

Conformity with Parrinello-Rahman

After having established the conformity of our external forces formulation with popular thermostat Hamiltonians, we turn to the realm of barostats. We will demonstrate conformity for the original Parrinello-Rahman barostat as well as its combination with the Nosé-Hoover thermostat. In the literature multiple different transformations of coordinates are present [GH06, Her01, SM97, PR81], a matter which is more elaborate than we wish to address here. Instead we will focus on the conformity of the external forces with the internal ones, leaving the treatment of known terms to the previously stated literature. With this approach in mind, we consider the external energy formulation in terms of scaled coordinates and their derivatives in terms of the coordinates and the scaling respectively

$$
\begin{aligned}
& \sum_i \int_{\vec{q}_{i,0}}^{\vec{q}_i} \vec{F}_{ext,i}(x)\,dx = U_{ext}(\vec{q}) && \mid \text{Substitute } \vec{q}_i = h\cdot\vec{u}_i \\
\Leftrightarrow \quad & \sum_i \int_{h_0\vec{u}_{i,0}}^{h\vec{u}_i} \vec{F}_{ext,i}(x)\,dx = U_{ext}(h\vec{u}) \\
\Rightarrow \quad & \frac{\partial}{\partial u_i}\sum_i \int_{h_0\vec{u}_{i,0}}^{h\vec{u}_i} \vec{F}_{ext,i}(x)\,dx = \frac{\partial U_{ext}}{\partial q_i}\cdot\frac{\partial q_i}{\partial u_i} = \vec{F}_{ext,i}(h\vec{u}_i)^T\cdot h \\
\Rightarrow \quad & \frac{\partial}{\partial h}\sum_i \int_{h_0\vec{u}_{i,0}}^{h\vec{u}_i} \vec{F}_{ext,i}(x)\,dx = \frac{\partial U_{ext}}{\partial q_i}\cdot\frac{\partial q_i}{\partial h} = \vec{F}_{ext,i}(h\vec{u}_i)\cdot\vec{u}_i^T .
\end{aligned}
$$

Note that the substitution may not be performed in the integration variable, as the scaling matrix h changes over time. However, the starting point of the integral is constant, thus it is always transformed by the initial scaling matrix $h_0 := h(0)$. We recall the Hamiltonian from (2.12) and add external energy contributed by forces

$$
\mathcal{H}_{\text{Parrinello}} = \sum_i \frac{p_{u,i}^T G p_{u,i}}{2m_i} + U(h\vec{u}) - \sum_i \int_{h_0\vec{u}_{i,0}}^{h\vec{u}_i} \vec{F}_{ext,i}(x)\,dx + \frac{\operatorname{tr}(p_h^T p_h)}{2W} + P_{ext}\cdot\det(h).
$$

Consequently, we obtain the equations of motion

$$\frac{\partial q_i}{\partial t} = \frac{\partial \mathcal{H}}{\partial \tilde{p}_i} = \frac{G\tilde{p}_i}{m_i}, \tag{2.20}$$

$$\frac{\partial \tilde{p}_i}{\partial \tau} = -\frac{\partial \mathcal{H}}{\partial u_i} = -\frac{\partial U(h\vec{u})}{\partial u_i} + \vec{F}_{ext,i}(h\vec{u}) \cdot h, \tag{2.21}$$

$$\frac{\partial h}{\partial t} = \frac{\partial \mathcal{H}}{\partial p_h} = \frac{p_h}{W}, \tag{2.22}$$

$$\frac{\partial p_h}{\partial t} = -\frac{\partial \mathcal{H}}{\partial h} = \frac{\partial}{\partial h}\Bigg(\sum_i \frac{p_{u,i}^T G p_{u,i}}{2m_i} - U(h\vec{u}) + \sum_i \int_{h_0\vec{u}_{i,0}}^{h\vec{u}_i} \vec{F}_{ext,i}(x)\, dx + P_{ext} \cdot \det(h)\Bigg). \tag{2.23}$$

Obviously, equations (2.20) and (2.22) have not changed compared to the original equations of motion, so we only need to concern ourselves with the conformity of equations (2.21) and (2.23). In order to compare the potential contributions we consider the partial derivatives of the inner potential $U(h\vec{u})$

$$\frac{\partial}{\partial u_i} U(h\vec{u}) = \frac{\partial U}{\partial q_i} \cdot \frac{\partial q_i}{\partial u_i} = \left(\frac{\partial U}{\partial q_i}\right)^T \cdot h,$$
$$\frac{\partial}{\partial h} U(h\vec{u}) = \frac{\partial U}{\partial q_i} \cdot \frac{\partial q_i}{\partial h} = \frac{\partial U}{\partial q_i} \cdot u_i^T.$$

Inserting the results into equations (2.21) and (2.23)

$$\frac{\partial \tilde{p}_i}{\partial \tau} = -\left(\frac{\partial U}{\partial q_i}\right)^T \cdot h + \vec{F}_{ext,i}(hu) \cdot h = \left(-\left(\frac{\partial U}{\partial q_i}\right)^T + \vec{F}_{ext,i}(hu)\right) \cdot h,$$
$$\frac{\partial p_h}{\partial t} = \frac{\partial}{\partial h}\left(\sum_i \frac{p_{u,i}^T G p_{u,i}}{2m_i} + P_{ext} \cdot \det(h)\right) - \frac{\partial U}{\partial q_i} \cdot u_i^T + \vec{F}_{ext,i}(h\vec{u}_i) \cdot u_i^T$$
$$= \frac{\partial}{\partial h}\left(\sum_i \frac{p_{u,i}^T G p_{u,i}}{2m_i} + P_{ext} \cdot \det(h)\right) + \left(-\frac{\partial U}{\partial q_i} + \vec{F}_{ext,i}(h\vec{u}_i)\right) \cdot u_i^T,$$

we find that both external and internal forces are subject to the same scaling in their respective equations and thus can conclude that our formulation of external forces is valid in this ensemble as well.

Having established the conformity in the NPE ensemble, we consider the Hamiltonian presented in (2.13) combining the Nosé-Hoover thermostat and the Parrinello-Rahman barostat to an instance of an NPT ensemble with the addition of external

forces

$$\begin{aligned}\mathcal{H}_{NPT} =& \sum_i \frac{\tilde{\vec{p}}_{u,i}^T \tilde{G} \tilde{\vec{p}}_{u,i}}{2m_i s^2} + U(\tilde{h}u) - \sum_i \int_{\tilde{h}_0 \vec{u}_{i,0}}^{\tilde{h}\vec{u}_i} \vec{F}_{ext,i}(x)\, dx \\ &+ \frac{\mathrm{tr}(\tilde{p}_{h,i}^T \tilde{p}_{h,i})}{2Ws^2} + P_{ext} \cdot \det(\tilde{h}) + \frac{\pi^2}{2Q} + g k_B T \ln(s),\end{aligned}$$

which result in the equations of motion

$$\begin{aligned}\frac{\partial q_i}{\partial \tau} &= \frac{G\tilde{p}_i}{m_i s^2}, \\ \frac{\partial \tilde{p}_i}{\partial \tau} &= -\frac{\partial U(\tilde{h}u)}{\partial u_i} + \vec{F}_{ext,i}(\tilde{h}u) \cdot \tilde{h} \\ &= \left(-\frac{\partial U}{\partial q_i}^T + \vec{F}_{ext,i}(\tilde{h}u) \right) \cdot \tilde{h}, \end{aligned} \tag{2.24}$$

$$\begin{aligned}\frac{\partial \tilde{h}}{\partial \tau} &= \frac{p_h}{Ws^2}, \\ \frac{\partial p_h}{\partial \tau} &= \frac{\partial}{\partial \tilde{h}} \left(\sum_i \frac{p_{u,i}^T G p_{u,i}}{2m_i s^2} + P_{ext} \cdot \det(\tilde{h}) \right) - \frac{\partial U(\tilde{h}u)}{\partial \tilde{h}} \\ &\quad + \frac{\partial}{\partial \tilde{h}} \left(\sum_i \int_{\tilde{h}_0 \vec{u}_{i,0}}^{\tilde{h}\vec{u}_i} \vec{F}_{ext,i}(x)\, dx \right) \\ &= \frac{\partial}{\partial \tilde{h}} \left(\sum_i \frac{p_{u,i}^T G p_{u,i}}{2m_i s^2} + P_{ext} \cdot \det(\tilde{h}) \right) + \left(-\frac{\partial U}{\partial q_i} + \vec{F}_{ext,i}(\tilde{h}\vec{u}_i) \right) \cdot u_i^T, \\ \frac{\partial s}{\partial \tau} &= \frac{\pi}{Q}, \\ \frac{\partial \pi}{\partial \tau} &= \sum_i \frac{\tilde{p}_i^2}{m_i s^3} + \frac{\mathrm{tr}(\tilde{p}_{h,i}^T \tilde{p}_{h,i})}{2Ws^3} - g k_B T \frac{1}{s}. \end{aligned} \tag{2.25}$$

In this way, we have shown analogously to the pure Parrinello-Rahman equations, that the scaling of internal and external forces coincide, compare equations (2.24) and (2.25). The other equations are unaffected by the addition of external forces.

In summary, we have shown in the above three sections that our new formulation of external forces can be combined with three traditional methods of thermo- and barostating originally based on Hamiltonian formulations. As a consequence, the integration schemes of these methods can be used with only minor modifications in the update functions where the external energy and forces are concerned, and without any effect on the other variables.

3 Upscaling from Particle to Continuum Dynamics

This chapter is dedicated to the connection of the molecular dynamics simulations to the coefficients of the continuum dynamics equations.

After a brief review of upscaling techniques for particle dynamics, we will begin a discussion of upscaling techniques for migration phenomena in non-equilibrium molecular dynamics, such as diffusion and convection. We will also discuss the possibility of measuring heat generation in the ensemble and estimate the error associated with this measurement.

For all measurements we will keep in mind that the computation of macroscopic phenomena from a microscopic ensemble is often accompanied by assumptions on the ensemble, which need to be satisfied for the computation to be valid. Generally, these requirements rely on equilibrium conditions in the ensemble, rendering them void in the context of non-equilibrium molecular dynamics. Nevertheless, there are exceptions in either direction, meaning that there are measurements for which the requirement of equilibrium conditions alone is not sufficient to guarantee validity, as well as measurements which continue to function in non-equilibrium conditions. In these cases other requirements need to be satisfied, with steady state conditions of the energy flux being an important criterium.

Thus we will conclude this chapter with a discussion of steady state detection for the application of external forces and thermostats.

3.1 Overview of Upscaling Techniques

The terminology *multiscale methods* refers to a multitude of diverse methods and techniques, some of which are very similar, while others have almost nothing in common. The methods depend on the problems involved and as such – for molecular problems – upscaling may take place from wave functions on the quantum-mechanical scale to particles on the atomistic scale, each with their own passing of time, while for applications in plate tectonics upscaling methods may link different partial differential equations from the centimeter to the kilometer regime.

Many popular multiscale methods such as Coarse Graining [NCA+08] or Homogenization [NRLJ10] stay within their respective method framework of particle dynamics and partial differential equations. Consequently, since a general discussion of avail-

able multiscale methods would be beyond the scope of this thesis, we restrict ourselves to the discussion of methods linking particle dynamics to continuum mechanics and point to [GLW08] for a general overview of methods and their building blocks.

In our application we intend to bridge from microscale particle methods using ångström and femtoseconds to continuum equations on the centimeter and minute scale. Even between those particular scales different methods may be used. In the application of stress and strain modeling, including crack simulation, which is clearly a non-equilibrium process, different areas of the same domain are treated with different methods and interface via a so-called "handshake" region, where an interface between both methods is established [TM11]. This method, known under the name of bridging scale method, is suitable for applications involving solids, where only a limited region requires the fine scale attention.

The scaling process we are interested in is quite different. We intend to derive macroscopic properties from the finer scale which are applicable over large parts of the simulation domain, both in time and in space. As such they correspond to the ideas laid out in [WEL+07] under the name heterogenous multiscale methods, which emphazise that the physical models do not necessarily need to be identical and which understand the upscaling process as an estimation of missing components of the macroscopic model. While the physical models are not identical, we need to ensure that data supplied to the macroscopic equation and the boundary conditions set to the microscopic system model the same problem. We make use of the method of averaging in order to match the phenomena of particle dynamics to the continuum scale, which we will describe in the following section.

3.2 Matching the Scales

In order to relate to the heterogenous multiscale methods, we need to link our particle dynamics to the continuum equation which we investigate. We display the derivation already presented in [Neu10] expanding on the method of averaging in [Sal98].

We define the averaging operator for arbitrary variables X

$$\langle X \rangle_K := \frac{1}{n} \sum_{i=0, k \in K}^{n} X(k_i)$$

with $n = |K|$.

On the particle scale we define a discrete concentration of particles belonging to a common group K via the delta distribution[1]

$$\tilde{c}_K(x) = \sum_{i \in K,\, x_i \in \Omega} \delta(x - x_i)$$

[1] The delta distribution is defined to be the unique distribution with the property $\int \delta(x - x_0) f(x)\, dx = f(x_0)$.

where Ω denotes the whole domain of the particles and x_p is the location of particle p. By averaging over an environment[2] $B_r(x)$ with radius r around x, we obtain a concentration function

$$c_K(x) = \frac{1}{|B_r(x)|} \int_{B_r(x)} \tilde{c}_K(\tilde{x})\, d\tilde{x}. \tag{3.1}$$

Note that $|B_r(x)| = |B_r(y)| =: V_r$ for all x and y, i.e. the volume of the ball is constant, only its position changes. Without chemical reactions, we can then derive the continuity equation by applying the time derivative to (3.1), substituting $\tilde{x} = x' + x$

$$\begin{aligned}
\frac{\partial c_K}{\partial t} &= \frac{\partial}{\partial t}\frac{1}{V_r}\int_{B_r(x)} \sum_{i\in K,\, x_i\in\Omega} \delta(\tilde{x} - x_i)\, d\tilde{x} \\
&= \frac{\partial}{\partial t}\frac{1}{V_r}\int_{B_r(0)} \sum_{i\in K,\, x_i\in\Omega} \delta(x + x' - x_i)\, dx' \\
&= \frac{1}{V_r}\int_{B_r(0)} \sum_{i\in K,\, x_i\in\Omega} \frac{\partial}{\partial t}\delta(x + x' - x_i)\, dx' \\
&= \frac{1}{V_r}\int_{B_r(0)} \sum_{i\in K,\, x_i\in\Omega} \sum_{j=1}^{3} \frac{\partial \delta(x + x' - x_i)}{\partial x_i^j}\frac{\partial x_i^j}{\partial t}\, dx' \\
&= \frac{1}{V_r}\int_{B_r(0)} \sum_{i\in K,\, x_i\in\Omega} \sum_{j=1}^{3} (-1)\frac{\partial \delta(x + x' - x_i)}{\partial x^j}\frac{\partial x_i^j}{\partial t}\, dx' \\
&= -\sum_{j=1}^{3} \frac{\partial}{\partial x^j}\frac{1}{V_r}\int_{B_r(x)} \sum_{i\in K,\, x_i\in\Omega} \delta(x + x' - x_i)\frac{\partial x_i^j}{\partial t}\, dx' \\
&= -\nabla\frac{1}{V_r}\int_{B_r(0)} \sum_{i\in K,\, x_i\in\Omega} \delta(x + x' - x_i)\frac{\partial \vec{x}_i}{\partial t}\, dx' \\
&= -\nabla\frac{1}{V_r}\int_{B_r(x)} \sum_{i\in K,\, x_i\in\Omega} \delta(\tilde{x} - x_i)\frac{\partial \vec{x}_i}{\partial t}\, d\tilde{x} \\
&=: -\nabla \vec{J}_K,
\end{aligned} \tag{3.2}$$

where $\vec{J}_K$ is called the flux of the particles, which contains the velocities of the particles $\frac{\partial \vec{x}_i}{\partial t} = \vec{v}_i$. Note that the coordinates x and x' are independent of the time variable, which results in vanishing time derivatives $\frac{\partial x}{\partial t} = \frac{\partial x'}{\partial t} = 0$ in equation (3.2), shortening the expression considerably.

By considering the particle average and the respective individual deviation we ob-

[2] While our notation implies a spherical environment, this is not necessary. In practice the domains in Molecular Dynamics are formed by a parallelepiped.

tain

$$
\begin{aligned}
\vec{J}_K &= \frac{1}{V_r} \int_{B_r(x)} \sum_{i \in K,\, x_i \in \Omega} \delta(x - x_i) \frac{\partial \vec{x}_i}{\partial t}\, dx \\
&= \frac{1}{V_r} \int_{B_r(x)} \sum_{i \in K,\, x_i \in \Omega} \delta(x - x_i) \vec{v}_i\, dx \\
&= \frac{1}{V_r} \int_{B_r(x)} \sum_{i \in K,\, x_i \in \Omega} \delta(x - x_i) \left(\vec{v}_i - \langle v \rangle_K + \langle v \rangle_K\right)\, dx \\
&= \underbrace{\frac{1}{V_r} \int_{B_r(x)} \sum_{i \in K,\, x_i \in \Omega} \delta(x - x_i) \left(\vec{v}_i - \langle v \rangle_K\right)\, dx}_{\text{diffusion}} \qquad (3.3) \\
&\quad + \underbrace{\frac{1}{V_r} \int_{B_r(x)} \sum_{i \in K,\, x_i \in \Omega} \delta(x - x_i) \langle v \rangle_K\, dx}_{\text{convection}}. \qquad (3.4)
\end{aligned}
$$

The averaging integral acts now on the average velocity – the convection – and the deviation from this convection – the diffusion. This equation also demonstrates that it is not only the macroscopic convection which is relevant for the flux; we observe a seperation of scales, where macroscopic effects are not immediately visible on a restricted ensemble on the lower scale.

When we consider environments of points x_1 and x_2, which are sufficiently far apart with $|x_1 - x_2| \gg r$ and for which we have $c_K(x_1) \neq c_K(x_2)$, we see that the sum over the number of particles may lead to diffusive flux between the two points caused by the unbalanced concentration, which is not described by the average of the velocities.

The above expressions allow for some insights into the relation of diffusion and convection. Experimental evidence leads to the Einstein-Smoluchowski equation, tying the convection velocity to the diffusion properties of the material. While the above equations do not allow us to derive this relation directly, we see that both terms involve the averaging integral over the localized particle velocities. In particular, we note that the diffusion expression results from the deviation from the average convection, a fact which we will revisit in the following section formulating an improved expression for the diffusion measurement and later in 3.4.2, where we estimate the error in our convection measurements, which will also determine the error estimate for the energy transference.

3.3 Modified Diffusion

The extraction of diffusion values via the computation of Mean-Sqare Displacement (MSD) and Velocity-Auto-Correlation (VAC) functions is a well established practice

[FS02, MLK01]. However, the established methods fail when equilibrium conditions are violated, even worse, they already fail in equilibrium settings where constant convection is present. In the previous section we matched the micro- and the macroscale via an averaging method and established the diffusion as the deviation from the average convection. In this section we will make use of this relation towards improved methods of diffusion measurement.

Specific violations of equilibrium conditions can be circumvented by adaptions of the used methods as already described in [Neu10]. Nevertheless, we must take care that these modifications do not implicitly rely on original requirements which are no longer valid.

3.3.1 Velocity-Auto-Correlation

We begin the discussion of diffusion measurements with the measurement via the Velocity-Auto-Correlation function. The foundations of this method was laid in [Kub57], with further elaboration added in [Kub66]. The standard relation

$$D = \frac{1}{3} \lim_{t\to\infty} \int_0^t \langle v(t-\tau)v(0)\rangle \; d\tau$$

has been originally derived for equilibrium conditions, but can also be generalized to the case where $\lim_{t\to\infty} \langle v(t)v(0)\rangle = 0$. While we can write an explicit correction to this measurement, see [Neu10],

$$D = \frac{1}{3} \lim_{t\to\infty} \int_0^t \langle v(t-\tau)v(0)\rangle - \langle v(t-\tau)\rangle \langle v(0)\rangle \; d\tau,$$

this method unfortunately produces false results when applied to ensembles which are subject to external forces.

The reason for this failure lies in the original derivation of the VAC method, which assumes that the ensemble satisfies equilibrium conditions throughout the duration of the simulation to justify the time shift of the integral. The equivalence proposed in [FS02]

$$\langle \vec{v}(t)\vec{v}(\tau)\rangle = \langle \vec{v}(t-\tau)\vec{v}(0)\rangle$$

relies on the fact that the velocities of the particles become independent of their starting or intermediate conditions. For non-steady state conditions, this independence is clearly void, as the time evolution of the velocities is biased.

For steady state conditions, the case is less certain. While conditions can be postulated, under which Green-Kubo relations[3] are approximately valid under steady

[3] Green-Kubo relations are a general type of relations, of which the velocity auto correlation is a special case [FS02].

state conditions [SE00], there are restrictions on the magnitude of external forces, which depend on other transport coeefficients and their relation. Indeed, the original Green-Kubo relations have been derived for the small field limit and linear relations. However, the influence of general external forces does not necessarily couple linearly to the macroscopic transport and energy parameters. As a matter of fact, in most settings a quadratic phase of energy transfer can be expected, which corresponds to accelerated transport. We will discuss this phenomenon in section 3.4.1.

While of limited use, we can formulate a requirement for convergence of the VAC method for diffusion coefficients with

$$\langle v(t-\tau)v(0)\rangle - \langle v(t-\tau)\rangle \langle v(0)\rangle = o\left(\frac{1}{t}\right),$$

but this requirement is tautological in nature, as it is the base requirement for the convergence of the VAC integral and cannot be predicted from the ensemble setup.

However, the correction we presented in [Neu10] is sufficient, if a constant convection of particles is present, as the internal trajectories of a molecular dynamics system with non zero total impulse are equivalent to the trajectories of the same system where the average velocity is subtracted from all individual velocities.[4]

3.3.2 Mean Square Displacement

A different method for the computation of the diffusion is based on the displacement of the particles. While the original method relies on the particles to perform random movements around their point of origin, the modified method specifically takes the convective motion into account. Nevertheless, we will demonstate that for the method to work properly, the convection must have reached a steady state, or the measurements are bound to provide conflicting results over the course of the simulation.

We revisit results derived in [Neu10] by introducing

$$\vec{r}_i(t) = \vec{x}_i(t) - \vec{x}_i(0),$$

which is the distance traveled by a particle p during time t. Let g be a group of individual particles and n_g the number of particles in this group. Using the general mean displacement

$$\langle \vec{r}(t)\rangle = \frac{1}{n_g}\sum_{i\in g}\vec{r}_i(t)$$

for further computations would yield the original MSD equation for diffusion [FS02]. We present the formula correcting for directed movements, which makes use of the fact that we look for deviations from the average behavior.

[4] Needless to say, that the kinetic energy needs to be adjusted by an appropriate constant as well.

With the corrected displacement

$$\left\langle L^2(t)\right\rangle = \frac{1}{n}\sum_{i\in g}\left(\vec{r}_i(t) - \langle\vec{r}(t)\rangle\right)^2,$$

we measure the variance of the distance traveled $\vec{r}(t)$, which we use to compute the diffusion over the time interval t

$$D = \frac{1}{6}\frac{\langle L^2(t)\rangle}{t}. \tag{3.5}$$

We see the following analytic equivalences for $T = N\cdot\delta t$

$$\begin{aligned}
\frac{1}{6}\frac{\langle L^2(T)\rangle}{T} &= \frac{1}{6}\frac{\langle L^2(T)\rangle - 0}{T}\\
&= \frac{1}{6}\frac{\langle L^2(T)\rangle - \langle L^2(0)\rangle}{T}\\
&= \frac{1}{6}\frac{\langle L^2(T)\rangle - \langle L^2(0)\rangle}{N\cdot\delta t}\\
&= \frac{1}{6N}\sum_{j=1}^{N}\frac{\langle L^2(j\cdot\delta t)\rangle - \langle L^2((j-1)\cdot\delta t)\rangle}{\delta t} \qquad (3.6)\\
&\xrightarrow{\delta t\searrow 0} \frac{1}{6}\left\langle\frac{\partial\langle L^2(t)\rangle}{\partial t}\right\rangle_t,
\end{aligned}$$

where in (3.6) we expand the telescopic sum. In the context of a continuous average, the above reads

$$\begin{aligned}
\frac{1}{6}\left\langle\frac{\partial\langle L^2(t)\rangle}{\partial t}\right\rangle_t &= \frac{1}{6\,T}\int_0^T\frac{\partial\langle L^2(t)\rangle}{\partial t}\,dt\\
&= \frac{1}{6\,T}\int_0^T d\left\langle L^2(t)\right\rangle\\
&= \frac{1}{6\,T}\left\langle L^2(T)\right\rangle.
\end{aligned}$$

In the above equations we have shown the equivalence of the long time measurements of the diffusion equation with the time average over point measurements. This equivalence will be of use later, when we will be able to improve the error estimation of the convection measurements in section 3.4.2. Apart from the implications for the error estimates, this also implies that the method may be able to produce consistent results under non-steady state conditions. Indeed, in previous work we established [NGH12] that the method reproduced the equilibrium diffusion coefficients of an ensemble even when the ensemble was subject to external forces without thermal tempering, effectively constantly adding energy to the ensemble.

As a result, careful attention needs to be paid to a proper setup of the system, as unintentional use of non-steady state systems will lead to insensible results in most cases. This is demonstrated best when considering that using thermostats in conjunction with external forces and otherwise unobstructed or only slightly obstructed particle paths will lead to alignment of the particle trajectories. With aligned trajectories, the deviation from the average velocity declines, leading to a phenomenon often referred to as "flying ice cube", which was originally observed for thermostat scaling [HTC98]. When this phenomenon occurs, the energy originally stored in the internal degrees of freedom contributing to the diffusion is transfered to the convection, reducing the measured diffusion. Conversely, for obstructed particles with no temperature control present, the interparticle impact may heat up the whole ensemble, leading to unpredictable behavior, e.g. when phase changes are triggered, completely changing the basis of computation.

Nevertheless, the fact that unsteady states are accessible at all underlines the method's robustness in the context of non-equilibrium settings and recommends this method over the previous VAC.

3.4 Convection and External Energy

The measurement of convection per type of particle can easily be computed by the average over their velocities as noted in the correction term in 3.3. However, this average is subject to constant fluctuations and we will demonstrate, that the error of this ad hoc average may become arbitrarily large. Thus convection measurements need to take long term behavior into account, computing the particle convection over time t by

$$\vec{w}_i(t) = \frac{r_i(t)}{t}.$$

The resulting values can then be averaged with the standard method. In this section we will present error estimates for both, the ad hoc and the long term method.

Furthermore, it should be noted that in the presence of external forces the convection may generally be unbounded, which we will demonstrate with artificial test cases in section 5.1.2. In realistic applications this behavior is prevented by interparticle forces and collisions, which add a decelerating effect which balances with the accelerating force. However, these interactions transfer the energy from the affected particle species to the surrounding material, heating the total ensemble. In the presence of external forces it is a necessary criterion for the overall energy steady state that the convection reaches a steady state, since the total energy transfered to the ensemble

can be expressed in terms of the average convection of all particle types

$$E_{ext,F,k}(t) = \sum_k \int_{t_0}^{t} \vec{F}_{ext,k}(\tau) \left\langle \vec{v}(\tau) \right\rangle_k \, d\tau,$$
$$\frac{\partial E_{ext,F,k}(t)}{\partial t} = \sum_k \vec{F}_{ext,k}(t) \left\langle \vec{v}(t) \right\rangle_k ,$$

as otherwise the external energy flux continues to fluctuate. Consequently we will investigate the behavior of the convection more closely in the following sections, beginning with the acceleration behavior of particle velocities from external forces and later with estimations of the error of the convection measurements, which we will convert to estimate the error in the energy transfer from external forces.

3.4.1 Different Regimes of Acceleration

The average rate of energy transfer from external forces applied to an ensemble in equilibrium is expected to change over time. Initial acceleration of unobstructed particles leads to a linear increase in their average velocity, which again is part of the integrand in the external energy integral. The resulting energy transfer for particles subject to a constant force

$$\begin{aligned} E_{ext,i}(t) &= \int_{t_0}^{t} \vec{F}_i \cdot \left(\vec{v}_{i,0} + \int_{t_0}^{\tau} \frac{\vec{F}_i}{m_i} \, d\tau' \right) d\tau \\ &= (t - t_0) \cdot \vec{v}_{i,0} \cdot \vec{F}_i + \frac{1}{2m_i} (t - t_0)^2 \, \vec{F}_i^2 \end{aligned} \tag{3.7}$$

is quadratic in nature. However, the assumption of unobstructed particles cannot be expected to hold in most physical matter (with the exception of very thin gases). Instead, particles interact with their surroundings, transfering impulse and – as a result – changing magnitude and direction of their velocities. Assuming a homogenous medium, where the same (external) forces act on all particles, these interactions would not influence the overall energy transfer, as the formulae could be reduced to the center of momentum system, which would experience the cumulative forces on the particles. All of this changes however, when we investigate more complex ensembles which consist of particles of different masses and different outside interactions.

As the particles exchange impulses, they scatter and the new obtained impulse of an individual particle may be aligned in a different direction, possibly even the inverse of its previous impulse. In this case of impulse inversion, the energy transfer of this particle reverses as well, as the sign from the scalar product of force and velocity changes. Further interaction of the particles lead to additional changes in direction, all yielding different rates of energy transfer. After a sufficient number of interactions, the velocity state of the particles has been completely changed, it can be

considered reset. The time for this to happen is determined by the time a particle is on average free of interactions, the mean free time. During this time, external forces act unobstructed, accelerating – or decelerating – the particle. If the forces were to act unidirectional in the ensemble, that is the direction of force is the same for all particles which experience them, we would observe an acceleration of the full ensemble in the direction of the force. However, in most physical settings, the forces acting in a particular direction on one group of particles are paired with forces acting in the opposing direction for other groups of partices – consider for example an electric field, which exerts opposing forces on particles with opposite signs of charge.

After some initial acceleration, the internal impulse transfer from the opposing forces counteracts the external force, leading to a mean balance of the forces acting on the group of particles. As such, the convection velocity of the affected groups becomes constant. Nevertheless, as long as the convection is not zero, energy will still be added to the ensemble at a linear rate.

As soon as this stage is reached actual measurements become possible. The continued flux of energy can be balanced by the use of thermostats, creating a steady state for the energy and the convection. Additionally, the energy transfer at the final convection state can be used as a basis for computing the heating of the material by the external forces, which we will treat in section 3.5.

3.4.2 Error Estimation

Since we may expect that the mean kinetic energy changes proportionally to the external energy, we recall the expression for external energy transferred and its rate

$$\begin{aligned} E_{ext} &= \sum_i \int_0^t \vec{F}_i(\tau)\vec{v}_i(\tau)\, d\tau \\ \frac{\partial E_{ext}}{\partial t} &= \sum_i \vec{F}_i(t)\vec{v}_i(t). \end{aligned}$$

With correctly given and implemented external forces, those are exact and do not contribute to the error of the measurement. Consequently, the remaining source of an error of the measurement is the distribution of the particle velocities. Assigning individual particles to groups g, such that the forces are identical ($\vec{F}_p = \vec{F}_g$, if $p \in g$), we can rewrite the external energy rate as

$$\begin{aligned} \frac{\partial E_{ext}}{\partial t} &= \sum_i \vec{F}_i(t)\vec{v}_i(t) \\ &= \sum_g n_g \cdot \vec{F}_g(t)\langle\vec{v}(t)\rangle_g \end{aligned}$$

where $\langle\vec{v}(t)\rangle_g = \frac{1}{n_g} \cdot \sum_{i\in g} \vec{v}_i(t)$. While it is intuitive to measure the convection by averaging over the ad hoc velocities of the particles, this average proves to be unreliable.

For a single time step δt and $t_0 = t - \delta t$ we can write

$$\vec{v}_i(t) = \frac{r_i(t)}{\delta t},$$

which can be used to estimate an upper bound on the standard deviation of the average velocity measurements. We consider the variance of the velocity measurement and insert (3.5)

$$\begin{aligned}
\sigma^2(\vec{v}_g) &= \frac{1}{n_g} \cdot \sum_{i \in g} (\vec{v}_i - \langle \vec{v} \rangle)^2 \\
&= \frac{1}{n_g} \cdot \sum_{i \in g} \frac{(\vec{r}_i - \langle \vec{r} \rangle)^2}{\delta t^2} \\
&\approx \frac{1}{\delta t} \left\langle \frac{\partial \langle L^2 \rangle}{\partial t} \right\rangle \\
&= \frac{6}{\delta t} \cdot D_g,
\end{aligned}$$

with D_g being the diffusion coefficient of group g. Since the diffusion coefficient is expected to assume a constant value for a given ensemble and with the time steps usually used in Molecular Dynamics, this variance may become very large, even several magnitudes larger than the actual measured value.

Fortunately, considering long term behavior over longer time intervals allows for better estimates. Considering the single particle convection

$$\vec{w}_i(t) = \frac{r_i(t)}{t}, \tag{3.8}$$

we can write the external energy for constant $\vec{F}_g$ as

$$\begin{aligned}
E_{ext} &= \sum_g n_g \cdot \int_0^t \vec{F}_g(\tau) \langle \vec{v}(\tau) \rangle_g \, d\tau \\
&= \sum_g n_g \vec{F}_g \cdot \langle \vec{r}(t) \rangle \\
&= \sum_g n_g \vec{F}_g \cdot \int_0^t \frac{\langle \vec{r}(t) \rangle}{t} \, d\tau \\
&= \sum_g n_g \vec{F}_g \cdot \int_0^t \langle \vec{w}(t) \rangle \, d\tau.
\end{aligned}$$

This time we consider the variance of $w(t)$, resulting in the expression

$$\begin{aligned}\sigma^2(\vec{w}_g) =& \frac{1}{n_g} \cdot \sum_{i \in g} (\vec{w}_i - \langle \vec{w} \rangle)^2 \\ =& \frac{1}{n_g} \cdot \sum_{i \in g} \frac{(\vec{r}_i - \langle \vec{r} \rangle)^2}{t^2} \\ =& \frac{6}{t} \cdot D_g.\end{aligned}$$

As before, the diffusion coefficient is expected to assume a finite value so that increasing the ensemble size is only of limited value, since the number of particles does not appear in the estimate. Consequently, the runtime needs to be increased to reliably reduce the standard deviation of the velocity measurement. Moreover, since the standard deviation σ is the square root of the variance, a decrease of error can only be expected with $\frac{1}{\sqrt{t}}$, since

$$\sigma(\vec{v}_g) = \sqrt{\frac{6 \cdot D_g}{t}}.$$

In summary we obtain an estimate of the maximal error [BSMM01] of the external energy

$$\Delta_{max} \left(\frac{\partial E_{ext}}{\partial t} \right) = \sum_g \left| n_g \vec{F}_g \right| \sqrt{\frac{6 \cdot D_g}{t}}. \tag{3.9}$$

Using the error estimate for the convection velocities in the Gaussian law error propagation [BSMM01] we also obtain an expression for the variance of the rate

$$\sigma^2 \left(\frac{\partial E_{ext}}{\partial t} \right) = \sum_g (n_g \vec{F}_g)^2 \cdot \frac{6 \cdot D_g}{t}. \tag{3.10}$$

These results stands in remarkable contrast to the estimate on the error for the diffusion measurement. As elaborated in [Neu10], using results from [Sac88], the error of the diffusion measurement can be estimated in the number of particles, while an increase in simulation time only seems to average over the errors of the snapshots in time.

In both cases, it is nevertheless reasonable to expect a decrease of the uncertainty of the measurement by both larger ensembles and longer simulation times, however standard methods fail in quantifying this decrease.

Accelerating Convergence

In light of the above error estimate and the slow guaranteed convergence, we want to discuss possible remedies by convergence accelerating methods. [CCC+03] introduces

a convolution technique, which makes use of functions used in signal filtering. The technique requires that the area of convergence is reached and the original rate of convergence in time is $\mathcal{O}(\frac{1}{T})$ and allows to reach $\mathcal{O}(\frac{1}{T^k})$ for arbitrary $k \in \mathbb{N}_+$. However, it is not applicable to measurements whose original convergence rate is slower, as it is with our case which only guarantees $\mathcal{O}(\frac{1}{\sqrt{T}})$. Furthermore the authors themselves point out for their method, that while errors are reduced on the sampled trajectory, the sampled phase space remains unchanged, which is the primary obstruction in complex examples.

Approaches which aim to increase the sampling area are umbrella sampling and replica exchange methods. Both methods have been advanced from their early beginnings in the 1980s [ED05] and recently have been combined [NMRP13]. This approach promises to reduce both the statistical and systematic error in MD simulations and – for the example demonstrated in the paper – gives reasonable predictions for autocorrelation times larger than the individual simulation times. However, the combined simulation times still exceed the estimated correlation times by up to two orders of magnitude, which would be of limited use in our settings.

3.5 Upscaling of Temperature Generation

The control of temperature within MD systems is a topic which has been investigated intensely [EH85, Nos91]. A significant portion (if not the majority) of this research is targeted at controlling the temperature of MD systems via some explicit (e.g. Nosé-Hoover type) or implicit (e.g. Berendsen type) coupling of the ensemble with a virtual outer "heat bath" or reservoir. However, these couplings generally do not model a specific physical interaction but strive to model the effect of such an interaction.

Specific external interactions with individual particles with the purpose of observing the heat flow have previously been treated as abstracted cases of color fields [BEC93]. While not modeling an actual physical coupling process, attempts were made to establish controlled heat addition in [Had99], which were inspired by the Berendsen type thermostat. However, the scaling factor for the impulses does not properly match the energy addition, missing the quadratic relation between velocities and energy. We will present the correct energy computation from impulse scaling in section 3.6.1.

In this context it is important to distinguish the terms heat and temperature more thoroughly. While in the past temperature was only a macroscopic concept, the equivalence to the kinetic energy of the material

$$T = \frac{2}{3Nk_B} \sum_i \frac{m_p}{2} \vec{v}_p^2 = \frac{2}{3N} E_{kin} \tag{3.11}$$

has now long been established and is called the absolute temperature [Dem04a]. This equation leads to the relation of temperature and energy.

Heat is an expression for energy which does not correspond to a measurable variable of the system, but is defined over the change of other variables, with the most straight forward being the first law of thermodynamics, expressing heat Q as the difference between the change of internal energy δU of a system and the work W it produced

$$Q = \delta U - W.$$

However, the amount of heat transfered to or from a system does not convert directly to a change in temperature via (3.11). This becomes apparent, when no macroscopic work is performed. Then the amount of heat equals the change in the internal energy of an ensemble, which is defined by the sum of change in kinetic and potential energy [TME12]. Thus only a fraction of the energy supplied changes the temperature of the ensemble, with the ratio determining another material property, the heat capacity. While this heat capacity is a universal constant for ideal monoatomic gases, it is subject to change for other materials, depending on the exact configuration and equilibrium conditions of the ensemble. As such there is no analytical formula to derive the heat capacity from the microscopic states, instead it has to be extracted from the behavior of the macroscopic variables.

In light of the above – particularly in the context of energy transfer via external forces – the heat generation can be accessed via two different approaches. First, for all settings, the rate of change in the kinetic energy itself can be computed for a direct conversion to the rate of change in the temperature of the ensemble

$$\frac{\delta T}{\delta t} = \frac{2}{3Nk_B}\frac{E_{kin}}{\delta t} =: \beta(F_{ext}).$$

A different approach depends on the fact that with our new computations of all external energy contributions the externally transfered energy can be summed up to determine the exchanged heat, and the resulting temperature can be calculated via the heat capacity $C := \frac{Q}{\Delta T}$ of the ensemble material

$$\frac{\partial T}{\partial t} = \frac{1}{C}\frac{\partial E_{ext}}{\partial t}.$$

While the latter is trivially known from the setup of the ensemble, the prior needs to be supplied externally or additionally computed from the simulation, with the computation method depending on the ensemble of the simulation [AT89]. The heat capacity as defined above is of limited functional value, as it does not take the amount of substance into account. Several normalizations are in use, which take a proportionality with the material amount into consideration, such as volumetric heat capacity $[C_V] = \frac{J}{K \cdot m^3}$, molar heat capacity $[C_m] = \frac{J}{K \cdot mol}$ and specific heat capacity $[C_s] = \frac{J}{K \cdot kg}$. Particularly the latter is widely found in literature and textbooks. In order to set this into relation with the Molecular Dynamics calculation of energy, we consider the density ρ of the material and the volume V of the ensemble

$$C_s \cdot \rho \cdot \frac{\partial T}{\partial t} = \frac{1}{V}\frac{\partial E_{ext}}{\partial t}.$$

3.5.1 Einstein-Smoluchowski Equation

For complex materials the above equations converge only slowly. The reason lies in the estimate of the energy transfer we presented in section 3.4.2. As the convergence of the energy transfer is bound by the diffusion coefficients and only converges with $\frac{1}{\sqrt{t}}$, we either require large amounts of computational ressources, or we need to employ indirect means of scaling, requiring additional information. As such, upscaling of the generated heat may also be obtained by making use of the macroscopic Einstein-Smoluchowski equation. This equation relates the ion mobility μ_g with the diffusion coefficient of the respective ion type g

$$\mu_g = \frac{D_g}{k_B T}.$$

The mobility allows us to compute the convection velocity of the respective species

$$\langle v \rangle_g = \mu_g \cdot \vec{F}_g,$$

which in turn permits the computation of the transfered energy

$$E_{ext} = \sum_g \int_{t_0}^{t} \langle v \rangle_g \vec{F}_g \, d\tau.$$

Thus the temperature upscaling with the heat capacity takes the form

$$C \cdot \frac{\partial T}{\partial t} = \frac{\partial E_{ext}}{\partial t} = \sum_g |g| \cdot \langle v \rangle_g \vec{F}_g.$$

As noted in the previous section, it is prudent to account for the amount of material, so we make use of the specific heat capacity

$$C_s \cdot \rho \cdot \frac{\partial T}{\partial t} = \frac{1}{V} \frac{\partial E_{ext}}{\partial t} = \frac{1}{V} \sum_g |g| \cdot \langle v \rangle_g \vec{F}_g. \tag{3.12}$$

Having a specific application in mind, we examine the above relations in the case where the external forces are generated by a homogenous electric field. We obtain the force on a particle in group g by taking the spatial derivative of the field and multiplying with the particle charge z_g, resulting in

$$\vec{F}_g(\Phi) = z_g \cdot \nabla \Phi.$$

Consequently the expression for the convection velocity now reads

$$\langle v \rangle_g = \mu_g \cdot \vec{F}_g(\Phi) = \mu_g \cdot \nabla \Phi z_g. \tag{3.13}$$

Inserting the above into the general equation (3.12) we obtain

$$C_s \cdot \rho \cdot \frac{\partial T}{\partial t} = \frac{1}{V} \sum_g |g| \cdot \langle v \rangle_g \cdot z_g \cdot \nabla \Phi.$$

By combining groups of particles, we convert the sum over individual particles divided by volume into a particle density $c_g = \sum_{i \in g} \frac{1}{V} = \frac{|g|}{V}$. This gives us the current density of the ionic charges

$$\vec{j} = \sum_g z_g c_g \langle v \rangle_g,$$

which by equation (3.13) is aligned with the electric field $E = \nabla \Phi$. Thus our thermal source becomes

$$\begin{aligned} C_s \cdot \rho \cdot \frac{\partial T}{\partial t} &= \vec{j} \cdot \nabla \Phi = \frac{1}{V} |\vec{I}| \cdot |\nabla \Phi| \\ \Leftrightarrow C_s \cdot M \cdot \frac{\partial T}{\partial t} &= |\vec{I}| \cdot |\nabla \Phi|, \end{aligned}$$

which corresponds to classical Joule heating [Dem04b].

Of course there are other effects which connect heat generation and currents, such as the Seebeck and the Peltier effect. However, these effects are the result of interface dynamics of different materials and thus not trivially accessible in our setting. Fortunately, it has been found that these contributions are minor compared to the Joule heating [LZ15], making the macroscopic scaling here particularly useful in electric applications.

3.6 Steady State Detection

The results in the previous sections allow us to compute the energy exchanged between the open system under investigation and its surroundings. While the use of an open system abandons the stage of equilibrium Molecular Dynamics, our goal is to perform steady state simulations instead. Up to now we have not yet discussed how we determine the presence of a steady state, while the system under observation exchanges energy with the external system.

Due to their complex nature, we are not able to provide a recipe that enables the creation of steady states in arbitrary physical systems in flux. However, in this section we will present criteria to determine whether a given system has reached steady state with respect to the energy exchanged between the system itself and some connected outer system(s). In particular, we will investigate coupling with external heat baths (thermostats) and external driving forces on the particles.

In essence, the detection of a steady state requires the detection of a balance of the energy brought into the system vs. the energy extracted from the system. We

will generally expect that the energy is dissipated via the thermostat and added via external forces on the particles. From a mathematical point of view, this behavior can also be inverted, but generally this is not reflected in physical reality, see the discussion in section 2.2.3.

We compute the dissipated energy E_{dis} from the change in the kinetic energy induced by the thermostat

$$\delta E_{dis} = \delta E_{kin,therm}.$$

First we note that this does not necessarily correspond to the total change in the kinetic energy or temperature

$$\delta E_{dis} \neq \delta E_{kin} = \frac{3}{2} N k_B \delta T,$$

since there may be natural fluctuations within the ensemble as well as a loss of energy due to the modeled outside interaction.

Furthermore, it is not necessary that all energy added to the system over time needs to be dissipated, since the steady state may be assumed with a higher energy than the system initially held. Additional energy may be stored in the potential energy by rearrangement of the atomic configurations, which would not be accessible in the equilibrium state. Relevant is the rate of energy added/extracted from the system, which corresponds to the time derivative

$$\frac{\partial E_{dis}}{\partial t} = \frac{\partial E_{kin,therm}}{\partial t}$$

of the energy change.

In the application of computer simulations, the derivative is replaced by the difference quotient with a small time step δt, suitable to the time scale of the simulation. The primary key to the analysis is the separation of the change of kinetic energy in inner and outer contributions. The inner contributions are the result of the positions and interactions of the atoms in the system itself and are balanced by a change in the potential energy of the system. Thus, while they may change the kinetic energy, they do not contribute to the exchange of energy with the external system.

The outer contributions can again be separated into two contributions, one by the thermostat and one by the external forces. It is those that we wish to balance and thus it is important that the measurements of either contribution is separated. The contributions by external forces can be computed as detailed in section 2.3.2. The computation of the thermostat energy depends on the particular choice of the thermostat.

The ad hoc values of these rates need to be averaged, as energy fluctuations in the ensemble are natural. In order to determine whether an energy steady state has been reached, the rate of the thermostat energy transfer and the rate of other external

energy transfers need to satisfy two criteria. Naturally, we require that both values have equal magnitude. Furthermore, we require that the averages of both values themselves remain constant over time. The latter requirement needs to be checked in light of the different regimes of acceleration outlined in 3.4.1, as long as the forces are not balanced, the configuration of the system may still be in a transient state.

3.6.1 Energy of Berendsen Thermostat

The Berendsen thermostat functions by scaling all particle velocities equally by a factor β. This factor is computed such that a predefined kinetic energy is reached exactly after scaling. In the general use of the thermostat, this scaling is not applied every time step, but generally allows for some time for equilibration before the next scaling. However, the scaling with factor $\beta = 1$ is indistinguishable from no scaling taking place and thus, without loss of generality, we may assume in the following discussion that some $\beta(t)$ is applied in every time step t. In order to scale to a desired temperature T_D, we compute

$$\beta(t) = \begin{cases} \sqrt{\frac{E_{kin,\,D}}{E_{kin}}} = \sqrt{\frac{T_D}{T}} & \text{if } t \text{ is a scaling time step} \\ 1 & \text{if } t \text{ is a non-scaling time step.} \end{cases}$$

Let now $\vec{v}_i(t)$ be the velocity of the particle i prior to scaling, then we define

$$\vec{v}_{i,\beta}(t) = \beta \cdot \vec{v}_i(t),$$

the velocity after scaling. Consequently, the difference of the kinetic energies, which is absorbed in the thermostat at a single time step, computes to

$$\begin{aligned} \Delta E_{therm}(t) = E_{kin}(t) - E_{kin,\beta}(t) &= \frac{1}{2}\sum_i m_i \vec{v}_i^2(t) - \frac{1}{2}\sum_i m_i \vec{v}_{i,\beta}^2(t) \\ &= \frac{1}{2}\sum_i m_i \left(\vec{v}_i(t)^2 - \vec{v}_{i,\beta}(t)^2\right) \\ &= \frac{1}{2}\sum_i m_i \left(\vec{v}_i(t)^2 - \beta(t)^2 \vec{v}_i(t)^2\right) \\ &= \frac{1}{2}\sum_i m_i \left(1 - \beta(t)^2\right) \vec{v}_i(t)^2 \\ &= \left(1 - \beta(t)^2\right) E_{kin}(t). \end{aligned}$$

The total energy stored in the thermostat can then be written as

$$E_{therm}(t) = \sum_{n=0}^{N_t} \left(1 - \beta(t_n)^2\right) E_{kin}(t_n),$$

with $N_t \cdot \delta t = t$.

For the actual detection of a steady state, we are interested in the rate of energy transfer, which corresponds to the power exchanged between both systems. It may appear trivial to write the power exchanged as

$$P_{therm}(t) = \frac{\Delta E_{therm}(t)}{\delta t} = \frac{(1 - \beta(t)^2)\, E_{kin}(t)}{\delta t},$$

however, in cases where the thermostat is not applied in every time step, this formula neglects the time interval between the subsequent scaling applications. As a consequence, if the time interval between scaling applications is denoted by $\Delta t = \delta t \cdot n_{\Delta t}$, we modify the formula to

$$P_{therm}(t) = \frac{\Delta E_{therm}(t)}{\Delta t} = \frac{1}{n_{\Delta t}} \sum_{n=0}^{n_{\Delta t}} \frac{(1 - \beta(t_n)^2)\, E_{kin}(t_n)}{\delta t}.$$

With Δt chosen as the interval of the rescaling algorithm, this is the ad hoc rate at which energy is stored in the thermostat. As an ad hoc factor it is still bound to fluctuate over the time of the simulation. Choosing longer times for Δt allows us to compute an average over multiple thermostat operations, and these values must approach a constant value equal to the energy flux via other external interactions in order to finally enable us to establish whether a steady state has been reached.

3.6.2 Energy of Nosé-Hoover Thermostat

In contrast to the above described Berendsen thermostat, the energy of the Nosé-Hoover thermostat is already subject of the original derivation and implementation of the thermostat.

By performing the substitutions π_s to $\xi = \frac{s\pi_s}{Q}$ and $\eta = ln(s)$, we are able to eliminate the time scaling from the extended Nosé-Hoover Hamiltonian from equation (2.8) to

$$\mathcal{H} = \sum_i \frac{\vec{p}_i^2}{2m_i} + U(\vec{q}) + \frac{Q\xi^2}{2} + gk_BT\,\eta.$$

In addition to the physical energies, we will call the Hoover kinetic energy

$$E_{kin,\,Hoover} = \frac{Q\xi^2}{2}.$$

Furthermore, we have the Hoover potential energy by

$$E_{pot,\,Hoover} = gk_BT_D\eta$$

with $\dot{\eta} = \xi$ and $\eta(t_0) = 0$. The total extended energy

$$\begin{aligned} E_{extended} &= E_{kin} + E_{pot} + E_{kin,\,Hoover} + E_{pot,\,Hoover} \\ &= E_{phys} + E_{therm} \end{aligned}$$

is a constant of the Nosé-Hoover Molecular Dynamics, despite the fact that the system itself is no longer Hamiltonian in nature [BLL99][5].

Thus the thermostat energy is given by

$$E_{therm} = \frac{Q\xi^2}{2} + gk_BT_D\eta,$$

where both ξ and η are already computed in the simulation.

From this expression, it is easily possible to compute the ad hoc energy transfer rate from the variables already computed for the equations motion

$$\begin{aligned}\frac{\partial E_{therm}}{\partial t} &= gk_BT_D\dot{\eta} + \frac{Q}{2}2\xi\cdot\dot{\xi} \\ &= gk_BT_D\xi + Q\xi\cdot\dot{\xi}.\end{aligned}$$

However, even in the equilibrium setting the kinetic energy is bound to oscillate, with the main frequency depending on the thermostat mass Q. Thus it is advisable to use time averages for the rate of the thermostat energy. While the relations between the mass and the frequency are estimated for the ensemble without external forces, it is reasonable to assume the wavelength derived from these estimates as a lower bound for the averaging operators. For a given target kinetiv energy E^D_{kin} the main oscillation wavelength is

$$\lambda = \sqrt{\frac{Q}{2E^D_{kin}}},$$

see also [MKT92][6].

[5] Here we presented the equations without external forces. In the case of external forces, we begin with the Hamiltonian from equation 2.18 and the extended energy becomes $E_{extended} = E_{kin} + E_{pot} + E_{ext} + E_{kin,\,Hoover} + E_{pot,\,Hoover}$.

[6] Note that the cited paper gives a different leading factor to the kinetic energy and the selection of thermostat mass is described as a rough estimate. Furthermore there is room for interpretation of what constitutes the *main* oscillation wavelength (or frequency), since in practical applications harmonic oscillations are present.

4 The System of the Extended Heat-Poisson-Nernst-Planck Equations

After having discussed the atomistic simulation of ion migration and the upscaling from the respective results to macroscopic variables, we now turn towards the continuous equations on the macroscale, the Heat-Poisson-Nernst-Planck system.

These equations are at the center of various applications, among those are biological ion channels, semiconductors and battery cells. The coupling of all three equations yields a system which we no longer can characterize in the traditional forms, as we join the parabolic operator of the heat equation, the elliptic operator of the Poisson equation with the Nernst-Planck equation, which by itself may be of parabolic or hyperbolic type, depending on the coefficients [MB06]. The nonlinearity of the equations and their reciprocal coupling pose further challenges to solving the equation system.

Up until recently, the dynamics of temperature have been largely ignored, only considering the Poisson-Nernst-Planck (PNP) system with constant temperature T. Previous works which computed thermal dynamics did so with respect to the macroscopic variables of total current and state of charge [SDB+13]. While several publications exist which describe the modeling of the coupling of thermodynamics and ion migration e.g. [LZ11], at the time of writing only a single implementation of such a coupling is known, which restricts the application to charge neutral binary systems [LZ15].

Our approach consists of a more general system, which has not been studied in the literature so far, allowing for an arbitrary number of species as well as charge separation. As a consequence, our approach will be suitable not only for a small set of narrowly defined applications, but for different problems on multiple scales, as we will demonstrate in chapter 5.

We begin this chapter by introducing the system of the Heat-Poisson-Nernst-Planck equations, as we intend to solve it, and continue with an overview over the current state of research of analysis and numerical solutions of related systems, in particular the Poisson-Nernst-Planck subsystem. Subsequently we present our discretization scheme and the numerical methods which we employ to solve the combined system of equations.

4.1 Modeling

We begin by discussing the individual equations and the physical processes they describe. For the first part, leading to the Nernst-Planck and Poisson equation, we will follow our previous derivation in [Neu10].

The Nernst-Planck equation describes the time evolution of ion concentrations based on their diffusive and convective migration. For multiple species of ions with concentrations $c_0, ..., c_{n-1}$ within one setting, separate equations need to be assembled with matching coefficient functions, which we will index by i. In the course of this thesis, we will assume that all particles have access to the same spatial domain $\Omega \subset \mathbb{R}^d$ during the time interval $[0, t_{end}] \subset \mathbb{R}$. The diffusive flux $\vec{J}_{D,i}$ is described by

$$\vec{J}_{D,i} = -D_i \nabla c_i(x,t), \tag{4.1}$$

with $c_i(x,t)$ being the concentration function and D_i the function of the diffusion coefficient.

The convective flux has separate contributing terms. These share the common structure

$$\vec{J}_{conv,i} = \vec{v}_i \cdot c_i = \nu_i \vec{F}_i \cdot c_i, \tag{4.2}$$

where $\vec{v}_i$ denotes the convection velocity, which is driven by the force $\vec{F}_i$ scaled by the mobility of the species ν_i. The mobility of an ion species is given by the Einstein-Smoluchowski relation already discussed in section 3.5.1,

$$\nu_i = \frac{D_i}{k_B T}, \tag{4.3}$$

where k_B is the Boltzmann constant and T the temperature of the system.

In the classical setting, the convection of the charged particles is only driven by the electric field Φ, with the force acting on a single ion determined by its charge number z_i

$$\vec{F}_{e,i} = -z_i \cdot e \cdot \nabla \Phi, \tag{4.4}$$

where e denotes the electron charge. Combining equations (4.2), (4.3) and (4.4) and considering forces on a per mole instead of a per particle basis, we obtain the convective term driven by the electric interaction

$$\vec{J}_{e,i} = -\frac{D_i z_i F}{RT} \nabla \Phi c_i(x,t) \tag{4.5}$$

with the Faraday constant F taking the place of e and the gas constant R taking the place of k_B.

However, the electric field is not the only driving factor for the concentrations. Another directed influence can be derived from the chemical potential[1], the gradient of which can be interpreted as a force term. Thus we obtain an additional convection term

$$J_{\mu,i} = -\frac{D_i}{RT}\nabla\mu c_i(x,t), \tag{4.6}$$

where the mobility is considered in terms of moles as well.

In order to connect the flux with the time evolution of ion concentrations, we consider the continuity equation

$$\frac{\partial c_i}{\partial t} = -\nabla\vec{J}_{tot}. \tag{4.7}$$

By summing the flux components from equations (4.1), (4.5) and (4.6) and inserting them into equation (4.7), we obtain the extended Nernst-Planck equation

$$\frac{\partial c_i}{\partial t} = \nabla\left[D_i\left(\underbrace{\nabla c_i}_{\text{diff}} + \underbrace{\frac{z_i F}{RT}c_i\nabla\Phi + \frac{1}{RT}c_i\nabla\mu_i}_{\text{conv}}\right)\right]. \tag{4.8}$$

As the ions are charged themselves, the sum over the charge concentrations $\sum_i z_i c_i$ may lead to local non-zero charges. Depending on the net sign, these act as sources or sinks of an electric potential on the same domain, leading to the Poisson equation

$$-\Delta\Phi = \frac{F}{\varepsilon}\left(\sum_i z_i c_i + Q\right). \tag{4.9}$$

Here $\varepsilon = \varepsilon_0 \cdot \varepsilon_r$ denotes the dielectricity, with ε_0 being the permittivity of free space and ε_r being the material modifier. Q may denote an additional background charge distribution, which is not subject to migration.

The last equation we need to complete the system is the heat equation. Since there are plenty of sources for its derivation in standard text books, e.g. [Dem04a, TME12], we will not give a general derivation here, but point to our upscaling methods for the temperature creation through external forces from section 3.5. The heat generation term is added as a source term to the heat equation and couples the temperature evolution to the ion convection, resulting in

$$\frac{\partial T}{\partial t} = \alpha\Delta T + \beta(c,\Phi). \tag{4.10}$$

[1] In some publications, the extra convection is derived from the chemical activity. The chemical activity a and chemical potential μ are related via $RT\ln a = \mu - \mu_0$ [Coh07].

In contrast to the previous equations, we allow the solution to exist on an extended domain $\Omega_T \supseteq \Omega$.

The above equations are not a complete description of the modeled system, they require initial and boundary conditions to be closed. Since these vary with the exact application, we will not include them in this overview, but discuss those which we actually use in context of the relevant example in chpater 5. We will however discuss the different classes of mathematical boundary conditions in section 4.3.4 of this chapter.

Summary

We will now summarize our above derivations to present the system which we intend to solve. In the following, we will use the notation

c_i: concentration	α: thermal diffusivity
Φ: electrical field	R: ideal gas constant
T: temperature	ε: dielectric constant
D_i: diffusion coefficient	F: Faraday constant
μ_i: chemical potential	z_i: ion charge number
β: heat source	Q: background charge.

The Nernst-Planck equation (4.11) is present once for each of the n ion species and models the time evolution of each species concentration c_i.

So in collection we present the system of the Heat-Poisson-Nernst-Planck equations as we intend to solve it

$$\frac{\partial c_i}{\partial t} = \nabla \left[D_i \left(\nabla c_i + \frac{z_i F}{RT} c_i \nabla \Phi + \frac{1}{RT} c_i \nabla \mu_i \right) \right] \tag{4.11}$$

$$-\Delta \Phi = \frac{F}{\varepsilon} \left(\sum_i z_i c_i + Q \right) \tag{4.12}$$

$$\frac{\partial T}{\partial t} = \alpha \Delta T + \beta(c, \Phi). \tag{4.13}$$

4.1.1 Nondimensionalization

In order to better analyze the numerics of the system, it is sensible to study the equations independent of scale and units. This process is called nondimensionalization and its results assist in identifying problematic coupling constants towards improving the condition of the numerical problem. While the influence of selections of units of the parameters can be removed by nondimensionalization, we will see that the coupling can be affected by the magnitude of the respective values. For reasons which will become apparent to the reader in section 4.3.3, we will consider the Poisson and

Nernst-Planck equations separately from the heat equation and treat the temperature in the Nernst-Planck equation as a constant parameter instead of a variable.

Starting from the Poisson-Nernst-Planck equation system we substitute all variables with a dedimensionalized variable (denoted with a tilde) and a factor carrying the reference magnitude and units

$$\begin{aligned} c &= \tilde{c} \cdot \bar{c} \\ \Phi &= \tilde{\Phi} \cdot \bar{\Phi} \\ x &= \tilde{x} \cdot L \\ t &= \tilde{t} \cdot \tau. \end{aligned}$$

Rescaled functions are expected to be dependent on rescaled arguments only, so

$$c(x,t) = \tilde{c}(\tilde{x},\tilde{t}) \cdot \bar{c}. \tag{4.14}$$

Generally we need to ensure that the differential operators are also suitably replaced in order to still solve the same problem. Thus when we make substitutions for any space dependent function $u(x) = \bar{u}\tilde{u}(\tilde{x})$, we have the following dedimensionalized differential operator

$$\begin{aligned} \nabla_x u(x) &= \bar{u}\nabla_x \tilde{u}\left(\frac{x}{L}\right) \\ &= \bar{u}\frac{1}{L}\tilde{u}'\left(\frac{x}{L}\right) \\ &= \bar{u}\frac{1}{L}\tilde{u}'(\tilde{x}) \\ &= \bar{u}\frac{1}{L}\nabla_{\tilde{x}}\,\tilde{u}(\tilde{x}). \end{aligned}$$

Thus we have $\nabla_x = \frac{1}{L}\nabla_{\tilde{x}}$ and similarly $\frac{d}{dt} = \frac{1}{\tau}\frac{d}{d\tilde{t}}$. We will denote $\nabla_{\tilde{x}}$ as $\tilde{\nabla}$ and $\Delta_{\tilde{x}}$ as $\tilde{\Delta}$.

We get the rescaled system

$$\begin{aligned} \bar{c}_i\frac{1}{L}\tilde{\nabla}\left(D_i\frac{1}{L}\tilde{\nabla}\tilde{c}_i + D_i\kappa z_i\tilde{c}_i\tilde{\nabla}\tilde{\Phi} + D_i\pi\tilde{c}_i\right) &= \bar{c}_i\frac{1}{\tau}\frac{d\tilde{c}_i}{d\tilde{t}} \\ \frac{F}{\varepsilon}\sum_i z_i\bar{c}_i\tilde{c}_i &= \frac{1}{L^2}\bar{\Phi}\tilde{\Delta}\tilde{\Phi} \end{aligned}$$

with $\kappa = \frac{\bar{\Phi}F}{RT}$ and $\pi = \frac{\tilde{\nabla}\mu_i}{RT}$.

In the Nernst-Planck equations it is possible to completely eliminate the factors $\bar{c}_i$, as they can be factored out of all summands of the respective equations, leaving only the rescaled values. In the Poisson equation however the factors remain as they are only part of one of the summands each.

Thus we obtain the following system by shifting all unit constants to the left hand side

$$\frac{\tau}{L^2}\tilde{\nabla} D_i(\tilde{\nabla}\tilde{c}_i + \kappa z_i \tilde{c}_i \nabla\tilde{\Phi} + \pi\tilde{c}_i) = \frac{d\tilde{c}_i}{d\tilde{t}}$$
$$L^2 \cdot \frac{F}{\varepsilon \cdot \bar{\Phi}} \sum_i z_i \bar{c}_i \tilde{c}_i = \tilde{\Delta}\tilde{\Phi}.$$

After the substitution, we collect the factors to the following products

$$\lambda_i = \frac{D_i \tau}{L^2} \tag{4.15}$$
$$\sigma' = \frac{L^2 F}{\varepsilon \bar{\Phi}}.$$

Obviously, σ' is still associated with units of volume per ion amount, which require the scaling factor from the concentration functions to be nondimensionalized. However, the scaling factors of the individual concentration function are not necessarily identical, thus we split them into a common and an individual scaling parameter

$$\bar{c} \cdot \hat{c}_i = \bar{c}_i$$

which we use to truly nondimensionalize the coupling constant

$$\sigma = \frac{L^2 F}{\varepsilon \bar{\Phi}} \bar{c}. \tag{4.16}$$

The new set of equations thus takes the form

$$\tilde{\nabla}\lambda(\tilde{\nabla}\tilde{c}_i + \kappa z_i \tilde{c}_i \nabla\tilde{\Phi} + \pi\tilde{c}_i) = \frac{d\tilde{c}_i}{d\tilde{t}} \tag{4.17}$$
$$\sigma \sum_i z_i \hat{c}_i \tilde{c}_i = \tilde{\Delta}\tilde{\Phi}.$$

For the convection term, we can now easily compare the two factors κ and π in order to determine the dominant convective influence. Furthermore, these values can be used to detect convection dominance in the equation, which is known to cause instabilities. Assuming that after rescaling all tilded variables are of the order of 1, we need to observe the factors from (4.15) and (4.16) to analyze performance of the numerical integration and ensure that our numerical scheme does not run into problems due to loss of significance in summation or substraction operations. In addition, by comparison of the factors λ and σ we can observe the respective dominance of either equation in the coupled system. In particular, σ determines the stiffness of the non-linear coupling and we will see the strong impact it has on the condition of the linear system in section 5.3.2, where we will present the scale analysis.

We continue our considerations with the heat equation. Using the same scaling for spatial and temporal arguments, we only need to rescale

$$T = \tilde{T} \cdot \bar{T}, \qquad \beta(c, \Phi) = \bar{\beta} \cdot \tilde{\beta}(c, \Phi)).$$

The scaled equation thus becomes

$$\bar{T}\frac{1}{\tau}\frac{d\tilde{T}}{d\tilde{t}} = \alpha\bar{T}\frac{1}{L^2}\tilde{\Delta}\tilde{T} + \bar{\beta}\tilde{\beta}(c, \Phi)$$

which can be rearranged to

$$\frac{d\tilde{T}}{d\tilde{t}} = \frac{\alpha\tau}{L^2}\tilde{\Delta}\tilde{T} + \frac{\bar{\beta}}{\bar{T}}\tilde{\beta}(c_i, \Phi).$$

Thus we obtain similar parameters to the Nernst-Planck equation,

$$\lambda_T = \frac{\alpha\tau}{L^2}, \qquad \kappa_T = \frac{\bar{\beta}}{\bar{T}}.$$

However, due to the difference in coupling behavior – see section 4.3.3 – and the absence of a convection term, their influence on the performance of the numerical system is far less pronounced than that of the parameters of the PNP system.

We note that the scaling factor of the concentration functions has been completely removed from the dedimensionalized Nernst-Planck equation. Since it does not even appear in the coefficients any more, this may lead to the assumption that the actual scale of concentrations is arbitrary. However this is not the case, as the scaling factors appear in the Poisson and Heat equations and influence the Nernst-Planck equation via the coupling.

4.1.2 Stochastic Modeling as an Alternative Approach

While we focus on the solution of the coupled partial differential equations, we would like to point the reader to the fact that alternative approaches are also viable. Stochastic methods for atomistic and ion-based behavior have been developed for decades, beginning with reaction modeling for particle solutions by characterizing the interaction of particles of certain types as an event and assigning probabilities to the different possible events based on the rate or timescale with which these events occure in reality [Gil76, Gil77]. While the first of these approaches were limited to reactions in homogeneous solutions, the algorithms were later extended to incorporate diffusion in spatial concentration by introducing compartments. Consequently, events were extended to include the motion of particles between adjacent cells [Two07]. By modifying the rates of these events depending on additional – possibly coupled – functions, non-constant diffusion coefficients can be simulated [LDP08]. In essence the latter work

presented the necessary formulas for convection-like driving forces in its treatment of non-constant diffusion coefficients, but explicit treatment of convection modeling within this class of algorithms was presented in [MK02, PJD+13]. While these publications deal with different underlying models of climate and cloud simulations, they are based on the same original algorithmic ideas.

The combination of the above results allows for a complete stochastic treatment of the ion flux, however it is the coupling with the other quantities of the system which hides the challenges of this approach. Both the heat and the electric potential are inherently continuous in nature, making the modeling via rates of events problematic. While the simulation of reaction diffusion systems was transferred to solving the one-dimensional heat equation in [Ber05], several issues remained, among which were mutually exclusive restrictions on cell sizes, which may be caused by separations of timescales. While the existence of such a separation between the Nernst-Planck and the heat equation depends on the exact coefficients in the equation, a separation is always present between the Poisson and the other equations, evidenced by the missing time dependence in the Poisson equation.

Another stochastic approach encountered in the applications of ion migration, particularly biological ion channels, is the modeling involving Markov chains [TL16]. These often describe a general system state and are coupled with additional differential equations equations in order to give a full physical model of the physical or biological process.

4.2 State of the Art

The extended Heat-Poisson-Nernst-Planck system given in equations (4.11) - (4.13) has not been studied so far in previous literature. The closest resemblence is found in [LZ15], where a reduced two species model is coupled with an extended heat equation. Nevertheless, we will give a review of several results with respect to related systems, their modeling requirements and numerical approaches, as these remain relevant to our problem within limits.

Most of the literature in the following section will not use our extended Nernst-Planck equation (4.11), but a variant replacing the physical with an arbitrary coefficient in the coupling term and additionally dropping the chemical potential

$$\frac{\partial c_i}{\partial t} = \nabla \left[D_i \left(\nabla c_i + \alpha_\Phi c_i \nabla \Phi \right) \right]. \tag{4.18}$$

4.2.1 Existence and Uniqueness

One of the predominant questions when dealing with the solution of partial differential equations is the existence of solutions and their uniqueness. The general difficulty of this question is illustrated by the state of research with respect to the well-known

Navier-Stokes equations. These fundamental equations of fluid dynamics are of significant importance for various applications in science and engineering (and even in remote areas such as entertainment industry), nevertheless the existence of solutions to these equations in three dimensions remains unproven and has been added to the seven Millennium Prize Problems published by the Clay Mathematics Institute [Fef00][2].

For the system of Poisson-Nernst-Planck equations several approaches have been made and for a variety of related systems results have been achieved under some specific assumptions. In the following sections we will outline these results and their requirements, as well as their applicability to the system which we investigate.

While general existence of a solution for the time dependent two species problem of the Poisson-Nernst-Planck system was shown in [Jer85] and a powerful uniqueness result was established in [Gaj85], later investigations have shown that the question of uniqueness has not yet been satisfactorily solved for all problems of interest. In particular, it can be shown that under certain conditions multiple solutions exist, even for the steady state two species case and more so for multiple species systems [Liu09]. There is some speculation in the literature, whether all but one of such multiple solutions are unphysical – e.g. by producing negative concentration values. For the case of Dirichlet problems, asymptotic solutions can be constructed and it has indeed been shown that the physical solutions are unique for up to three ion species [WHWH14]. For cases of more than three ion species or differing boundary conditions and exact solutions, the question of uniqueness remains open.

One-Dimensional Steady State

Several investigations have been performed for the one-dimensional case, with particular emphasis on the steady state system.

While the existence of steady state solutions is generally affirmed [Liu05], the question of uniqueness is the center of ongoing research. With additional requirements, such as constant coefficients, positive Dirichlet boundary conditions and vanishing background charges, uniqueness of the solution for the steady state equations was shown in [PJ97]. In fact, the authors were even able to show that the resulting solutions must be positive almost everywhere.

Later publications indicate that such strict requirements are indeed necessary. Inspired by biological channel systems, non-zero background charges were investigated in [Liu09]. Analyzing the equations as a singular perturbed system, the author concludes that multiple solutions may exist for a variety of conditions placed on the system, and that negative values may be assumed by the solution functions. Specifically, even for a set of only two species, solutions must not be unique and in the case of

[2] Some partial results have been achieved during the runtime of the twentieth century. Among those are existence and smoothness in two dimensions, existence for a limited (and starting condition dependent) time [Fef00].

more than three species results become even more varied. These variations may also include solutions with negative concentration functions, and while the author states that he expects (unique) solutions with positive concentrations to exist, he does not give reasons to support this expectation.

Three-Dimensional Non-Steady Systems

As noted in the introduction, for the dynamic system in physical space – $\Omega \times [0, T]$ with $\Omega \subset \mathbb{R}^3$ – the existence of a unique solution was shown in [Gaj85]. In light of the results for the one-dimensional steady state, the result is quite powerful, as it permits non-vanishing background charges and additional reaction rates. Nevertheless, these two results do not stand in contradiction, as several additional requirements are placed on the initial conditions, the coefficient functions, the reaction rate and the boundary conditions. The results are limited to two species systems, making no indication of their validity for equation systems of multiple species.

Related Equation Systems

Due to the fact that we are investigating an extension of the Poisson-Nernst-Planck system, we would like to have a result for the existence and uniqueness of this particular system. However, to the best of our knowledge such a result has not yet been presented. Nevertheless, other extended systems have been investigated and the results shall be shortly summarized, specifically as we will encounter the first proof of uniqueness for a system of multiple species. The Stokes-Nernst-Planck-Poisson system is created from the classical PNP setting by considering hydrodynamic convection of the solvent and consequently adding the Stokes equation. By homogenization, the related Darcy equation is derived, yielding the Darcy-Nernst-Planck-Poisson system.

A proof is presented for the existence of unique weak solutions of the Darcy-Nernst-Planck-Poisson system, where the authors specifically deal with the case of non-electroneutrality. However, the conditions under which these results hold demand that the spatial dimension of the problem is either two or three and that the spatial boundary conditions must be Dirichlet values [HRK12]. While the initial results were limited to the two species case, a later work extended this result to multicomponent solutions, being indeed the first work to prove the existence of unique solutions to such systems [Her14].

4.2.2 Reduced Models

Several attempts at the modeling of batteries turn to a simplification of the model from a two species system to a one species equation, of which at least two different approaches exist.

The first approach relies on the argument that the strong coupling between the electric field and the individual species reduces the dispersion of charge, arguing that

the reduction is so strong that in fact it does not exist and the total charge function in the electrolyte may be considered neutral (electroneutrality assumption) [DN08]. This electroneutrality allows for an immediate relation of the species functions of the form $c_1 = \frac{|z_2|}{|z_1|}c_2$. After some modification of the equations and combination of the constants to combined values, the transport equations for the individual species can be reduced to a single equation. However, this treatment makes it impossible to simulate charge separation effects near the boundary, such as double layer formation on the electrode-electrolyte-interface.

The second approach does allow for such separation behavior, the reduction is achieved by expressing the equations in terms of the charge concentration, which is a function of the concentration differences. However, despite allowing for the separation of the concentrations, this method is severly limited by additional requirements, demanding symmetry of the concentration behavior and only small scale changes from the original (identical) concentration function, the so-called linear regime [GT09]. This requirement of symmetric small scale changes to the mean concentration limits the ability to handle changes of the concentration profile over time or non-symmetric boundary conditions.

By design neither of the above methods is able to treat multi species problems with more than two species, but as noted above the limitations reach even further. Often the transport coefficients involved are changed, the relative behavior of the different species becomes the relevant characteristic and as such, at times the transference number of the respective ion species is used instead of the diffusion coefficients [LZ11].

In contrast, our non-reduced equations cannot be solved with knowledge of the transference number alone, but instead they are able to derive it from their simulation results, as we will demonstrate in section 5.5.

4.2.3 Analytical Solutions

Due to the nature of the coupling between the equations, analytical solutions for the general case of the Poisson-Nernst-Planck system have not been found. However, for some special cases, exact solutions to the Poisson-Nernst-Planck system or approximate solutions under limiting requirements can be provided.

Exact Analytical Solution to the Single Species Problem

We note that for the decoupled equations an analytical solution to the Poisson equation can be derived from the combined charge concentration function. This property forms the basis of one of the cases where an exact analytical solution is available, the single species case with Neumann boundary conditions, as in this case the charge concentration function is a multiple of the concentration function of this particular species. Introducing the electric field $E = -\nabla\Phi$, for a single species we have the relation $\nabla \cdot E = z^2\, c_0$. With additional spatial integration to remove the divergence, the

formerly coupled equations (4.18) and (4.12) can be reduced to the single non-linear vector valued equation

$$\frac{\partial E}{\partial t} = \Delta E + E(\nabla \cdot E) + \nabla \times G,$$

where $G(x,t)$ is a gauge field resulting from the integration. In order to obtain a solution for this equation in one dimension, additional transformations are necessary to first reach the Burgers equation and subsequently the heat equation. Boundary conditions need to be transformed likewise and the solution of the heat equation can then be transformed back to the original functions. While this method works well for one dimension, for two and three dimensions additional requirements are necessary, assuming that the dimensions need to behave identical and that the functions in each dimension can be combined by addition [Sch12].

Approximative Solutions

Other analytical approaches do not give exact closed functions, but are based on approximations, often connected with asymptotic expansion. Care must be taken in two regards, first that the requirements which justify the relevant approximations are properly satisfied and second that there is a remaining error, which these approximations still carry. In fact, a priori it is not clear whether the error made by an analytical approximation is an improvement over the error made by a numerical solution, which stems from an approximation by discretization.

The result presented in [GT09] is an example, where the approximation matches the qualitative behavior of the solution very well, but the quantitative results deviate from numerical solutions. The approximation begins by requiring only small voltages for a reduction to a single charge concentration, as described in section 4.2.2, and suffers from the same limitations. Furthermore, the approximation is time dependent, however intermediate steps rely on approximation properties of a stationary solution. As noted before, the resulting approximation models the qualitative behavior of the solution relatively well, while the solution deviates quantitatively. Indeed, when controlling how well the solutions satisfy the original equations, it can be shown, that the analytical estimate produces larger residual values than the numerical results, see section 5.3.3.

Another approximation ansatz [SS15] is targeted towards the steady state only. One of the assumptions made is electroneutrality, which again leads to the limitations considered in section 4.2.2. For a specific one-dimensional problem a closed expression is given, while for a two-dimensional problem the method of asymptotic expansion is used. Comparison with numerical results show a deviation in the single digit percentage regime, which is concentrated on the boundary of the system.

4.2.4 Extension to Thermal Modeling

Up to recently, approaches to thermal modeling ignored the internal coupling to the ion flux modelled by the Poisson-Nernst-Planck system. In [SDB+13] heat generation is computed from the state of charge, current and overpotential, neglecting internal temperature gradients and their resulting influence on the ion flux (and thus again coupling to the heat generation). In other cases, the modeling of heat generation is restricted to cylindric geometries and to chemical reactions in the electrodes [MZRS16].

Even in cases where the models of ion migration were successfully derived from thermodynamics, the actual temperature was assumend as a constant in first implementation works [LZ11]. Following reports on thermal coupling were confined to two dimensions initially [TTP+12] and only recently the same group turned to 3D dynamic temperature simulations, however they point out themselves that some of their approaches may not be valid, since the scale of the electrode particles and the electrode thickness is too similar to separate [LZ15]. While the modeling is very thorough and multiple forms of coupling between temperature, concentrations and electric field are observed, we point out that the transport equations are reduced to binary systems in an electroneutral setting, whereas we permitt arbitrary number of species and charge separation.

4.2.5 Numerical Techniques

In the modeled physical setting the ions behave as sources and sinks of the potential field which drives their convection. In the equation system, this leads to strong non-linear coupling between the Nernst-Planck and the Poisson equations. Explicit approaches to solving this system have been found to immediately fall prey to unstable exchange effects [Neu10], namely oscillating signs in the net-charge of the ions and correspondingly in the gradient of the potential which drives the ions. While such behavior is not explicitly mentioned in other literature, almost all other publications on this topic make use of full implicit methods, e.g. [SM99, LZH+07, CCAO14]. While we found a single mentioning of a pure explicit handling, this was restricted to the context of solving the steady state equations only [ZCW11].

Recent advances [MG14] demonstrate that implicit-explicit methods used in the treatment of the Nernst-Planck equation may be combined with a separated implicit solution of the Poisson equation. However, the discretization requires mixing of Finite Element and Finite Volume methods and parts of the cell interpolation scheme cannot be extended to three dimensions. Several other assumptions are placed on the modeled systems, among which are a limitation of the applied voltage to the so-called thermal voltage[3] and very thin electric double layers, where the Debye layer thickness

[3] The paper gives the formula as $\Delta V \ll \frac{ez}{k_B T}$, but the units are inverted on both sides. The restriction becomes sensible by inverting the fraction $\Delta V \ll \frac{k_B T}{ez} = 0.0258V$.

(estimated for $\varepsilon_r = 80$, $T = 300K$, $z = e$ and $c = 1\frac{mol}{l}$)

$$\lambda = \sqrt{\frac{\varepsilon_0 \varepsilon_r k_B T}{2ce^2 z^2}} \approx 1 \cdot 10^{-8} m$$

must be far smaller than the characteristic length of the simulated region or the width of possibly present pores.

Scharfetter-Gummel Method

Since the PNP equations pose several numerical challenges, the first being the possible dominance of convection over the diffusion in the Nernst-Planck equation, several attempts have been made to overcome them. Transforming the dependent and independent variables is a common approach in this regard and known as a Scharfetter-Gummel discretization [FGJ91, GG92] or also as the introduction of Slotboom variables. Here we will summarize results for the transformation with Slotboom variables as published in [LHMZ10].

The aim of the variable transformation is to change the NP equation, such that the operator becomes uniformly elliptic and self adjoint. To that end Slotboom variables are introduced as follows

$$\bar{D}_i := D_i e^{-\beta q_i \Phi}, \qquad \bar{c}_i := c_i e^{\beta q_i \Phi}. \tag{4.19}$$

The resulting transformed NP equation is indeed self adjoint

$$\frac{\partial \left(\bar{c}_i e^{-\beta q_i \Phi}\right)}{\partial t} = \nabla \cdot \left(\bar{D}_i \nabla \bar{c}\right),$$

however the expectation that the operator's condition would be reduced in the process turned out to be false in several instances, specifically in the context of biomolecular applications. Furthermore, after applying the transformation, the Poisson equation will no longer be self adjoint

$$-\nabla \cdot (\varepsilon \nabla \Phi) - \lambda \sum_i q_i \bar{c}_i e^{\beta q_i \Phi} = 0.$$

As the Poisson-Nernst-Planck equation is extended even further, other problems surface as well, as convection terms introduced by other sources than the Poisson equation (e.g. the chemical potential) cannot be treated with this approach. Possible solutions might come from changing the modeling of the problem by including the additional terms in the solution of the Poisson equation, but this would not solve the mathematical issue for the extended equation system.

4.3 Discretization of the Heat-Poisson-Nernst-Planck System

Before solving our general Heat-Poisson-Nernst-Planck system numerically, we need to establish a discretization of the problem. We will begin this section by a comparison of available discretization methods and their previous applications in related systems. After this review we will present the weak form of the Heat-Poisson-Nernst-Planck equation and transform these equations into the form which we will eventually use in our simulation routine. The non-linear coupling between these equations makes the selection of the time discretization non-trivial. Thus we finish this section by discussing the couplings inside the domain and those which may arise from boundary conditions before presenting the final linear system to be solved and the matrices to be assembled.

4.3.1 Overview of Discretization Methods

Before describing our actual handling of the discretization of the coupled system, we will give an overview over generally available discretization methods and their previous application to this or related systems.

Finite Volumes

The Finite Volume method seems a natural choice to discretize the PNP and related systems, due to its ease of handling unstructured grids and sustentation of conservation properties by construction. Furthermore, Finite Volume methods are easily able to handle discontinuities in the solution function, as they might occur along interfaces of different regions. However, their convergence theory is generally much less developed compared to the long-studied Finite Difference and Finite Element methods. Indeed, this method is only being used quite recently in the PNP setting [MG14, Fuh15] and was found to have limited convergence rates [SSZL16]. In addition, as already mentioned in 4.2.5, an extension of Finite Volume and Finite Element methology in [MG14] is able to handle two-dimensional problems, but does not fully extend to three-dimensional ones. Nevertheless it might be interesting to investigate a full Finite Volume approach in future work in order to check whether their favorable characteristics improve the behavior of Heat-Poisson-Nernst-Planck simulations.

Finite Differences

Finite Differences are a very intuitive method for solving PDE problems and have for some time been the most prominent method in numerical solvers for PDEs [GRS07]. Traditionally, they have been confined to regular grids and domains, significantly limiting their potential. Approaches dealing with irregular domain shapes, such as the

Shortley-Weller method, retain convergence properties, while the order of consistency of the method is reduced [Hac05, GR94].

Irregular grids may be treated with so-called box schemes, which are closely related to Finite Volume techniques and in most cases require dual latices [GR94]. Other approaches, which can be applied to irregular grids – and more generally even to collections of points without grid structure, are known as General Finite Differences (GFD) [LO80] (also as Finite Differences for Arbitrary Grids (FIDAG), Meshless Finite Difference Method (MFDM) and others [Vas15]). However, prior to the solution of the PDE, obtaining a proper discretization require additional problems (such as least squares problems) to be solved and may encounter problems of singular or almost singular subsystems.

Apart from these practical limitations, Finite Difference methods have substantial requirements on the solution function in order to guarantee their convergence results. Classical methods require for the solution function $u \in C^4(\Omega)$ in order to guarantee second order convergence, while we will see in the next section that requirements from the Finite Element method are much more relaxed.

Despite the listed difficulties, there have been previous uses of FD methods for PNP problems [ZCW11], however, even on regular grids, they required the use of adapted stencils and were limited to the steady state.

Finite Element Method

The Finite Element method has replaced the previously discussed Finite Difference method as the most prevalent numerical discretization method for PDE problems [GRS07]. While this popularity may be based on the possibility of easy implementation of the method, extensive convergence and stability results are available and the reduced requirements on the space of solution functions makes them also appealing from a mathematical point of view, if knowledge about the actual solutions is scarce, as in our case.

Additionally, they are flexible with respect to irregular domains and are able to achieve high orders of convergence [SSZL16]. The general setting of Finite Elements allows for a reaction to a variety of numerical challenges by adaptions of the method. Among those are discontinuous Galerkin methods to handle discontinuities along domain interfaces or Petrov-Galerkin upwind methods for the stabilization of convection dominated problems. However, the advantages of using such specialized methods must be weighted against their downsides. In the case of discontinuous Galerkin methods, the continuity may be lost in domains where it is required, and while streamline upwind methods increase the stability of the computation, the order of convergence is reduced at the same time. As a consequence, the standard approach is still viable [LHMZ10] and in combination with prudent grid selection able to solve problems on complex geometries with multiple species and varying boundary conditions.

4.3.2 Weak Form of the Heat-Poisson-Nernst-Planck System

For actually solving the equation system numerically, we intend to discretize the equations by the Finite Element Method in space. As the proper introduction of this method, its derivation and the description of its nuances can easily fill a book on its own and have already been studied extensively, we direct the reader to other works [Sch91, BR03, Bra07]. Instead we will restrict ourselves to applying the weak formulation to equations (4.11) to (4.13).

Since we intend to discretize the Heat-Poisson-Nernst-Planck system in the framework of the Finite Element method, we need to convert the strong form of the differential equations (4.11)-(4.13) to the corresponding variational problem, also referred to as the weak form. Generally, the solutions to the original problem are required to be continuously differentiable, meaning we need to demand that for $\Omega, \Omega_T \subset \mathcal{R}^n$

$$c_i \in C^2(\Omega) \quad \forall i = 0, \dots, n-1, \qquad \Phi \in C^2(\Omega) \qquad \text{and } T \in C^2(\Omega_T).$$

However, these requirements can be relaxed, when we consider the transformed variational equations. From now on let $\Gamma = \partial\Omega$ and $V_c' \subset H^1(\Omega)$, $V_\Phi' \subset H^1(\Omega)$ and $V_T' \subset H^1(\Omega_T)$ be chosen test function spaces. By multiplication with test functions and integration over the spatial domain, we gain the weak formulation

$$\begin{aligned}
\int_\Omega \frac{\partial c_i}{\partial t}\psi d\vec{x} &= \int_\Omega \nabla \cdot \left[D_i \left(\nabla c_i + \frac{z_i F}{RT} c_i \nabla\Phi + \frac{1}{RT} c_i \nabla \mu_i \right) \right] \psi d\vec{x} && \forall \psi \in V_c' \\
0 &= \int_\Omega \left[\Delta\Phi + \frac{F}{\varepsilon} \left(\sum_i z_i c_i + Q \right) \right] \phi d\vec{x} && \forall \phi \in V_\Phi' \\
\int_\Omega \frac{\partial T}{\partial t}\xi d\vec{x} &= \int_\Omega \left[\alpha \Delta T + \beta \right] \xi \, d\vec{x} && \forall \xi \in V_T'
\end{aligned}$$

of our original strong PDE problem (4.11)-(4.13). For ease of readability we will drop writing "$\forall \psi, \phi, \xi \in V_\cdot'$" from now on, however this requirement for the general validity of the equations is still implied.

As is commonly done in such settings we use partial integration to shift part of the spatial derivatives to the test functions and obtain boundary terms

$$\begin{aligned}
\int_\Omega \frac{\partial c_i}{\partial t}\psi \, d\vec{x} &= \int_\Gamma \left[D_i \left(\nabla c_i + \frac{z_i F}{RT} c_i \nabla\Phi + \frac{1}{RT} c_i \nabla \mu_i \right) \right] \cdot \vec{n} \, \psi \, d\vec{x} \\
&\quad - \int_\Omega \left[D_i \left(\nabla c_i + \frac{z_i F}{RT} c_i \nabla\Phi + \frac{1}{RT} c_i \nabla \mu_i \right) \right] \nabla\psi \, d\vec{x} \\
0 &= \int_\Gamma \nabla\Phi \cdot \vec{n} \, \phi \, d\vec{x} - \int_\Omega \nabla\Phi \nabla\phi \, d\vec{x} + \int_\Omega \frac{F}{\varepsilon} \left(\sum_i z_i c_i + Q \right) \phi d\vec{x} \\
\int_\Omega \frac{\partial T}{\partial t}\xi \, d\vec{x} &= \int_\Gamma \alpha \nabla T \cdot \vec{n} \, \xi \, d\vec{x} - \int_\Omega \alpha \nabla T \nabla \xi \, d\vec{x} + \int_\Omega \beta \xi \, d\vec{x}.
\end{aligned} \tag{4.20}$$

From these equations the spatial discretization can be established by choosing basis functions of the test function spaces $V_\cdot'$ and corresponding basis functions for the solution functions. In standard Galerkin methods, the solution functions are developed in the same spaces, with the solutions expressed as

$$c_i(t,x) = \sum_j c_{i,j}(t) \cdot \psi_j(x), \qquad \Phi(x) = \sum_j \Phi_j(t) \cdot \phi_j(x), \qquad T(x) = \sum_j T_j(t) \cdot \xi_j(x).$$

Other choices of basis functions are possible, and methods making use of different basis functions for the test and the solution spaces are referred to as Petrov-Galerkin methods [GR94]. Depending on the choice of the function spaces, different numerical schemes for the integration of the weak forms (4.20) are suitable.

This leaves the discretization of the time dependent coefficients. We establish this via a backwards Euler method, which can also be described as a discontinuous Galerkin discretization with constant test functions [BR03]. It is also known as the method of lines [GR94], leading to

$$\begin{aligned}
\int_\Omega \frac{c_i^{n+1} - c_i^n}{\Delta t} \psi \, d\vec{x} &= \int_\Gamma \left[D_i \left(\nabla c_i^{n+1} + \frac{z_i F}{RT} c_i^{n+1} \nabla \Phi^{n+1} + \frac{1}{RT} c_i^{n+1} \nabla \mu_i \right) \right] \cdot \vec{n} \, \psi \, d\vec{x} \\
&\quad - \int_\Omega \left[D_i \left(\nabla c_i^{n+1} + \frac{z_i F}{RT} c_i^{n+1} \nabla \Phi^{n+1} + \frac{1}{RT} c_i^{n+1} \nabla \mu_i \right) \right] \nabla \psi \, d\vec{x} \\
0 &= \int_\Gamma \nabla \Phi^{n+1} \cdot \vec{n} \, \phi \, d\vec{x} - \int_\Omega \nabla \Phi^{n+1} \nabla \phi \, d\vec{x} + \int_\Omega \frac{F}{\varepsilon} \left(\sum_i z_i c_i^{n+1} + Q \right) \phi \, d\vec{x} \\
\int_\Omega \frac{T^{n+1} - T^n}{\Delta t} \xi \, d\vec{x} &= \int_\Gamma \alpha \nabla T^{n+1} \cdot \vec{n} \, \xi \, d\vec{x} - \int_\Omega \alpha \nabla T^{n+1} \nabla \xi \, d\vec{x} + \int_\Omega \beta \xi \, d\vec{x}
\end{aligned} \tag{4.21}$$

4.3.3 Coupling between the Equations

The nature of coupling between the equations in the full system is quite diverse. While all three types of equations are coupled non-linearly over the full domain, the coupling between the Poisson equation and the Nernst-Planck equations behaves very differently from the coupling of both of these types of equations to the heat equation.

Inside the domain the species concentration and – as a derived property – the charge distribution defined by the Nernst-Planck equation act as the sources and sinks of the electric potential computed by the Poisson equation. In turn the gradient field derived from this potential dominates the convection term of the Nernst-Planck equation.

This coupling is extremely stiff, a fact that will be confirmed by our operator analysis in section 5.3.2. Adding to the challenge is the fact, that the coupling is self-opposing, with the charge concentration inducing a convection term which aims to reduce it.

As noted in section 4.2.5, choosing explicit coupling methods between the Nernst-Planck equation and the Poisson equation leads to numerical instability. The specific nature of the equations allows for alternating signs in the flux and consequently to increasingly oscillating behavior of the solution functions.

In contrast to the above experience, the coupling constants between the PNP equation system and the heat equation are much smaller. Yet even more important is the fact, that the coupling does not permit the reversal of the sign of the flux. Since the temperature is always positive by definition only its magnitude changes while its sign remains positive. Thus the flux of particles in the NP equation never changes its direction based on the coupling with the heat equation.

The reverse coupling is also constant in its sign, but the argument is more complex and relates to the discussion of the consequences of the fluctuation theorem, see our remarks in section 2.2.3. We have described the microscopic process of energy transfer controlled by the electric field in section 3.5 with the conclusion that in the steady state Joule heating will take place. As the ion migration described by the system of equations is a macroscopic process, deviations on the microscale cannot be expected and as a result we can be confident that for physical systems no heat sinks will be present. As such we place our consideration under the requirement

$$\beta(c, \Phi) > 0,$$

fixing the sign of the coupling function as positive.

4.3.4 Boundary Conditions

In this section we discuss the selection and the implementation of the boundary conditions to the three types of differential equations we are handling. We denote the boundary by $\Gamma = \partial\Omega$ and $\Gamma_T = \partial\Omega_T$ and allow the separation of the boundary into disjoint subsets Γ_g and Γ_D, such that $\Gamma_g \cup \Gamma_D = \Gamma$, and respectively $\Gamma_{T,g} \cup \Gamma_{T,D} = \Gamma_T$. Γ_D denotes a boundary part where Dirichlet boundary conditions are applied, whereas Γ_g denotes a boundary part, where Neumann or Robin[4] boundary conditions are applied.

For all three equation types of the system, Dirichlet boundary conditions can principally be applied. Dirichlet boundary conditions are appropriate where the respective parameter is instantly controlled by the conditions outside of the domain and the internal behavior is not expected to have an influence on this value. Such an assumption can be the result of a very large reservoir of the respective quantity which is able to compensate changes instantly with respect to the timescale of the simulation. In terms of implementation, Dirichelet boundary conditions are treated by the standard Finite Element approach by setting the coefficients for the respective functions to the value

[4] This type of boundary conditions is not consistently named in the literature. While the name Robin boundary conditions seems to be the most widely used, the names mixed boundary conditions or general Neumann boundary conditions appear as well.

required to satisfy the boundary condition and solve the remaining system restricted to the interior of the domain. However, some special care must we taken in the case of the Newton-Raphson iteration – which we will introduce in section 4.3.5. As we are updating the solution iteratively, we need to ensure that the boundary conditions are not erroneously summed over several iterations. Thus the Dirichlet function needs to be updated in every iteration step by setting

$$u_{\Gamma_D,i+1} = u_{\Gamma_D} - u_{\Gamma_D,i}.$$

Other boundary conditions – leaving Neumann and Robin type conditions – are generally backed by more elaborate modeling and they shall be discussed in the following. Both types of boundary conditions rely on the fact that during the integration by parts a boundary integral is formed. The expression integrated over can be used to define the boundary behavior of the system. While the boundary integral is always computed over the full boundary Γ, we restrict our discussion to the evaluation of Γ_g, as the degrees of freedom associated with Γ_D are fixed in the course of the discretization.

Boundary Conditions for the Nernst-Planck Equation

For the Nernst-Planck equation, the expression of the integral on the boundary is taken from equation (4.20)

$$\int_{\Gamma_g} \left[D_i \left(\nabla c_i + \frac{z_i F}{RT} c_i \nabla \Phi + \frac{1}{RT} c_i \nabla \mu_i \right) \right] \cdot \vec{n}\, \psi \, d\vec{x}.$$

The expression $\vec{I}_i := D_i \left(\nabla c_i + \frac{z_i F}{RT} c_i \nabla \Phi + \frac{1}{RT} c_i \nabla \mu_i \right)$ is the flux of the ion concentration of species i and allows for the specification of flow conditions on the boundary. As such they are often called natural boundary conditions. In addition to the concentration gradient, it contains the concentration function itself, giving these specifications Robin shape, meaning the function value and gradient value are related in the boundary equation. Thus natural boundary conditions take the form

$$D_i \left(\nabla c_i + \frac{z_i F}{RT} c_i \nabla \Phi + \frac{1}{RT} c_i \nabla \mu_i \right) \cdot \vec{n} = g \qquad \text{for } x \in \Gamma_g$$

with g a corresponding boundary function and $\vec{n}$ the normal vector on the boundary. Due to the inclusion of the $\nabla\Phi$ term in the flux, this boundary condition contains an implicit coupling with the Poisson equation. However, after the substitution, this term disappears from the equation, leaving us with the discrete expression

$$\begin{aligned} \int_\Omega \frac{c_i^{n+1} - c_i^n}{\Delta t} \psi \, d\vec{x} = & \int_{\Gamma_g} g\psi \, d\vec{x} \\ & - \int_\Omega \left[D_i \left(\nabla c_i^{n+1} + \frac{z_i F}{RT} c_i^{n+1} \nabla \Phi^{n+1} + \frac{1}{RT} c_i^{n+1} \nabla \mu_i \right) \right] \nabla \psi \, d\vec{x}. \end{aligned} \tag{4.22}$$

Boundary Conditions for the Poisson Equation

For the Poisson equation the boundary integral is

$$\int_{\Gamma_g} \nabla\Phi \cdot \vec{n}\phi \, d\vec{x}. \tag{4.23}$$

This expression describes the gradient of the potential on the boundary or respectively the electrical field on the boundary. Thus standard Neumann conditions can be set with ease, which specify

$$\nabla\Phi \cdot \vec{n} = g \qquad \text{for } x \in \Gamma_g,$$

fixing the field on the boundary. Robin conditions can be set as well, allowing for an interaction between the value of the field and its gradient, which is important for several physical models of the boundary layer. In their most general form they read

$$a \cdot \Phi + \nabla\Phi \cdot \vec{n} = g \qquad \text{for } x \in \Gamma_g.$$

The substitution in (4.23) is then achieved by a simple subtraction on both sides

$$\nabla\Phi \cdot \vec{n} = g - a \cdot \Phi$$

and we note that by setting $a = 0$ any description for Robin type boundary conditions can be transferred to Neumann boundary conditions. Thus we obtain the discrete equation

$$0 = \int_{\Gamma_g} g\phi \, d\vec{x} - \int_{\Gamma_g} a \cdot \Phi^{n+1} \, \phi \, d\vec{x} - \int_{\Omega} \nabla\Phi^{n+1} \nabla\phi \, d\vec{x} + \int_{\Omega} \frac{F}{\varepsilon} \left(\sum_i z_i c_i^{n+1} + Q \right) \phi \, d\vec{x}. \tag{4.24}$$

Boundary Conditions for the Heat Equation

The boundary integral term of the heat equation is

$$\int_{\Gamma_{T,g}} \alpha \nabla T \cdot \vec{n} \xi \, d\vec{x}.$$

As for the Poisson and the Nernst-Planck equations, the description of the heat equation is not complete, before boundary conditions are defined. Most of what we have written for the above equations remains true for the heat equation. In fact, due to the nature of its coupling with the PNP equation system and our subsequent explicit handling of the heat equation, the boundary treatment will be easier, as the system remains linear and does not require an iterative treatment. As noted above, the substitution of Robin boundary conditions

$$\nabla T \cdot \vec{n} = g - a \cdot T \qquad \text{for } x \in \Gamma_{T,g} \tag{4.25}$$

can be transferred to Neumann boundary conditions by setting $a = 0$. The discrete equation to be solved is thus

$$\int_{\Omega_T} \frac{T^{n+1} - T^n}{\Delta t} \xi \, d\vec{x} = \int_{\Gamma_{T,g}} \alpha g \, \xi \, d\vec{x} - \int_{\Gamma_{T,g}} \alpha a \cdot T^{n+1} \, \xi \, d\vec{x} - \int_{\Omega_T} \alpha \nabla T^{n+1} \nabla \xi \, d\vec{x} + \int_{\Omega_T} \beta \xi \, d\vec{x}. \tag{4.26}$$

4.3.5 Matrix Structure

With the previous considerations, particularly with our discussion about the coupling in section 4.3.3, we are now able to assemble the matrices and vectors, which will be used in the methods to solve the equation system. Due to the fact that the equations do not stand alone but are part of a system, see equations (4.21), it will be insufficient to only assemble the mass and stiffness matrices of the individual equations. Since we established that the coupling between the heat equation and the Poisson-Nernst-Planck system is straightforward in nature, specifically without sign oscillations to be expected, we will treat this coupling explicitly. For each time step, the heat equation will be solved first, on the basis of the parameters from the previous time step and afterwards the other equations will be treated. The Nernst-Planck and the Poisson equations are treated full implicitly due to the non-linear coupling between them and so we are required to combine the terms to a single operator. In the following, when writing the matrix blocks we will use the shorthand $\psi' := \nabla\psi$, $\phi' := \nabla\phi$ and $\xi' := \nabla\xi$ for the test functions. Furthermore, we will combine the individual solutions of the Nernst-Planck equations and the Poisson equation to a vector, using the notation

$$\vec{u} = \begin{pmatrix} c_0 \\ \vdots \\ c_{n-1} \\ \Phi \end{pmatrix}.$$

We begin with the linear system for the heat equation, which we rearrange from equation (4.26)

$$\int_\Omega T^{n+1} \xi \, d\vec{x} + \Delta t \left[\int_\Omega \alpha \nabla T^{n+1} \nabla \xi \, d\vec{x} + \int_{\Gamma_g} \alpha a \cdot T^{n+1} \, \xi \, d\vec{x} \right] = \int_\Omega T^n \xi \, d\vec{x} + \Delta t \left[\int_{\Gamma_g} \alpha g \, \xi \, d\vec{x} + \int_\Omega \beta \xi \, d\vec{x} \right].$$

Being a scalar equation, the block components for the matrices have scalar form

$$\begin{aligned}\mathcal{M}_{T,ij} &:= \int_{\Omega_T} \xi_i \xi_j \, dx \\ \mathcal{K}_{T,ij} &:= \int_{\Omega_T} \xi_i' \alpha \xi_j' \, dx \\ \mathcal{G}_{T,ij} &:= \int_{\Gamma_T} \alpha \xi_i a \xi_j \, dx,\end{aligned}$$

and together with the vectors

$$\begin{aligned}b_j &:= \int_{\Omega_T} \beta \xi_j \, dx \\ k_j &:= \alpha \int_{\Gamma_T} g \xi_j \, dx\end{aligned}$$

we write the linear system

$$\left(\mathcal{M}_T + \delta t \mathcal{K}_T + \delta t \mathcal{G}_T\right) T^{n+1} = \mathcal{M}_T T^n + \delta t \cdot b + \delta t \cdot k,$$

the solution of which is the time update to the temperature equation.

We continue to give the linear system for the iteration method of the Poisson-Nernst-Planck system. In order to make it easier to find the corresponding terms in the equations, we present the following color coded system

$$\begin{aligned}\nabla \left[\left(D_i \nabla c_i + D_i \frac{z_i F}{RT} c_i \nabla \Phi + D_i \frac{1}{RT} c_i \nabla \mu_i \right) \right] &= \frac{\partial c_i}{\partial t} \\ \nabla^2 \Phi + \frac{F}{\varepsilon} \sum_i \left(z_i c_i \right) + \frac{F}{\varepsilon} Q &= 0,\end{aligned}$$

the discrete version of which can be rearranged from equations (4.22) and (4.24)

$$\begin{aligned}\int_\Omega c_i^{n+1} \psi \, d\vec{x} + \Delta t \int_\Omega \left[D_i \nabla c_i^{n+1} + D_i \frac{z_i F}{RT} c_i^{n+1} \nabla \Phi^{n+1} + D_i \frac{1}{RT} c_i^{n+1} \nabla \mu_i \right] \nabla \psi \, d\vec{x} \\ = \int_\Omega c_i^n \psi \, d\vec{x} + \Delta t \int_{\Gamma_g} g \psi \, d\vec{x} \\ \int_\Omega \nabla \Phi^{n+1} \nabla \phi \, d\vec{x} - \int_\Omega \frac{F}{\varepsilon} \left(\sum_i z_i c_i^{n+1} \right) \phi \, d\vec{x} + \int_{\Gamma_g} a \cdot \Phi^{n+1} \, \phi \, d\vec{x} \\ = \int_\Omega \frac{F}{\varepsilon} Q \phi \, d\vec{x} + \int_{\Gamma_g} g \phi \, d\vec{x}.\end{aligned}$$

We define the matrices

$$\mathcal{M}_{ij} \coloneqq \begin{pmatrix} \int_\Omega \psi_i\psi_j\,dx & & 0 & 0 \\ & \ddots & & \vdots \\ 0 & & \int_\Omega \psi_i\psi_j\,dx & 0 \\ 0 & \cdots & 0 & 0 \end{pmatrix}$$

$$\mathcal{K}_{1,ij} \coloneqq \begin{pmatrix} \int_\Omega \psi_i' D_0 \psi_j'\,dx & & 0 & \int_\Omega \psi_i' \frac{D_0 z_0 F}{RT} c_0 \phi_j'\,dx \\ & \ddots & & \vdots \\ 0 & & \int_\Omega \psi_i' D_{n-1}\psi_j'\,dx & \int_\Omega \psi_i' \frac{D_{n-1} z_{n-1} F}{RT} c_{n-1}\phi_j'\,dx \\ \int_\Omega \phi_i(-\frac{F z_0}{\varepsilon})\psi_j\,dx & \cdots & \int_\Omega \phi_i(-\frac{F z_{n-1}}{\varepsilon})\psi_j\,dx & \int_\Omega \phi_i'\cdot\phi_j'\,dx \end{pmatrix}$$

$$\mathcal{K}_{2,ij} \coloneqq \begin{pmatrix} \int_\Omega \psi_i' \frac{D_0}{RT}\nabla\mu_0\psi_j\,dx & & 0 & 0 \\ & \ddots & & \vdots \\ 0 & & \int_\Omega \psi_i' \frac{D_{n-1}}{RT}\nabla\mu_{n-1}\psi_j\,dx & 0 \\ 0 & \cdots & 0 & 0 \end{pmatrix}$$

$$\left(\frac{\partial \mathcal{K}_1}{\partial u}\cdot u\right)_{ij} \coloneqq \begin{pmatrix} \int_\Omega \psi_i' \frac{D_0 z_0 F}{RT} c_0 \phi_j'\,dx & & 0 & 0 \\ & \ddots & & \vdots \\ 0 & & \int_\Omega \psi_i' \frac{D_{n-1} z_{n-1} F}{RT} c_{n-1}\phi_j'\,dx & 0 \\ 0 & \cdots & 0 & 0 \end{pmatrix}$$

$$\mathcal{G}_{ij} \coloneqq \begin{pmatrix} 0 & \cdots & 0 & 0 \\ \vdots & \ddots & \vdots & \vdots \\ 0 & \cdots & 0 & 0 \\ 0 & \cdots & 0 & \int_{\Gamma_g} \phi_i a_\Phi \phi_j\,dx \end{pmatrix},$$

where $\mathcal{M}$ is the mass matrix, $\mathcal{K}_1$ and $\mathcal{K}_2$ are parts of the stiffness matrix and $\mathcal{G}$ takes care of the Robin boundary term for the Poisson equation. $\frac{\partial \mathcal{K}_1}{\partial u}\cdot u$ is an additional matrix, which we will need to complete the non-linear handling of the coupling. Furthermore we set the vector

$$k_j \coloneqq \begin{pmatrix} \int_{\Gamma_g} g_0\psi_j\,dx \\ \vdots \\ \int_{\Gamma_g} g_{n-1}\psi_j\,dx \\ \int_{\Gamma_g} g_\Phi\phi_j\,dx + \int_\Omega \frac{F}{\varepsilon} Q\phi_j\,dx \end{pmatrix},$$

which defines the boundary values and possible background charge.

With performance optimization in mind, we note that not all of these matrices are dependent on iterated values. While the matrix $\mathcal{M}$ and the green colored terms in $\mathcal{K}_1$ are clearly independent of the iterated values, the terms in the matrix $\mathcal{K}_1$ marked in blue are directly dependent. For all other terms the dependency is decided by

the possible dependence of the respective coefficients D_i and μ_i. If these values are constant, an update of the matrix is not necessary within the iteration loop. If these coefficients are concentration dependent, a full implicit method requires them to be updated within each iteration cycle, while ignoring to update them (leaving them at their respective value from the previous time step) would introduce a semi-implicit part into the procedure.

4.4 Numerical Solution

After having assembled the Heat-Poisson-Nernst-Planck system in its discretized form we will handle it numerically. The coupled system poses several challenges, of which we have already discussed the non-linear coupling. Different units and dimensions of the solution functions pose another challenge, as they may distort the balance of approximations introduced by numerical methods. Additionally, depending on input variables and discretization, the absolute values of many parameters will change, most importantly the vector norms when computing the residual in the linear solution. This can be dealt with via nondimensionalization and prudent scaling. Linear solver methods can also be aided by reorganization of the matrices involved. Furthermore, the strong coupling of the equations, as well as previous results, let us expect that the behavior of the solution is not uniform across the domain of the solution functions. As a consequence we will consider adaptive strategies as well as the possibility of previous selections of suitable grid layouts.

4.4.1 Newton Method and Linear Solver

Newton-Raphson Iteration

In order to treat the nonlinearity of the Poisson-Nernst-Planck operator we make use of an iteration method of Newton type. For readers not familiar with this method, we suggest [Sto05] for further descriptions and convergence results.

We define the residual function on which we use the Newton-Raphson method

$$\mathcal{R}(u^{n+1}) := (\mathcal{M} + \delta t \cdot [\mathcal{K}_1 + \mathcal{K}_2 + \mathcal{G}])\, u^{n+1} - \mathcal{M}u^n - k,$$

which evaluates to zero if u^{n+1} is a solution to the discretized version of our Poisson-Nernst-Planck operator.

Considering some approximation u_i^{n+1}, where i denotes the index of an iteration, we wish to find an update δu, such that

$$u_{i+1}^{n+1} := u_i^{n+1} + \delta u \approx u^{n+1}.$$

Since our residual function $\mathcal{R}(u)$ can be Taylor expanded, we expect

$$0 = \mathcal{R}(u^{n+1}) \approx \mathcal{R}(u_i^{n+1}) + \left.\frac{\partial \mathcal{R}}{\partial u}\right|_{u_i^{n+1}} \delta u$$

and inserting this into the Newton-Raphson method gives

$$\begin{aligned} -\mathcal{R}(u_i^{n+1}) &= \mathcal{M}u^n + k - (\mathcal{M} + \delta t \cdot [\mathcal{K}_1 + \mathcal{K}_2 + \mathcal{G}])\, u_i^{n+1} \\ &= \left(\mathcal{M} + \delta t \cdot \left[\mathcal{K}_1 + \mathcal{K}_2 + \left.\frac{\partial \mathcal{K}_1}{\partial u}\right|_{u_i^{n+1}} + \mathcal{G}\right]\right) \delta u_{i+1} \\ &= \left.\frac{\partial \mathcal{R}}{\partial u}\right|_{u_i^{n+1}} \delta u \end{aligned}$$

which defines the linear system to be solved iteratively. In practice it has proven to be beneficial to dampen the iteration update

$$u_{i+1}^{n+1} = u_i^{n+1} + \gamma \cdot \delta u$$

with a dampening factor γ from the interval $[0.75, 0.9]$. Unfortunately, attempts to choose γ via a line-search procedure have decreased performance, as the evaluation of the function $\mathcal{R}(\cdot)$ requires an update of several matrix entries at least in $\mathcal{K}_1$, making multiple evaluations of $\mathcal{R}(\cdot)$ relatively expensive.

Linear Solver

With the system from the Newton method and the linear system from the heat equation, we now need to solve two linear systems. Due to the large size and sparsity of the matrices, direct solvers are impractical and iterative solvers are obvious candidates for this task. Many iteration methods only guarantee convergence for a small class of matrices, e.g. by requiring that the matrix must be symmetric and positive definite, properties which our system matrix does not fulfill.

In these cases, certain Krylow space methods can be used, of which we have chosen to adopt the generalized minimal residual (GMRES) method [SS86][5]. As the name suggests, this algorithm is a variant of the minimal residual algorithm and is specifically geared towards nonsymmetric linear systems. It uses the Arnoldi method for the creation of the basis of the Krylow subspaces it operates on. In order to increase the rate of convergence, we use a preconditioner algorithm computing an incomplete LU decomposition of the sparse matrix before starting the GMRES method. Furthermore, for some simulations large increases in performance were gained by employing a renumbering scheme based on the Cuthill-McKee method [CM69].

4.4.2 Iteration Control and Residual Scaling

As described in section 4.4.1, we make use of an iterative Newton-Raphson method around a linear solver in order to advance our solution in time, with the linear solver

[5] We note that we have also experimented with other solvers and preconditioners, e.g. BICGSTAB or Moore-Penrose Inverse. However, these attempts proved to be either unstable or too computationally expensive.

again being an iterative solver. Thus in both cases we need to define criteria when the iteration has reached sufficient accuracy.

For the final result we are often satisfied with a solution which has a predefined accuracy with respect to the actual solution. For the outer iteration system, the Newton-Raphson solver computes a change δu, which is added to the previous iterated value $u_{i+1} = u_i + \gamma \cdot \delta u$. By its design, the iterative update $\gamma \cdot \delta u$ can be regarded as an approximation to the error $u_i - u$, and thus we can use the respective change to estimate the current accuracy.

However, the absolute value of this norm is only of limited value, as the norm of the residual is dependent on varying factors such as the discretization, the dimension or the scaling of the vector.

The latter should be taken care of by the nondimensionalization procedure from section 4.1.1, leading to solution vectors u, whose values remain of the same order regardless of the specific triangulation. However, the standard vector norms

$$\|u\|_1 = \sum_{j=1}^{N} |u_j|, \qquad \|u\|_2 = \sum_{j=1}^{N} |u_j|^2$$

scale with the number of vector entries N, which depend on the refinement. For one-dimensional problems they scale with $N = \frac{1}{h}$, but for d-dimensional problems they scale with $N = \frac{1}{h^d}$.

Thus we turn to the estimation of the relative accuracy and terminate the outer iteration when the ratio of the norm of the iteration update and the norm of the current solution vector falls under a preset tolerance,

$$\frac{|\gamma \cdot \delta u|}{|u_{i+1}|} < \epsilon_{\text{tol,nonlin}},$$

which corresponds to the relative error which we are willing to accept.

This approach requires that the respective updates are computed accurately. Thus, for the linear system, we use standard methods of error estimation via checking the residual against a predefined absolute tolerance

$$\|Ax - b\| < \epsilon_{\text{tol,lin}}.$$

In an attempt to ensure that the choice of $\epsilon_{\text{tol,lin}}$ is universally suitable, we may select to solve the scaled system $A\hat{x} = \frac{b}{\|b\|}$, where we can obtain the true solution by rescaling $x = \|b\| \cdot \hat{x}$. However, the vector b is not the dominant factor in the residual, moreover the error of the solution x is amplified with the condition of the matrix A, which is constant under scalar scaling.

4.4.3 Adaptivity and Graded Grids

The combination of the numerical treatment presented in the previous sections form a convergent method for solving the full coupled Heat-Poisson-Nernst-Planck system.

We can expect – and will show in the numerical results in section 5.3.4 – standard convergence rates in the respective norms for uniform refinement. However, knowledge from previous research indicates, that the solution to these equations may behave very differently on varying parts of the domain, e.g. exhibiting singularities close to the boundaries or at discontinuities of the coefficient functions. As a consequence, we do not expect the error to be distributed uniformly on the domain, but to be larger in specific subdomains. When these regional errors are dominant, additional refinement in the region with minor errors may have very little effect and the additional ressources spent on the corresponding degrees of freedom are wasted.

The obvious solution to the above problem is to restrict refinement to the subdomains which carry the largest error contribution. However, this obvious solution presents us with the problem to determine on which elements the error is largest. It is apparent that we are not able to derive the exact error for a given discrete solution, as otherwise we would be able to derive the exact solution by combination.

There are several methods of a posteriori error estimation available, which generally follow a heuristic approach transferred from a particular model problem, such as the so-called Kelly error estimator [KGZB83]. While this particular method is fitted to the general Poisson equation, it has been formulated for convection-diffusion equations as well. However, it has the inherent requirement that the derivatives of the numerical solution must be permitted to be discontinuous on the cell boundaries, as the estimator is based on the value of this discontinuity of the derivatives across cells. Even when this condition is satisfied, additional questions remain, such as at which time the estimation provides proper results, as time dependent problems have not been covered. In our previous work [Neu10] we have used such methods with considerable success. However, this success came at significant cost, as we had to solve the problem several times on the coarser grids, in order to achieve the refinement which we used for the actual solution.

Here we want to consider an alternative approach of graded grids. While this approach requires some previous knowledge about the solution behavior, it has the possibility to achieve exponential convergence of the error. Taking inspiration from the Kelly error estimator, which considers the derivatives of solution functions, the Scharfetter-Gummel method, which introduces exponential scaling of the solution function and knowledge about underlying physical systems, we make the assumptions that the strong coupling causes solutions in the interior of the domain to be close to electroneutrality – resulting in reduced strength of the electric field. Boundary conditions may disturb this property, driving the charge distribution apart and creating significant sources or sinks for the Poisson equation, which couple strongly with the Nernst-Planck equation. Correspondingly we want to expend the majority of numerical effort in this part of the domain, which can be achieved by introducing a grading function for the choice of grid points. While approaches, which distribute additional degrees of freedom only towards the boundary while leaving the interior degrees of freedom static, show exponential convergence, they do not converge to the full grid

solution. Thus an improved grading scheme is required, where additional degrees of freedom improve the coverage of the whole domain – with preference twoards the boundary area. We will present the successful application of such a grading in section 5.4.1, where we demonstrate improved convergence rates compared to uniformly refined grids.

5 Numerical Results

In this chapter we will finally bring the theory of the previous chapters into practice.

Starting on the atomistic scale, we will be observing examples of energy transfer from external forces both with and without thermostats and measure their energy transfer. We will find that our derivation of error estimates is represented in the computed values and furthermore determine that for physical applications a previously unexpected challenge rises in the ratio of the inner and external interactions.

On the macroscale, we will consider the pure Poisson-Nernst-Planck (PNP) system and its coupled operator before turning to the extended system with the heat equation. While we will find that the coupling and correspondingly the condition of the system are extremely stiff, we will confirm that the full implicit treatment of the equations provides accurate solutions.

For uniform grid refinements, we will observe standard convergence rates despite the non-linearity of the operator. For suitable problems, these can be improved by graded and adaptive grids.

We present an example derived from industrial application in battery design which allows for a comparison with experimental results and for which we perform a sensitivity analysis of the parameters.

The last example presented is a showcase using three-dimensional non-uniform geometry with varying boundary conditions, non-matching grids and multiple ion species to demonstrate the capabilities of our solver.

5.1 External Energy in Lennard-Jones Fluids

In order to demonstrate the feasibility of the application of external forces in molecular dynamics and the computation of the respective energy, we begin by observing the effects on ensembles with a well-known interaction potential, the Lennard-Jones potential defined by

$$V(r_{ij}) = 4\epsilon \cdot \left[\left(\frac{\sigma}{r_{ij}} \right)^{12} - \left(\frac{\sigma}{r_{ij}} \right)^{6} \right],$$

where r_{ij} is the distance between particles i and j, while ϵ scales the depth and σ the width of the resulting potential well. Ensembles for which the particle interacion is completely described by the above potential are known as Lennard-Jones (LJ) fluids. The widespread use of LJ fluids as benchmark problems in molecular dynamics

simulations stems from the relatively simple interaction of the particles, all of which can be treated individually. Furthermore, despite some situational specific shortcomings, Lennard-Jones potentials with additional charge interaction are applied to complex challenges in material design, among which are electrolytes [RH11, MNS13], but also other applications such as cementitious materials [QKB+14]. In contrast to the Lennard-Jones setting, complex forcefields, which are required for the formation of molecules, lead to additional effects in the ensemble, such as manifestation of dipoles, solution shells, etc. These additional effects however carry the potential to increase distortions in an ensemble or the potential barriers between different states, as we will see in 5.2.2.

The first examples presented will treat pure LJ fluids, which we will combine with the Coulomb potential later. While the potential is generally the same as presented in (4.12), now it does not include charge concentrations but point charges. In all our atomistic simulation experiments we used the inhouse-developed Tremolo-X software [GKZC04], which we modified according to chapter 2 to integrate the external energy contributions and thermostat energies.

5.1.1 Basic Results

The first Lennard-Jones fluid being subjected to external forces will be completely normalized with

$$\sigma = 1, \qquad \epsilon = 1.$$

The particles are separated into two groups of 256 particles each, where the first group carries the color charge[1] $q_1 = 1.0$, while the second carries the color charge $q_2 = -1.0$. In order to assemble the ensemble, the particles are placed randomly inside the domain and afterwards we apply a minimization to the potential energy to avoid accidental placement of particles within the singularity of the potential function. Prior to the actual simulation we also perform an equilibration phase with a Berendsen thermostat at $T = 2.7$. We apply constant external forces of magnitude 1.0 during the time interval $[0, 20]$ and set external influences to zero afterwards.

We find that the energy transfer is almost exactly as predicted, with the initial curve matching the energy transfer of free particles as derived in equation (3.7), see figure 5.1. With increasing velocities and more frequent interactions drag becomes apparent and beginning around time unit 10 we see the initial stages of the shift to the linear phase appear in figure 5.1. As the external forces are removed, the external energy becomes constant.

When plotting the total energy – in this case the sum of the physical energy and the transferred energy – we notice a consistent drift of the energy, see figure 5.2.

[1] We recall the concept of color charges from section 2.2.1 and [BEC93], as they do not interact within the ensemble, but affect the direction of outside forces with $\vec{F}_{ext,i} = q_i \cdot \vec{F}_{ext}$.

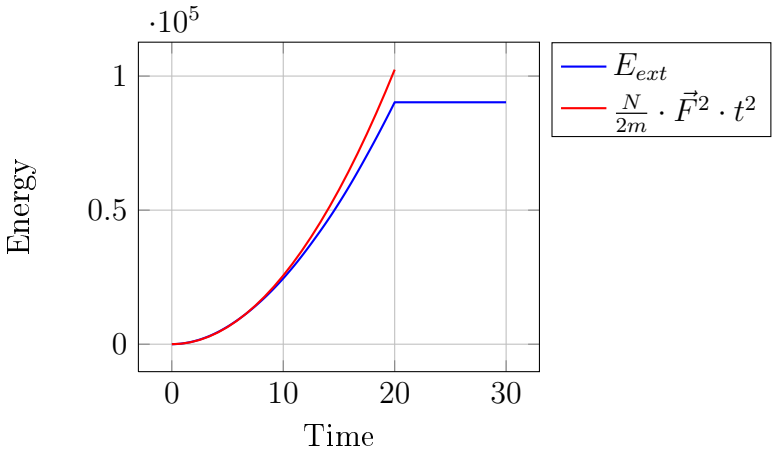

Figure 5.1: Energy transfer from external forces on a Lennard-Jones fluid.

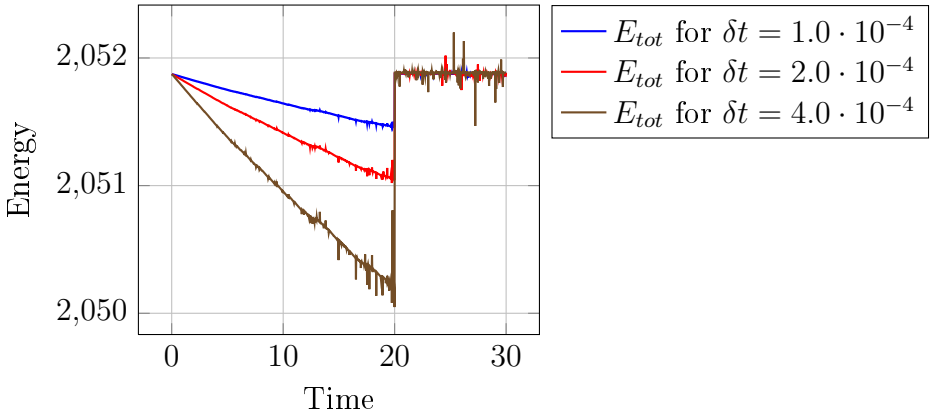

Figure 5.2: Leapfrog shift in total energy conservation in a Lennard-Jones fluid with external forces with varying timestep.

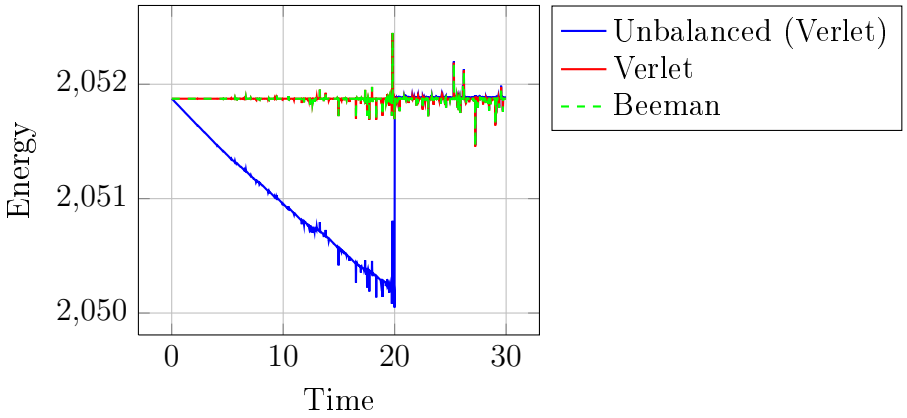

Figure 5.3: Conservation of total energy in a Lennard-Jones fluid in an external field for various iterators with timestep $\delta t = 4 \cdot 10^{-4}$.

This is due to the fact that even though the continuous trajectories of the particles conserve the energy consumed and expended, the discrete trajectories need to satisfy certain conditions to obtain the same property, as we already discussed in section 2.1.5. The energy drift is a consequence of a behavior often associated with leapfrog type algorithms, the physical energy value corresponds to a time removed by half a timestep from the time of the external energy. While the magnitude of this effect can be controlled by refining the size of the timestep, compare figure 5.2, a better approach is to modify the energy measurements or trajectory updates in a way that the time of evaluation coincides. It is indeed possible to construct such a measurement, by splitting the update of the external energy, compare the pseudocode in appendix A. The success of this simple change in procedure is demonstrated in figure 5.3, where we show that the modification removes the energy drift not only for the use of the velocity Störmer-Verlet algorithm, but also for iteration type algorithms, shown at the example of the iterated Beeman integrator.

5.1.2 Demonstration of Unbounded Acceleration

In the previous example, we ended the addition of energy after some time, allowing the ensemble to relax afterwards. In the following example, we will not remove the external forces, in essence providing unlimited energy to the ensemble.

While the energy transferred from external forces displays the same qualitative behavior as before, the plot of the physical energy terminates in a singularity, compare figure 5.4. As the particles achieve higher and higher velocities, the distances they traverse become larger than the interaction radii of the potential. As a result, particles may pass through each other without prior interaction and be placed in effectively random positions in their respective potential fields. Consequently acceleration and repulsion by the particle potentials become random and the energy balance is lost. When this process takes particles close to the singularity of their potential energy function, the extreme forces they are subjected to increase the velocity and the total energy by several orders of magnitude and lead to failure of the numerical scheme as the particles traverse distances surpassing the domain decomposition.

The failure of the simulation may be postponed by enlarging the potential interaction radii and the linked cells or reducing the timestep. However, even if the numerical method would be continually adapted to the growing needs of the ensemble, neither of these measures eliminates the fact that unlimited acceleration of the particles has a physical boundary, as the particle velocities approach the order of lightspeed, introducing relativistic effects. These effects would violate the assumptions formulated in the introduction to chapter 2, thus requiring the transition to different modeling approaches.

When the ensembles and external forces are selected from physical examples however, such extreme cases generally do not need to concern us. Nevertheless, we will investigate a way to keep the energy from external forces in check in simulations with

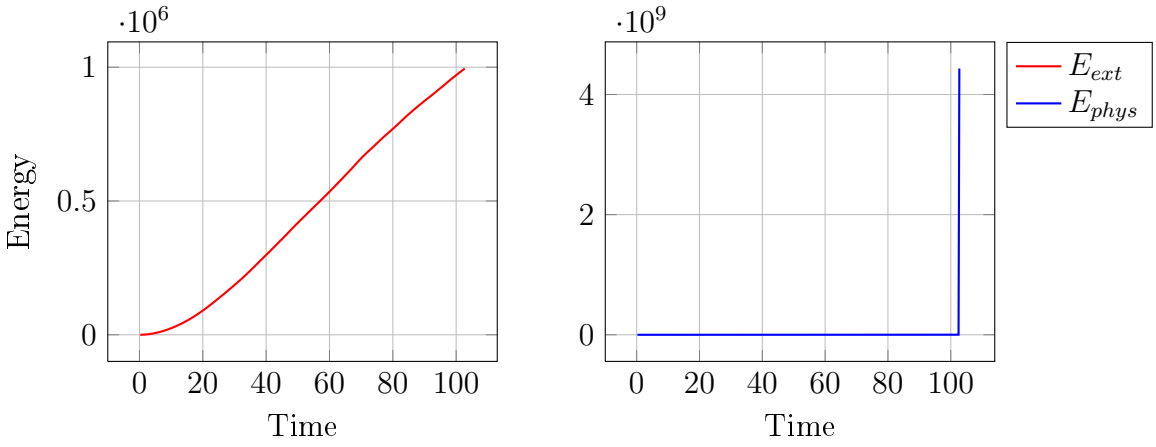

Figure 5.4: Energy transferred externally (left) and physical energy (right) over longer time.

limited domain and particle numbers.

5.1.3 Results with Temperature Control

With the control of external energy additions in mind, we now activate different thermostats with the ensemble to observe their respective behavior in connection with external forces. We will employ two different thermostats, the first being the Berendsen thermostat – introduced in section 3.6.1 – scaling all particle velocities in periodic intervals of 0.2 time units to match a preset temperature of 2.7.

The second thermostat used is the Nosé-Hoover thermostat – introduced in section 2.2.2 – which is assigned a virtual mass of $Q = 0.1$.

While the ongoing energy exchange under the effect of external forces is the main goal of this test case, we nevertheless control how the thermostats react to a removal of the external forces, switching these off after the time interval $[0, 20]$, as we did in section 5.1.1.

Figure 5.5 shows the physical energy of the system, once under the effects of the Berendsen thermostat and once under the effect of the Nosé-Hoover thermostat. As we see, the behavior is quite different for the two thermostats, with the Berendsen thermostat showing oscillations during the time the external forces are applied. The amplitudes of the spikes increase initially, until they appear to be at roughly constant height, as the energy exchange steadies out. As the external forces are switched of, the physical energy appears as a close to constant line. This is in line with the expectations for this type of thermostat, as the corrections of the kinetic energy are applied at discrete intervals only, and between the thermostat steps the transfer of external energy may build up the kinetic energy of the ensemble.

In contrast, the Nosé-Hoover thermostat displays only very small oscillations dur-

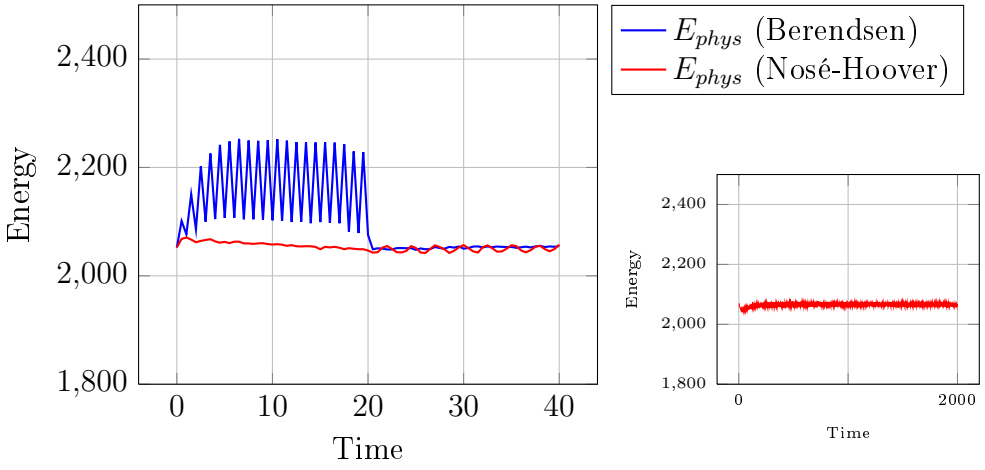

Figure 5.5: Physical energy of a LJ fluid under the effect of external forces and different thermostats.

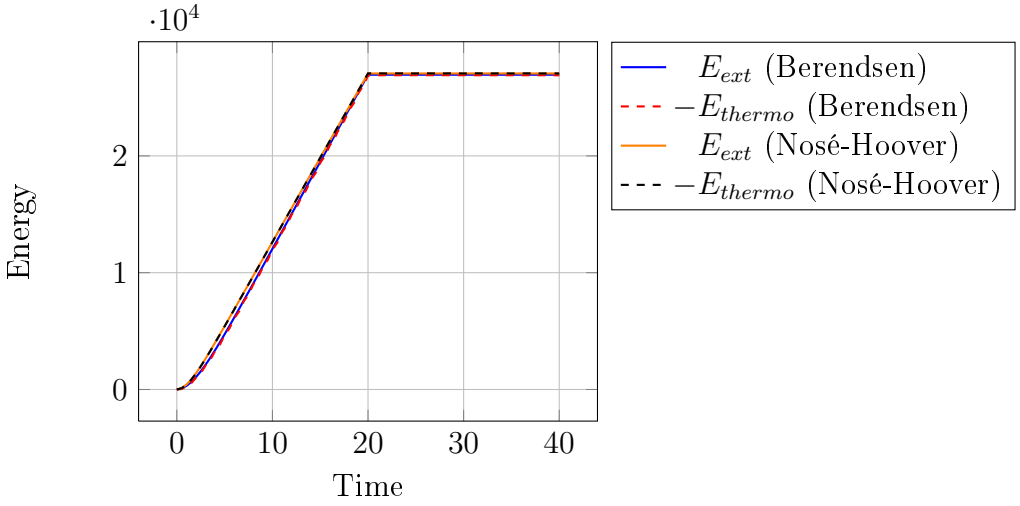

Figure 5.6: Comparison of energy values added by external forces and extracted by thermostats.

ing the heating phase, absorbing the energy more continuously than the Berendsen thermostat. In fact, once the external forces are switched off, the oscillations increase compared to the heating interval. While we have some considerations for the behavior of the frequency of the Nosé-Hoover energy – see [MKT92] – there is no previous experience with oscillation behavior in combination with external forces and thus we controlled the long term behavior to check for delayed changes in the energy. However, despite extending the simulation to 2000 units of time, we found the amplitudes to remain in the same order as those directly after stopping the external forces.

In figure 5.6 we compare the energy transferred to the ensemble from external forces with the energy extracted from the ensemble by thermostats. Since in the previous figure we already learned that the physical energy oscillates around a constant value, the results come as no surprise, in both cases the energy curves lie almost exactly on top of each other, indicating that the energy added and subtracted cancel out.

These results demonstrate that both, the Berendsen and the Nosé-Hoover thermostat can be combined with our new approach to external forces without loosing their original characteristics. In fact the Nosé-Hoover thermostat surpasses expectations with the almost constant energy during the time of heating.

5.1.4 Lennard-Jones Fluids with Neutral Species

In the following numerical experiment the goal is to demonstrate the influence of a denser medium, with which the externally excited particles interact. We start with the ensemble from section 5.1.1, which we modify by the addition of a third species, which is not assigned a charge in the applied color field, but shares the same Lennard-Jones properties as the other two species. Thus we amend the ensemble by adding another 512 particles of a third type. Since the particles may appear anywhere within the current energy landscape, we perform another optimization and equilibration of particle positions as described in section 5.1.1 before starting the simulation.

As laid out in chapter 3, the additional interaction interferes with the acceleration and decreases the final achievable velocity of the particles. As a result the energy transferred from the external forces is significantly decreased compared to the ensemble in free space, as confirmed from the energy transfer presented in figure 5.7. Nevertheless the inital acceleration is still noticeable.

5.1.5 Lennard-Jones Fluids with Coulomb Interaction

When adding Coulomb interaction, the behavior changes again. In the previous examples, the interaction between the particles was only local, requiring the trajectories of the particles to cross. In many physical applications and in particular in electrolytes, electrodynamic interaction is present, which is a long-range interaction, causing particles to exert influence on each others behavior even for non-intersecting trajectories. We start with the ensemble used in the prior experiment and expand the particle

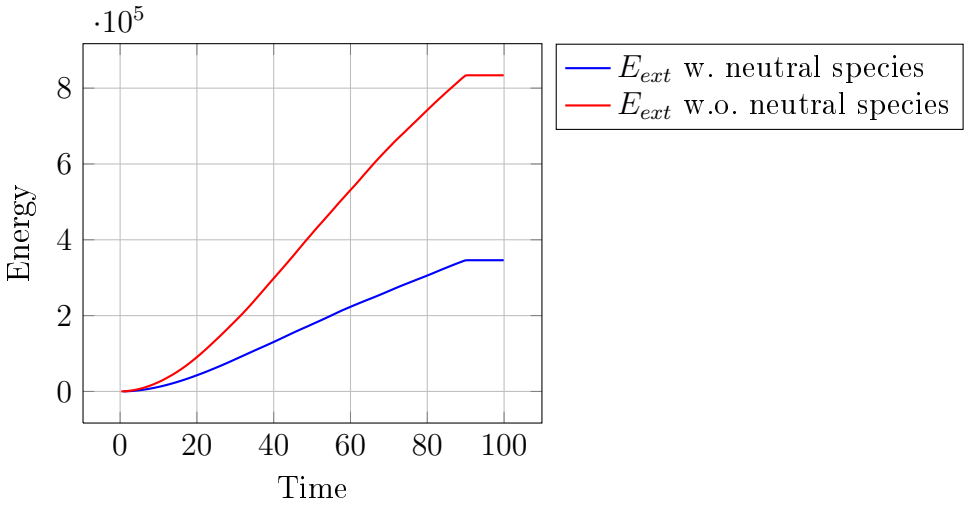

Figure 5.7: Comparison of energy transfer with only color charged particles vs. color charged particles with additional neutral species.

interaction of the charged particles with the Coulomb potential. Since the long-range interaction changes the energy landscape noticeably, another optimization and equilibration of particle positions as described in section 5.1.1 is necessary before we start the simulation.

The Coulomb potential in this scenario is computed by a full N^2 method with a cutoff of 40 units of length, such that the sphere of interaction fits inside the simulation domain.

Following the expected trend, the additional Coulomb interaction causes the rate of energy addition to be reduced, see figure 5.8. However, in addition to changing the quantitative rate, the long-range interaction also causes a delay in achieving a steady state, the quadratic acceleration phase is extended in time.

5.2 External Forces in Electrolytes

In the previous section we observed ensembles with uniform Lennard-Jones parameters and later a simple Coulomb potential, leaving out more complex interactions between the involved species. In this section we will investigate more elaborate settings, modifying the interaction between the particles depending on their species. As our ultimate goal is the simulation of ions in electrolytes, we will first consider an idealized electrolyte in the form of a Lennard-Jones example with varying potential parameters and Coulomb interaction, before turning to physical examples with complex internal force fields. In these sections we will also take a look at the kinetic energy of the simulations, and determine that the more complex settings introduce considerable challenges in forms of distortions of the values to be measured. We will

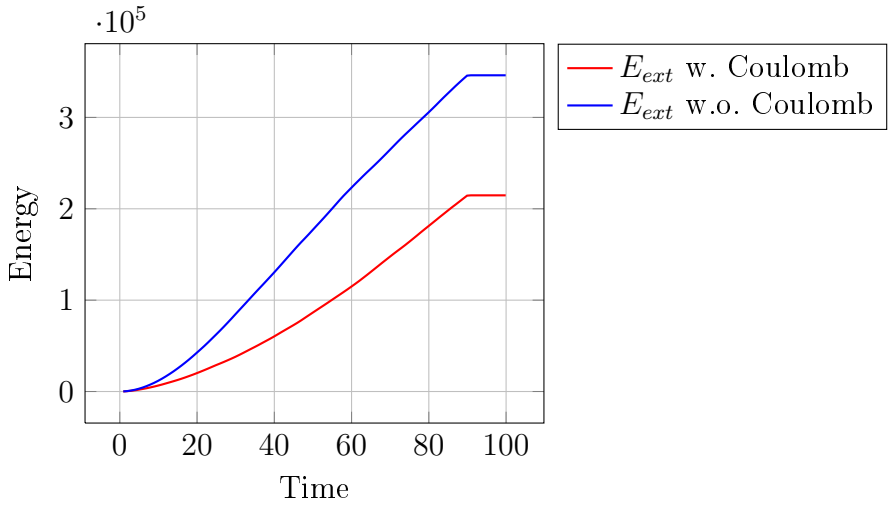

Figure 5.8: Comparison of energy transfer with and without Coulomb potential.

find that these are in line with the predictions of the error estimates from section 3.4.2.

5.2.1 Idealized Electrolyte

Up to now, all particles in the ensemble had identical properties apart from the charge. As a final test of the method, we investigate a composition of particles, where the particle parameters of the group differ from each other. With different masses and potential parameters, the ensemble configuration can indeed be interpreted as a reduced representation of an electrolyte.

We list the chosen parameters by identifying the particle groups via their charge in table 5.1. The resulting energy transfer can be found in figure 5.9. While the transferred energy is further reduced due to the increased mass and stronger interaction of the particles, the qualitative behavior remains unchanged.

In addition to the transferred energy, our interest lies in the behavior of the kinetic energy and temperature of the sample. When comparing the kinetic energy of the ensembles in figure 5.10 we notice that the general behavior of the kinetic energy follows that of the energy transferred from the outside, as can be expected. The scale of the respective energy values matches as well, with a rate of 943.5 energy units per time for the external energy and a rate of 704.2 energy units per time for the kinetic energy. This means, that roughly 75% of the external energy are converted to heat, whereas 25% of the external energy are stored in the potential energy interactions of the particles. However, the characteristic which will have significant influence on the measurability of the heat source is the distortion of the curve. While the curve of the kinetic energy of the ensemble with uniform LJ parameters without Coulomb interaction appears very smooth, the curve of the kinetic energy of the ensemble with varying LJ parameters and with Coulomb interaction shows oscillations

Charge	ϵ	σ	m
1	2	1	1
-1	1.5	1.5	5
0	1	2	10

Table 5.1: Particle parameters for the idealized electrolyte.

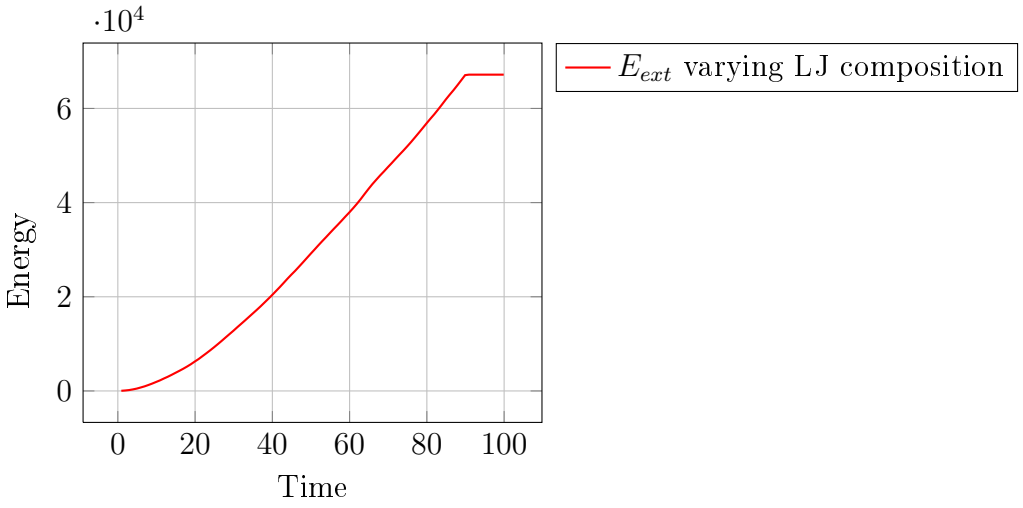

Figure 5.9: Energy transfer with varying LJ parameters and Coulomb potential.

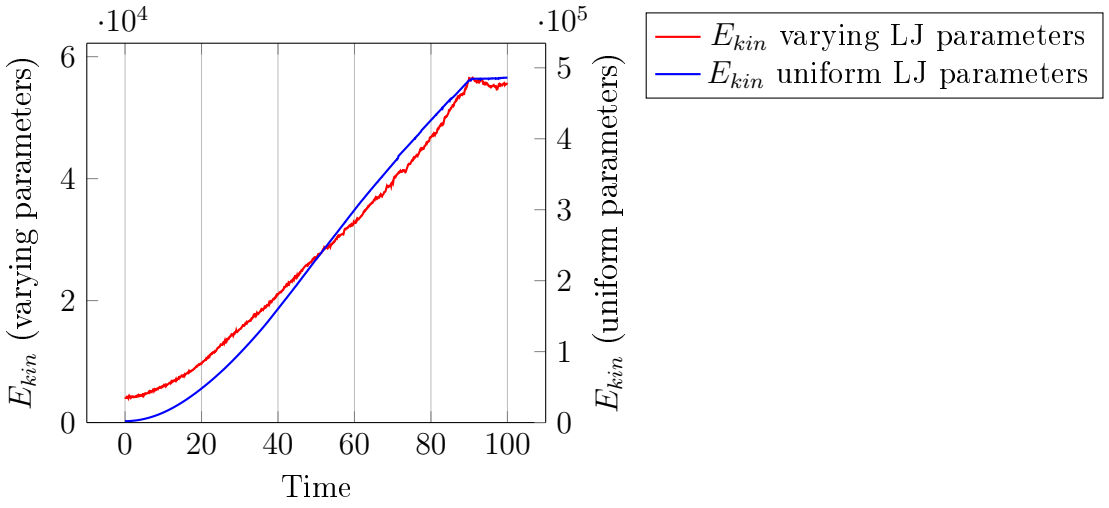

Figure 5.10: Comparison between kinetic energy behavior for pure uniform LJ fluid and idealized electrolyte.

and distortions. These are a consequence of the extended and now in parts unequal interactions of the particles. As the interactions become more complex and the number of different particles increases, we expect such distortions in the kinetic energy to increase, a fact which we will investigate in the following section by considering a real world example.

5.2.2 Complex Physical Electrolyte

In contrast to the above setting, real world electrolytes consist of molecules which have internal physical degrees of freedom and may exhibit different intermolecular interaction depending on their orientation in space. In particular, for many electrolytes the dipole characteristic of the molecules has a strong influence on the dielectric properties of the material.

As an example we present the simulation of an ethylene carbonate (EC) solution. The setup consists of 2177 molecules of ethylene carbonate, see figure 5.11, in a simulation domain of $(61.46744\text{Å})^3$. In this solvent, we embed 10 pairs of Li^+ and BF_4^- ions, resulting in a total of 21830 particles. For the modeling of the intramolecular interactions of the organic EC molecule we turn to the AMBER field parameters [CCB+95], while for the inorganic fluoroborate we use a united atom force field from [LWW06]. Intermolecular forces are modeled by the Lennard-Jones and Coulomb potentials taken from [SMM98, LWW06], the parameters of which we present in table 5.2.

Prior to the simulation we equilibrate the ensemble for $0.061\,ns$ – corresponding to 250000 integration steps under application of a Nosé-Hoover thermostat with a target temperature of $323\,K$. The simulation time is $0.12\,ns$ with a timestep of $0.244\,fs$. All simulations are based on the same equilibrated ensemble and differ only in the applied external forces. We apply external forces[2] of

$$z \cdot 2.304 \cdot 10^{-k} \frac{kcal}{\text{Å} \cdot mol} = z \cdot 2 \cdot 10^{4-k} \frac{eV}{20\mu m} = z \cdot 1.6 \cdot 10^{-10-k} N,$$

with $k \in \{0, 1, 2, 3, 4\}$ and z the particle charge. For the sake of brevity, in the following discussion we will refer to the forces by their base magnitude $2.304 \cdot 10^{-k} \frac{kcal}{\text{Å} \cdot mol}$ dropping the charge variable.

Our goal is to obtain a rate of growth of thermal energy, and thus we observe the behavior of the kinetic energy over time in figure 5.12. For the lower external forces the kinetic energy does not display a discernible trend but is dominated by oscillations, while we observe a trend dominating clearly over the oscillations for the strongest external force.

Compared to the previous examples the observed behavior is quite different, which can be attributed to two – partially correlated – reasons. While previously the internal

[2] Values of external forces in a battery cell can be expected to be around $2\frac{eV}{20\mu m} = 2.304 \cdot 10^{-4} \frac{kcal}{\text{Å} \cdot mol}$.

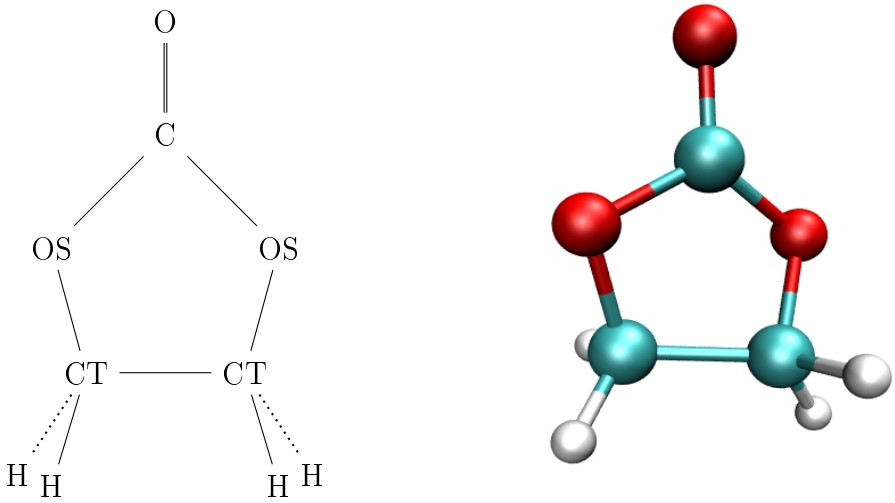

Figure 5.11: Structure of ethylene carbonate; schematics with atom type labels as used by the AMBER force field tables in [CCB+95] (left), simulation snapshot in ground state (right).

Atom type	ϵ $\left[\frac{kcal}{mol}\right]$	σ [Å]	Mass $[u]$	Charge $[e]$
O	0.210	2.96	15.9994	−0.6452
OS	0.170	3.00	15.9994	−0.4684
C	0.105	3.75	12.0107	1.0996
CT	0.066	3.50	12.0107	0.0330
H	0.030	2.50	1.0079	0.1041
Li	0.191	1.46	6.9410	1.0000
B	0.095	3.58	10.8110	0.9756
F	0.068	3.00	18.9984	−0.4939

Table 5.2: Potential parameters of Lennard-Jones and Coulomb interaction for $LiBF_4$ in EC.

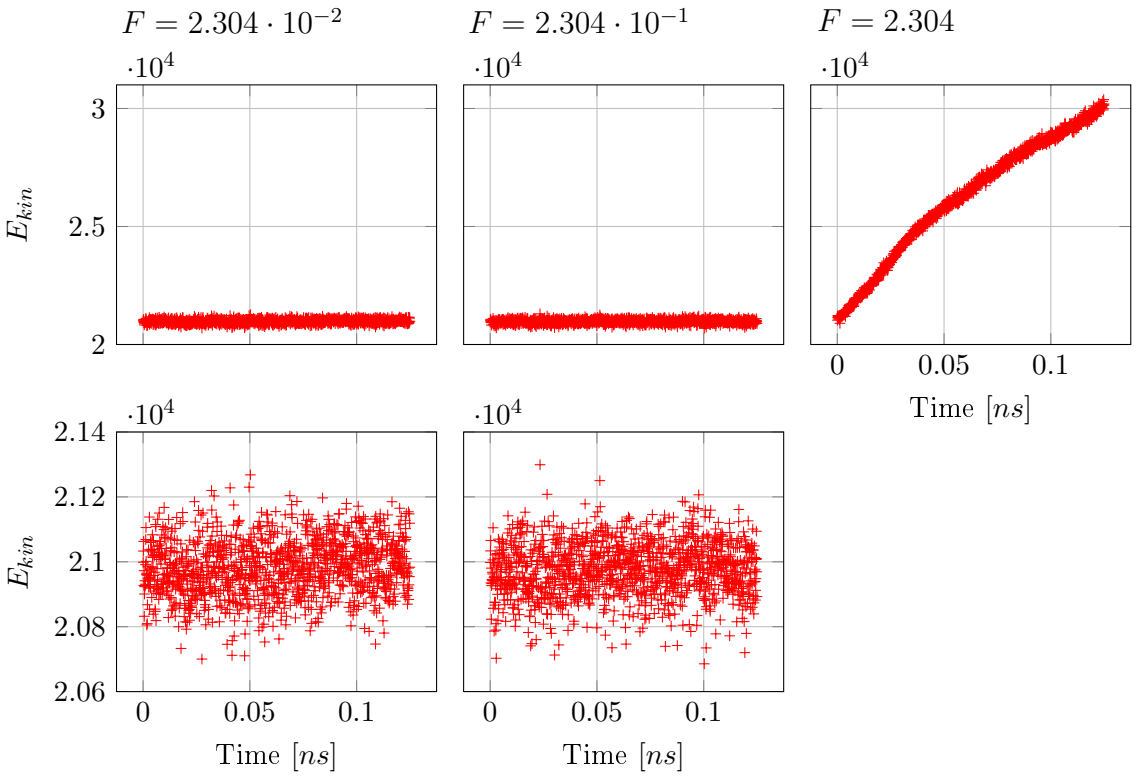

Figure 5.12: Heat generation in ethylene carbonate. Forces are given in $\frac{kcal}{mol \cdot \text{Å}}$.

and external forces were of the same order, this is not the case for either example but the one with the highest external forces. The order of magnitude of internal forces can be expected to be on the order of $\sim 1 \cdot 10^{-9} N$ for covalent bonds [GBR+99] and on the order of $\sim 1 \cdot 10^{-10} N$ for non-covalent bonds [MFG94]. The covalent bonds determine the behavior of its internal degrees of freedom, while the non-covalent bonds determine the interaction of the molecules among each other and as a result their motion. The force of the non-covalent bond interferes with the external forces of magnitude $1.6 \cdot 10^{-10-k} N$ with $k \in \{0, 1, 2, 3, 4\}$, meaning that for the strongest external forces they are on the same order as the non-covalent ones, while for the other settings they are one to four orders of magnitude lower, respectively. For the largest force the dynamics of the particles are changed significantly, as evidenced by the energy transfer on the one hand and increased diffusion coefficients for all particle types on the other[3].

As a consequence, the internal energy fluctuations are several orders of magnitude higher than the energy transferred from the outside, compare figure 5.13. Thus any

[3] Note that the total diffusion coefficient is significantly increased despite the fact that the convection corrected function was used, indicating that the external forces lead to a disturbance in the regular electrolyte dynamics.

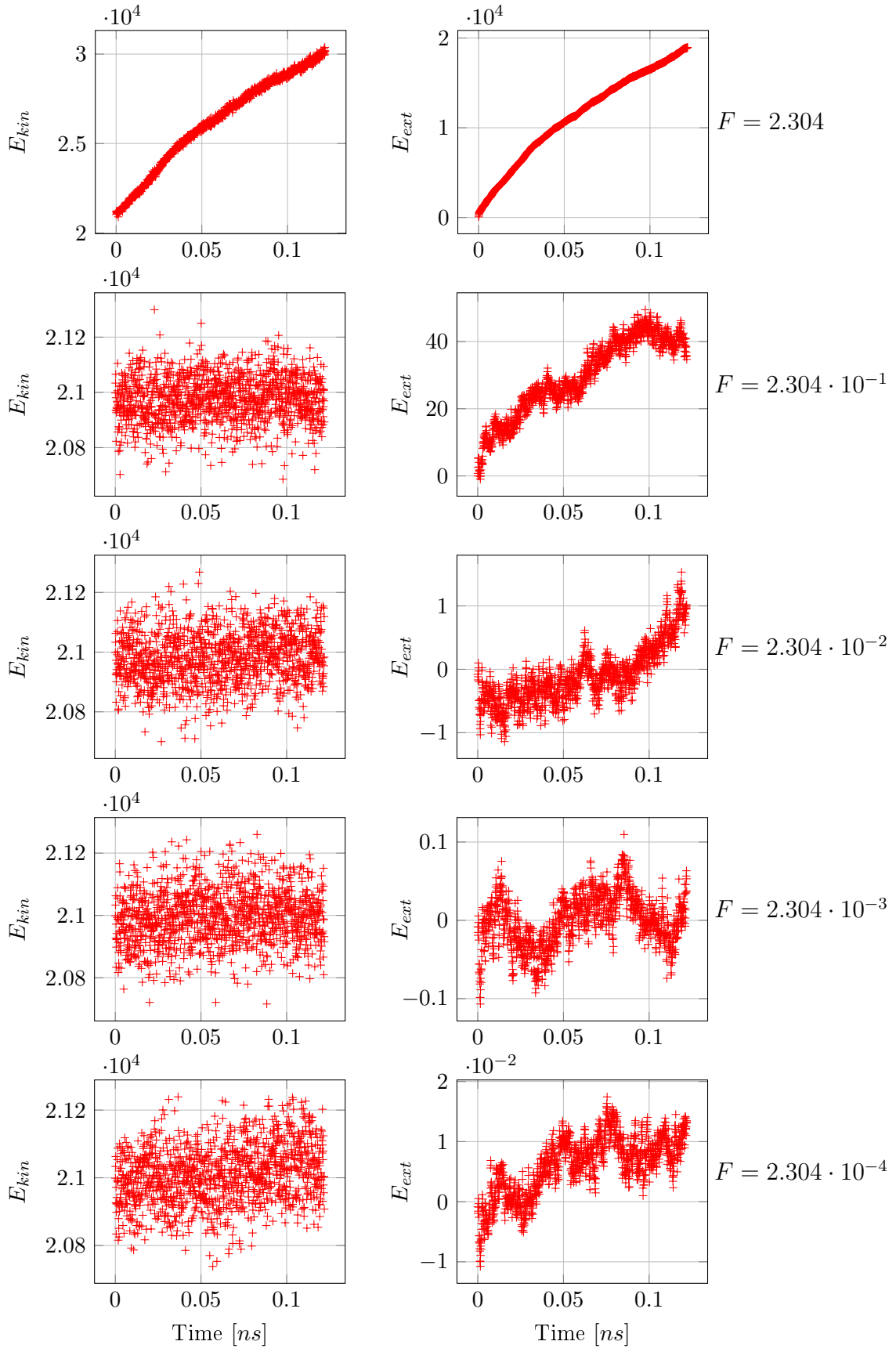

Figure 5.13: Comparison of oscillations in kinetic energy (left) with contributions and oscillations in external energy (right) for an external force of $2.304 \frac{kcal}{mol \cdot Å}$ (top) down to $2.304 \cdot 10^{-4} \frac{kcal}{mol \cdot Å}$ (bottom).

$LiBF_4$ in EC				
Force $\left[\frac{kcal}{mol \cdot Å}\right]$	Rate of heat generation $\left[\frac{J}{s}\right]$	$\left[\frac{K}{s}\right]$	Expected error in E_{ext} rate $\left[\frac{J}{s}\right]$	$\left[\frac{K}{s}\right]$
$2.304 \cdot 10^{0}$	$5.029 \cdot 10^{-7}$	$1.112 \cdot 10^{12}$	$2.9 \cdot 10^{-6}$	$6.4 \cdot 10^{12}$
$2.304 \cdot 10^{-1}$	$1.165 \cdot 10^{-9}$	$2.577 \cdot 10^{9}$	$1.1 \cdot 10^{-6}$	$2.4 \cdot 10^{12}$
$2.304 \cdot 10^{-2}$	$2.015 \cdot 10^{-9}$	$4.456 \cdot 10^{9}$	$1.1 \cdot 10^{-7}$	$2.4 \cdot 10^{11}$
$2.304 \cdot 10^{-3}$	$2.321 \cdot 10^{-9}$	$5.128 \cdot 10^{9}$	$1.1 \cdot 10^{-8}$	$2.4 \cdot 10^{10}$
$2.304 \cdot 10^{-4}$	$4.018 \cdot 10^{-9}$	$8.878 \cdot 10^{9}$	$1.1 \cdot 10^{-9}$	$2.4 \cdot 10^{9}$

Table 5.3: Rates of heat generation in realistic application of $LiBF_4$ in EC electrolyte with estimation of error.

effect of the external forces on the kinetic energy is superimposed and masked by the natural energy fluctuations between the potential and kinetic energy. Apart from masking the energy exchange, the oscillations have the additional effect of influencing the energy contributions from external forces, as the particle velocities are subjected to a random distortion. The effect is evidenced in the lower images of figure 5.13, where the external energies assume negative values and also show oscillations which can not be regarded as converged. The fact that – with exception of the example with the largest forces – the estimated rate of the kinetic energy actually increases as the forces decrease shows that the total kinetic energy and the external forces are in a detached energy state. Nevertheless, we present the results for the ensembles with different forces in table 5.3.

While we can compute the expected error for the external energy with formula (3.10), the detachment of the kinetic and external energies makes the formulas mute for estimating the accuracy of the heat generation. They can however still be used to judge the accuracy of the external energy contribution rates. Estimating the rate of external energy addition for the lowest force, we obtain an energy rate of $6.85 \cdot 10^{-13} \frac{J}{s}$, which on the one hand is much larger than we would anticipate but on the other still several orders of magnitude below the estimated error rates. From general practical and also experimental experience we expect the rate of temperature generation to be on the order of $1 \frac{K}{min}$ [MAHS+99], however heat may also be dissipated to the surroundings. Computing the theoretical upscaling via the Einstein-Smoluchowski equation yields an expected rate on the order of $1 \frac{K}{s}$. Energy and heat dissipation into the surrounding material and by radiation is however not considered in this factor.

A factor not quantified in this thesis is the internal shift between potential and kinetic energy, which disturbes the measurement as well. Methods for quantification and smoothing of this effect would at the very least allow for a better understanding of the restrictions of this method, if not improving the measurement itself. It is known that the convergence of the kinetic energy is hard to achieve, even using thermostats,

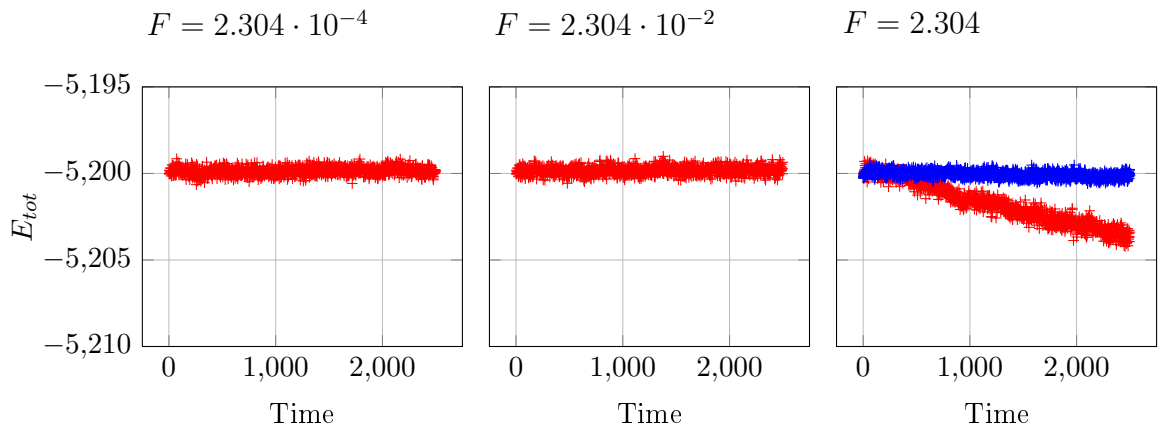

Figure 5.14: Energy conservation for external forces in ethylene carbonate. In the rightmost plot for external forces $F = 2.304 \frac{kcal}{mol \cdot Å}$, we show the total energy computed with $\delta t = 0.244\, fs$ and $\delta t = 0.049\, fs$.

see [BL07]. As we have seen from the previous simulations, the results for simplified interactions were not subject to such distortions. This suggests reduced models e.g. based on mean field and fluid density approximations may be a possible solution to this challenge. Previous work on upscaling results via mean field approaches produced excellent agreement with static properties such as the radial distribution functions, but unfortunately made no prediction about dynamic properties [Jag07].

However, the application of the method as it is to ions in solid materials promises to be an ideal utilization. Since the solid state material would only exhibit small, oscillating movement, the interference with the energy transfer would be restricted. The oscillatory movement also correlates to small diffusion coefficients, reducing the error estimates. Additionally, the energy transfer itself would be concentrated on the embedded ions and consequently be much easier to compute.

As a final remark we note that the external energy is conserved within the numerical accuracy by the four computations with the lower external forces, even using the leapfrog implementation of the external energy evaluation, see figure 5.14. For the simulation with the largest external force we do notice an energy drift, the magnitude of which is below 1‰ of the kinetic energy fluctuations. By refining the timestep, the energy drift is reduced to an order where the trend disappears compared to the oscillations of the total energy value.

5.3 Simulation of the Pure Poisson-Nernst-Planck System

While the theoretical results of this thesis give us some insight into the structure of the numerical system, they nevertheless fail to describe the structure of the solution space. The existence and uniqueness of the solution is only established under restrictive conditions on parts of the equation system and, as we presented in 4.2.1, even without the coupling of all equations there are conditions known, under which the results may follow multiple paths.

With these facts in mind, it is necessary to test the numerical scheme thoroughly in order to guarantee its suitability for the purpose of solving our system of equations. Furthermore, these tests carry further importance beyond the verification of the theoretical method, as they are a verification for the accuracy of its implementation.

In this section we will deal exclusively with the Poisson-Nernst-Planck system – that is with equations 4.11 and 4.12 – while we turn to the full system coupled with the heat equation in the next section. Before presenting numerical experiments, we will deal with analytical questions originally raised in chapter 4, selecting the break criteria for the iteration methods and analyzing the condition of the linear system depending on the coupling constants. We begin the numerical experiments with the comparison of our numerical solutions with analytical approximations, before presenting convergence results for the restricted system and demonstrate the suitability of our solver for multiple ionic species and boundary conditions.

The solver used in the remainder of this chapter is self-implemented based on the description of the numerical system in chapter 4. The software makes use of the Finite Element library deal.II [BR03, BHK07], which provides functions to ease several challenges of the implementation of the numerical system, such as the management of grid elements, degrees of freedom and integration methods.

5.3.1 Selecting the Break Criteria

As noted in section 4.4.2, we control the solver routines by observing the residuals of the respective equation systems. However, in order to choose and validate the values of the break criteria, we apply the iteration procedures to constructed solutions. These solutions are constructed as follows. After running a single simulation, we isolate an arbitrary solution fragment u^{n+1}, which is the approximate solution to the system

$$\begin{aligned} & 0 = \mathcal{R}(u^{n+1}) \\ \Leftrightarrow \quad & 0 = (\mathcal{M} + \delta t \cdot [\mathcal{K}_1 + \mathcal{K}_2 + \mathcal{G}])\, u^{n+1} - \mathcal{M}u^n - k \\ \Leftrightarrow \quad & \mathcal{M}u^n = (\mathcal{M} + \delta t \cdot [\mathcal{K}_1 + \mathcal{K}_2 + \mathcal{G}])\, u^{n+1} - k \end{aligned}$$

and the exact solution to some

$$\mathcal{M}\tilde{u}^n = (\mathcal{M} + \delta t \cdot [\mathcal{K}_1 + \mathcal{K}_2 + \mathcal{G}])\, u^{n+1} - k$$

Error norm	$\frac{\|c-\tilde{c}\|}{\|c\|}$	$\frac{\|\Phi-\tilde{\Phi}\|}{\|\Phi\|}$
L_1	$1.77253 \cdot 10^{-14}$	$5.79862 \cdot 10^{-13}$
L_2	$2.69152 \cdot 10^{-14}$	$5.45608 \cdot 10^{-13}$
L_∞	$1.73692 \cdot 10^{-13}$	$3.90831 \cdot 10^{-13}$
H_1	$1.79493 \cdot 10^{-12}$	$1.27629 \cdot 10^{-13}$

Table 5.4: Relative accuracy of iterated solutions $\tilde{c}$ and $\tilde{\Phi}$ compared to the preset solutions c and Φ.

for the correct $\tilde{u}^n$. Thus we solve the above equation for $\tilde{u}^n$ and treat this vector as the initial condition/previous timestep of our iteration procedure in order to obtain a new $\tilde{u}^{n+1}$, which we compare against u^{n+1} as the known solution.

A selection of

$$\epsilon_{\text{tol,lin}} = 1 \cdot 10^{-16} \text{ and } \epsilon_{\text{tol,nonlin}} = 1 \cdot 10^{-10}$$

has proven suitable, bringing the relative error of the iterative solutions to the constructed solutions to those presented in table 5.4, which we deem suitable even for the possible iteration over multiple timesteps.

5.3.2 Condition of the Linear System

A significant portion of the work of solving our PDE system lies in solving the linear system. The numerical difficulties of this operation can be assessed by the so-called condition number of the corresponding matrix. The condition of the linear system may vary greatly with the parameters used. In particular, the coupling between equations (4.11) and (4.12) plays a significant role.

It is generally not feasible to compute the condition number for every such problem, as the process itself is operation-intensive and thus time-consuming. However, we will investigate several of the PNP systems as they can be classified from the coefficients presented in equations (4.15) and (4.16).

Condition numbers can be defined for any function $f : \mathbb{R}^n \to \mathbb{R}^m$, compare [DH93]. However, we will restrict ourselves to the problem of solving the linear system $Ax = b$. The condition number of a matrix can naively be understood as an indication of how "close" the matrix is to being singular, with singular matrices having infinite condition.

The condition number of a linear system is always given with respect to a particular norm

$$\kappa(A) \coloneqq \|A\| \cdot \|A^{-1}\|.$$

This definition has the problem, that it requires the knowledge of the inverse of A, which, if we had access to it, would render it moot to compute the condition as we could solve our linear system exactly.

Luckily, there are equivalent possibilities to compute the condition number, which depend on the norm and may depend on some matrix properties. The ratio of the largest and smallest eigenvalue

$$\kappa = \left| \frac{\lambda_{max}}{\lambda_{min}} \right|$$

can be used to compute the condition with respect to the Frobenius norm in the case of normal matrices. Unfortunately, the matrix for the coupled PNP system is not generally normal, requiring us to follow a different approach.

For general matrices the condition can be computed with respect to the l_2 norm by the quotient of its largest and smallest singular value

$$\kappa = \frac{\sigma_{max}}{\sigma_{min}},$$

which is the definition we will apply[4].

We recall the dedimensionalized equations of the PNP system from (4.17)

$$\begin{aligned} \tilde{\nabla}\lambda(\tilde{\nabla}\tilde{c}_i + \kappa z_i \tilde{c}_i \nabla\tilde{\Phi} + \pi\tilde{c}_i) &= \frac{d\tilde{c}_i}{d\tilde{t}} \\ \sigma \sum_i z_i \hat{c}_i \tilde{c}_i &= \tilde{\Delta}\tilde{\Phi}. \end{aligned}$$

We propose, that the difficulty of solving this system is largely determined by the parameters λ and σ. Since the solution of the system requires multiple iterations, each with a separate matrix, we take the average of the condition number over all iterations in the first timestep. Since the theory for the Poisson-Nernst-Planck equation system suggests different behavior for one and higher dimensional problems, we executed the same test, once for a one-dimensional problem and once for a two-dimensional. To close the equations we apply uniform Dirichlet boundary conditions of 1.0 for the Nernst-Planck equations and 0.0 for the Poisson equation. The results of these computations are displayed in figure 5.15.

The results are very similar, with slight variations in the quantitative values of the condition numbers, but qualitative identical dependence on the coupling constants. For the one-dimensional case a plateau of condition numbers on the order of 10^3 is roughly encased in the rectangle $10^{-2} > \lambda > 10^{-15}$ and $10 > \sigma > 10^{-15}$, a reasonable condition for handling the solution of linear systems. However, around this area, the condition numbers quickly increase, until they reach the order of 10^{17} for larger values of λ and σ. For the two-dimensional case the area of the rectangle changes only slighly to $10^{-2} > \lambda > 10^{-15}$ and $10^2 > \sigma > 10^{-15}$, however the condition in this area is on the order of 10^4. Similarly the condition numbers outside the area increase up to the

[4] Note that absolute values are not required here, since singular values are positive by definition [BSMM01].

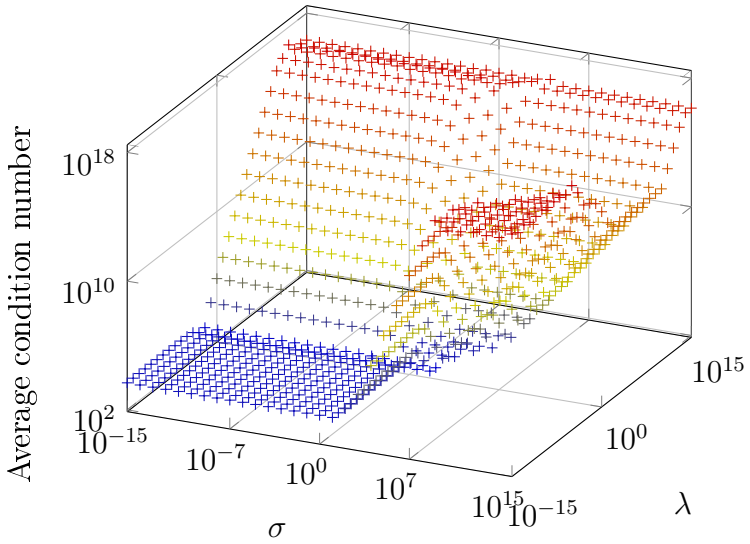

(a) Condition numbers for 1d case.

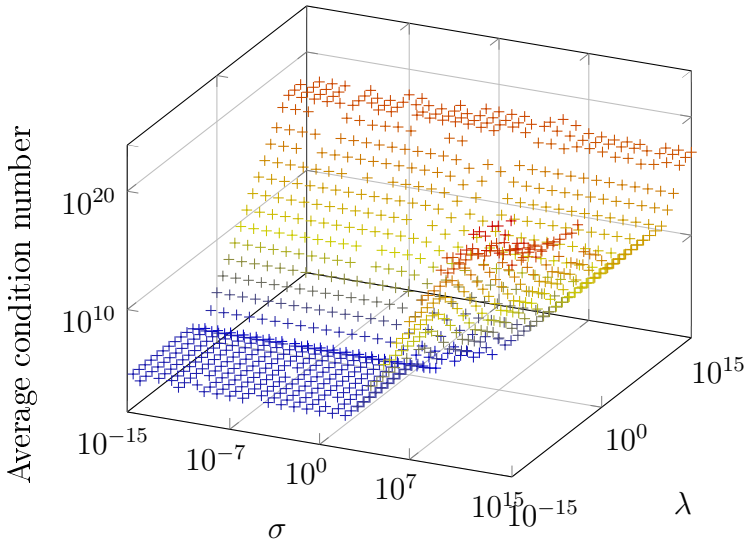

(b) Condition numbers for 2d case.

Figure 5.15: Average condition numbers in dependence on coupling parameters.

order of 10^{22}. For these large condition numbers, the matrices can said to be very close to singularity, making numerical operations with these matrices – like solving linear systems and also the computation of singular values themselves – extremely unstable.

It is possibly that this property leads to some failures in the computation of the condition numbers. While for the one-dimensional case all computations were successfull, in the two-dimensional case 43 out of the 961 computations failed, as can be seen from missing values in figure 5.15.

Note that the magnitude of these values roughly coincides with the results presented in [LHMZ10], where the condition numbers for the Poisson-Nernst-Planck problem applied to a biomolecular diffusion-reaction process were investigated.

In the context of the generally high condition numbers it is of interest, in which region typical physical problems are located. Considering ion migration in a battery as a typical physical example, we can use the following parameters

$$\begin{aligned} D &\approx 2 \cdot 10^{-10}\ \tfrac{m^2}{s} \\ L &\approx 0.5\ mm \\ \tau &\approx 1\ s \\ F &\approx 96485.341\ \tfrac{As}{mol} \\ \varepsilon &\approx 7.0833503 \cdot 10^{-10}\ \tfrac{A^2 s^4}{kg\, m^3} \\ \bar{\Phi} &\approx 1\ V \\ \bar{c} &\approx 1\ \tfrac{mol}{l} \end{aligned}$$

to estimate λ and σ

$$\lambda = \frac{D\,\tau}{L^2} \approx 0.0008, \qquad \sigma = \frac{L^2 F}{\varepsilon \bar{\Phi}} \bar{c} \approx 3.4053569 \cdot 10^{10}.$$

These values place the condition at approximately 10^{11} in the one-dimensional case and 10^{15} in the two-dimensional case, which are both very large conditions. This confirms our previous assumptions on the stiff coupling between the two equations and justifies the full implicit treatment of the Poisson-Nernst-Planck system. At the same time the large condition numbers serve as a warning that small residuals in the numerical solver may be connected to large errors in the solution vector [SK91].

5.3.3 Comparison with Analytic Approximations

As noted in section 4.2.3, analytical approximations to the solutions rely on restrictive assumptions to the equation parameters. However, even within these restrictions the analytical expression does not solve the equations exactly, but produces a residual. In this section we will compare the numerical solutions from our solver with the analytical approximation to a problem presented in [GT09].

The model problem has the properties

$$\begin{aligned} c_0 \coloneqq c_i(x,0) &= 6.022142e19\tfrac{1}{mol}, \\ D &= 1 \cdot 10^{-16}\tfrac{m^2}{s}, \\ z &= \pm 1e, \\ T &= 438K, \\ \varepsilon_r &= 4.0, \\ V &= 0.1V, \\ L &= 30\mu m. \end{aligned}$$

The expression presented in this paper provides a good qualitative approximation to the test problem, however the quantitative accuracy can be improved upon. This may be noticed in the value of the normalized local residual[5]

$$R(x,t) \coloneqq \left| \nabla \left(-D\nabla \frac{c}{c_0} - \frac{De}{kT} \nabla\Phi \frac{c}{c_0} \right) + \frac{1}{c_0} \frac{dc}{dt} \right|,$$

which appears sufficiently small with values as low as $1.22 \cdot 10^{-48}$ in the center of the domain and up to $3.49 \cdot 10^{-5}$ close to the boundary, but is large compared to residuals obtained from numerical solutions.

In order to compare the numerical and analytical approximations, we study the L_1 and L_∞ norms of the residual function. The evaluation of the analytical residual was obtained using mapleX [Map16]. For the analytical approximation we could not compute the L_∞ norm directly, but were forced to estimate it by checking for the maximum value of the residual function in table 5.5. We have collected the respective norm values in table 5.6, where we see that the numerical residual is several orders of magnitude lower than that of the analytical approximation. Consequently the analytical approximation has very little value, as the numerical solution of the system provides much better accuracy. These residuals ultimately translate to errors in the solution function, which may distort the relevant features of the system, such as the deviation from the initial concentration functions or the flux value.

5.3.4 Convergence Results

One of the most important properties for numerical schemes solving discretized differential equations is the respective convergence behavior. For sensible numerical schemes we generally expect that with increasing discretization effort the accuracy of the solution increases. So in addition to qualitative observations of solution behavior we also investigate the rates of convergence, which relate the effort spent on the solution with the reduction of the error.

[5] Recall that $c = c(x,t)$ and $\Phi = \Phi(x,t)$.

Point of evaluation	$t = 10$	$t = 100$	$t = 1000$
$R(0, t)$	$2.12 \cdot 10^{-46}$	$3.91 \cdot 10^{-47}$	$1.22 \cdot 10^{-48}$
$R(0.9 \cdot L, t)$	$1.51 \cdot 10^{-9}$	$1.51 \cdot 10^{-9}$	$1.51 \cdot 10^{-9}$
$R(0.99 \cdot L, t)$	$7.78 \cdot 10^{-6}$	$5.98 \cdot 10^{-6}$	$1.37 \cdot 10^{-5}$
$R(0.999 \cdot L, t)$	$1.45 \cdot 10^{-5}$	$1.77 \cdot 10^{-5}$	$3.49 \cdot 10^{-5}$
$R(L, t)$	$1.44 \cdot 10^{-5}$	$2.18 \cdot 10^{-5}$	$3.87 \cdot 10^{-5}$

Table 5.5: Value of the local residual $R(x, t)$ for the analytical approximative solution to the model problem.

Analytical approximation			
Norm	$t = 10$	$t = 100$	$t = 1000$
L_1	$9.01 \cdot 10^{-12}$	$8.87 \cdot 10^{-12}$	$1.82 \cdot 10^{-11}$
L_∞ (approx.)	$1.44 \cdot 10^{-5}$	$2.18 \cdot 10^{-5}$	$3.87 \cdot 10^{-5}$

Numerical approximation			
Norm	$t = 10$	$t = 100$	$t = 1000$
L_1	$1.12 \cdot 10^{-16}$	$1.17 \cdot 10^{-16}$	$7.46 \cdot 10^{-16}$
L_∞	$6.59 \cdot 10^{-14}$	$6.61 \cdot 10^{-14}$	$2.55 \cdot 10^{-13}$

Table 5.6: Norms of the residual function $R(x, t)$.

We compute the estimated error for the full solution vector, that is both species concentrations and the electric potential in their physical scaling units. The finest resolution in both space and time is considered the true solution u_0, and we compute

$$\epsilon_{g,t,k} = \frac{\|u_g^t - u_0\|_k}{\|u_0\|_k},$$

where the subscript g indicates the grid discretization, the superscript t the time discretization and the subscript k the norm type. We evaluate the norms L_1, L_2, L_∞, and the H_1 norm and H_1 seminorm.

As a benchmark system, we solve a one-dimensional test problem of the PNP system, in this case without the coupled heat equation. The system represents a crude one-dimensional approximation to a battery sytem with fixed current across the boundaries. The simulation domain is $[0 : L] \times [0 : t_{end}]$ with $L = 5 \cdot 10^{-5} m$ and $t_{end} = 10s$. The discretization consists of finite elements of order one, the temperature is held constant at $T = 438K$.

For the Poisson equation we set $\varepsilon_r = 4.0$ and the Dirichlet boundary conditions of $\Phi(0) = 0$ and $\Phi(1) = 0.1$.

Property	Symbol	Unit	Species 0	Species 1
Charge	z	e	$+1$	-1
Diffusion coefficient	D	$\frac{m^2}{s}$	$1.0 \cdot 10^{-16}$	$1.0 \cdot 10^{-16}$
Initial concentration	c_0	$\frac{1}{m^3}$	$6.022142 \cdot 10^{19}$	$6.022142 \cdot 10^{19}$
BC at $x = 0$	J_0	$\frac{1}{m^2 \cdot s}$	$6.022142 \cdot 10^{12}$	$6.022142 \cdot 10^{12}$
BC at $x = 1$	J_1	$\frac{1}{m^2 \cdot s}$	$-6.022142 \cdot 10^{12}$	$-6.022142 \cdot 10^{12}$

Table 5.7: Species properties used in the convergence tests.

We simulate two ionic species with the properties listed in table 5.7.

Separate Time and Space Convergence

We present separate convergence results for refinement in the time discretization and the space discretization in figure 5.16. In figure 5.16a we see that the initial grids do not sufficiently resolve the solution behavior, as the preasymptotic behavior of the error is near constant for the initial refinement steps. However, after passing a certain threshold of degrees of freedom, the convergence rate of the $L_.$ norms is of second order while the convergence order of the H_1 based norms is of first order, as we would expect from general finite elements. Furthermore we notice that the graphs for the relative error of the H_1 norm and the H_1 seminorm lie exactly on top of each other. This is due to the fact, that the absolute error values of the H_1 seminorm are several orders of magnitude larger than the L_2 error, leading to the domination of the H_1 error by the H_1 seminorm.

From figure 5.16b we can deduce that there is no preasymptotic plateau for the time refinement. Throughout the refinement process, the error show first order convergence with respect to all grid norms, as we expect from a time discretization with an implicit Euler method.

Combined Time and Space Convergence

Following general practice, we will test whether the separate convergence rates can be combined. To account for the preasymptotic plateau in the error during the grid refinement, we begin the joint refinement on a finer grid, which is sufficiently fine to resolve the solution characteristics. The measurement is started on level zero with $\delta x_0 = \frac{1}{320}$ and $\delta t_0 = 1.0$. For subsequent levels we set $\delta x_n = \frac{\delta x_{n-1}}{2}$ and $\delta t_n = \frac{\delta t_{n-1}}{4}$.

The levels show the relative error value

$$\epsilon_{n,k} = \frac{\|u_n(t_{end}) - u_N(t_{end})\|_k}{\|u_N(t_{end})\|_k}, \tag{5.1}$$

where ϵ denotes the error, n the current refinement level, N the maximum computed refinement level and k the norm type being used. The maximum level with which

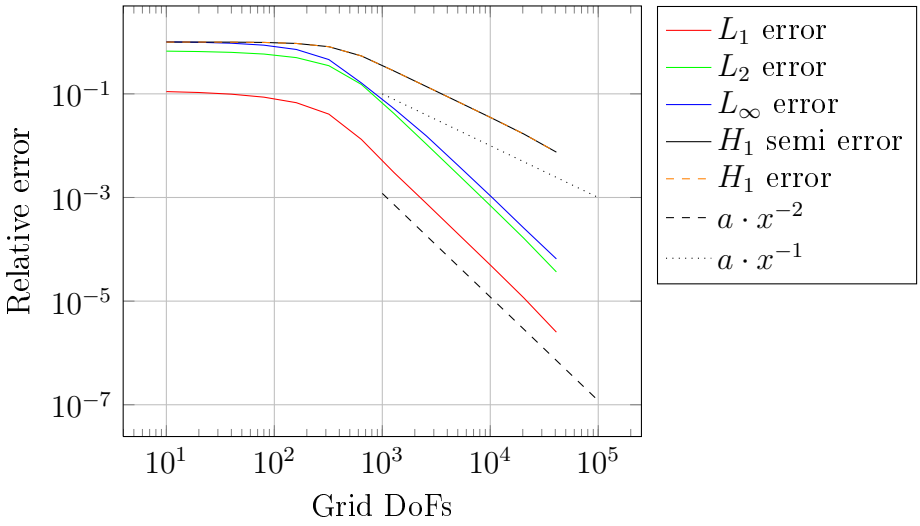

(a) Grid convergence at constant $\delta t = 9.77 \cdot 10^{-4}$.

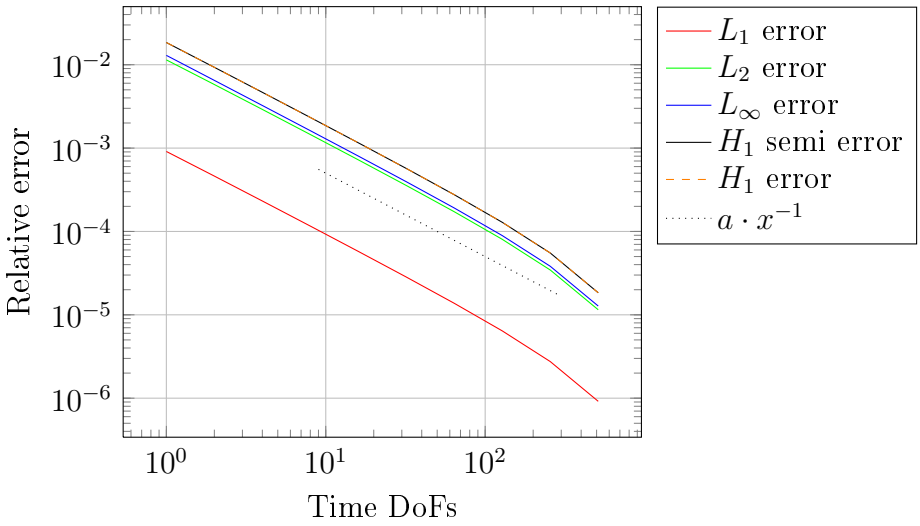

(b) Time convergence on grid with 10240 cells.

Figure 5.16: Separate convergence results for the one-dimensional test case with inhomogeneous flux boundary conditions.

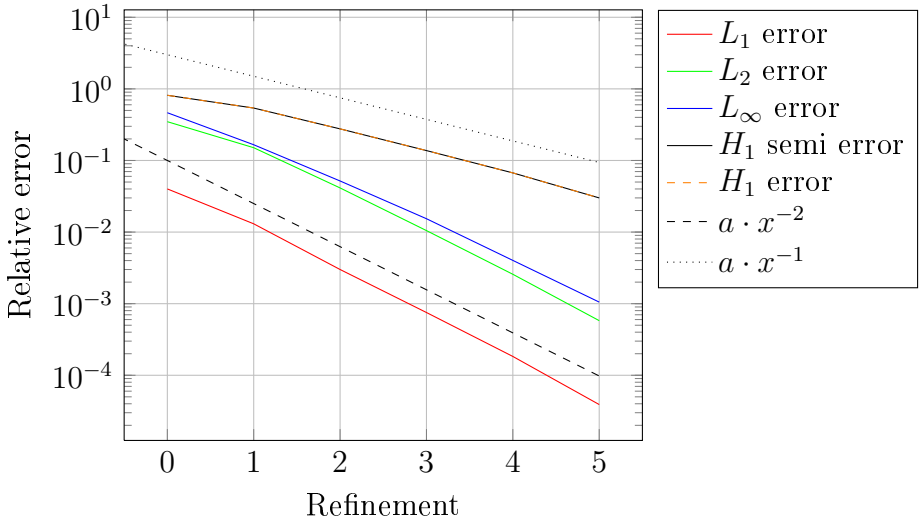

Figure 5.17: Convergence of coupled PNP system with constant temperature.

Relative error of concentration and potential functions						
#cells	δt	L_1	L_2	L_∞	H_1 semi	H_1
320	1	$4.01 \cdot 10^{-2}$	$3.48 \cdot 10^{-1}$	$4.65 \cdot 10^{-1}$	$8.14 \cdot 10^{-1}$	$8.14 \cdot 10^{-1}$
640	$2.50 \cdot 10^{-1}$	$1.30 \cdot 10^{-2}$	$1.51 \cdot 10^{-1}$	$1.66 \cdot 10^{-1}$	$5.40 \cdot 10^{-1}$	$5.40 \cdot 10^{-1}$
1280	$6.25 \cdot 10^{-2}$	$3.00 \cdot 10^{-3}$	$4.14 \cdot 10^{-2}$	$5.17 \cdot 10^{-2}$	$2.76 \cdot 10^{-1}$	$2.76 \cdot 10^{-1}$
2560	$1.56 \cdot 10^{-2}$	$7.53 \cdot 10^{-4}$	$1.05 \cdot 10^{-2}$	$1.54 \cdot 10^{-2}$	$1.37 \cdot 10^{-1}$	$1.37 \cdot 10^{-1}$
5120	$3.91 \cdot 10^{-3}$	$1.83 \cdot 10^{-4}$	$2.57 \cdot 10^{-3}$	$4.02 \cdot 10^{-3}$	$6.71 \cdot 10^{-2}$	$6.71 \cdot 10^{-2}$
10240	$9.77 \cdot 10^{-4}$	$3.90 \cdot 10^{-5}$	$5.79 \cdot 10^{-4}$	$1.05 \cdot 10^{-3}$	$3.00 \cdot 10^{-2}$	$3.00 \cdot 10^{-2}$

Table 5.8: Relative error of the coupled Poisson-Nernst-Planck system with constant temperature.

Property	Symbol	Unit	Species 0	Species 1
Charge	z	F	$+1$	-1
Diffusion coefficient	D	$\frac{m^2}{s}$	$1.0 \cdot 10^{-4}$	$1.0 \cdot 10^{-4}$
Initial concentration	c_0	$\frac{mol}{m^3}$	1.0	1.0
BC at $x = 0$	J_0	$\frac{mol}{m^2 s}$	0.0	0.0
BC at $x = 1$	J_1	$\frac{mol}{m^2 s}$	0.0	0.0

Table 5.9: Properties of the species used in the convergence test with the heat equation.

we compare in this benchmark is level 6 with $\delta x_6 = \frac{1}{20480}$ and $\delta t_6 = \frac{1}{4096} = 2.44 \cdot 10^{-4}$, which does not appear as a measurement as the error result would, by its very definition in (5.1), be zero.

The results are presented in figure 5.17 and table 5.8. We see that the error in the $L_\cdot$ norms still decrease with second order, while the H_1 norm and seminorm error decrease with first order in terms of refinement steps. Since each refinement step represents two steps of the previous time refinement, the results from the joint refinement process are consistent with those from the separate refinement.

5.4 Simulation of the Coupled Heat-Poisson-Nernst-Planck System

In the previous benchmark, the temperature was kept constant. In the following setup we will investigate the fully coupled Heat-Poisson-Nernst-Planck system, observing the convergence behavior for both, the vector of species and potential functions and the temperatur solution. For the second benchmark, we utilize the general setup of the previous one with some modifications. With the homogeneous boundary conditions, this setup may be regarded as a crude model for a capacitor instead of a battery.

The problem is one-dimensional with the simulation domain $[0 : L] \times [0 : t_{end}]$ with $L = 1.0m$ and $t_{end} = 10s$. The discretization consists of finite elements of order one, the temperature begins at $T = 438K$. As before we set $\varepsilon_r = 4.0$ and Dirichlet boundary conditions of $\Phi(0) = 0$ and $\Phi(1) = 0.1$ for the Poisson equation. For the heat equation we set the thermal diffusivity $k = 1.0$ and boundary conditions $T(0) = 300K$ and $T(1) = 300K$. The coupling is set to $\beta = 1.0 \cdot 10^2 \cdot \|\nabla\Phi\|$. The properties of the two ionic species are listed in table 5.9.

Again, the measurement is started on level zero with $\delta x_0 = \frac{1}{320}$ and $\delta t_0 = 1.0$. For subsequent levels we set $\delta x_n = \frac{\delta x_{n-1}}{2}$ and $\delta t_n = \frac{\delta t_{n-1}}{4}$.

For the PNP solution we measure the error exactly as before (5.1), and use the

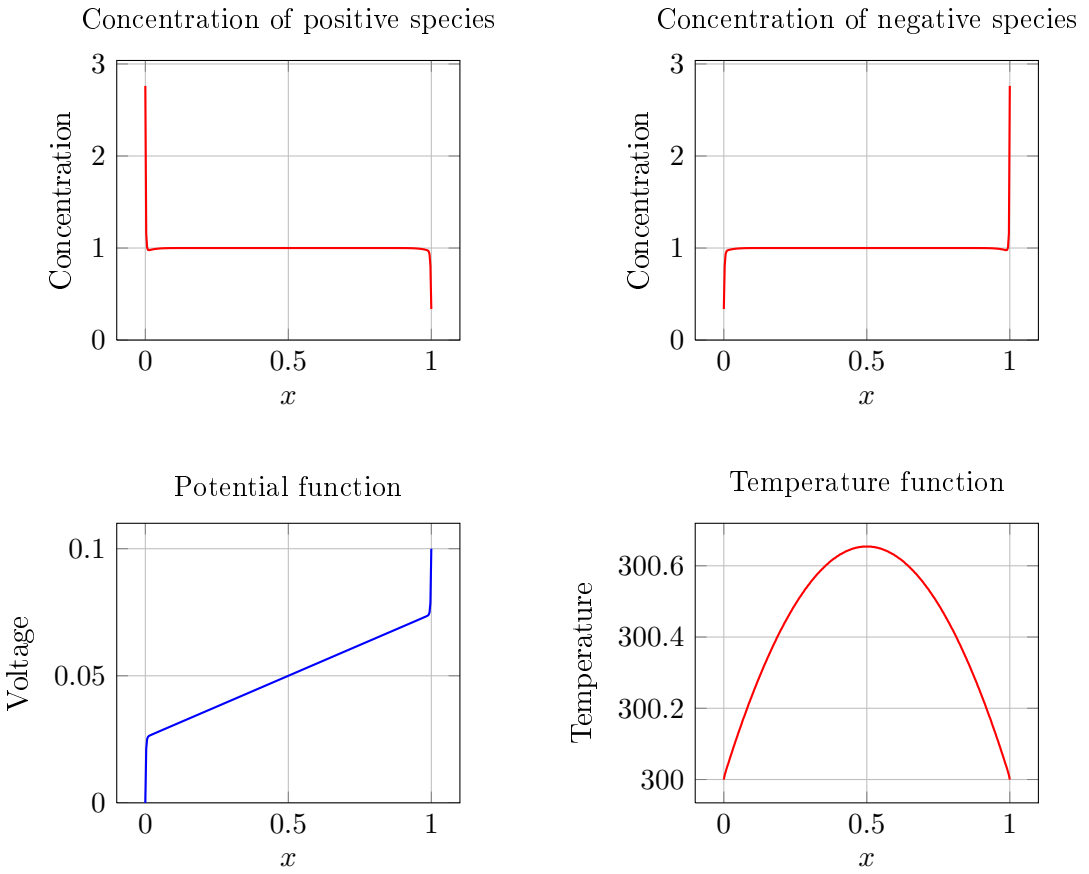

Figure 5.18: Solution functions for the coupled Heat-Poisson-Nernst-Planck system.

equivalent formula for the solution of the heat equation

$$\epsilon_{n,k} = \frac{\|T_n(t_{end}) - T_N(t_{end})\|_k}{\|T_N(t_{end})\|_k},$$

where all entries are as before, but we exchanged the vector valued function $\vec{u}(x,t)$ with the scalar function $T(x,t)$. As before, the maximum level N with which we compare in this benchmark is level 6.

We show the structure of the four different solution functions in figure 5.18, where we clearly see the dominance of the boundary behavior for the concentration functions and the electric potential, which can be interpreted as the formation of an electric double layer.

Convergence on uniform grids

Given the previous results, the results on uniform grids displayed in figure 5.19 do not hold any surprises. The convergence behavior for the Poisson-Nernst-Planck solution

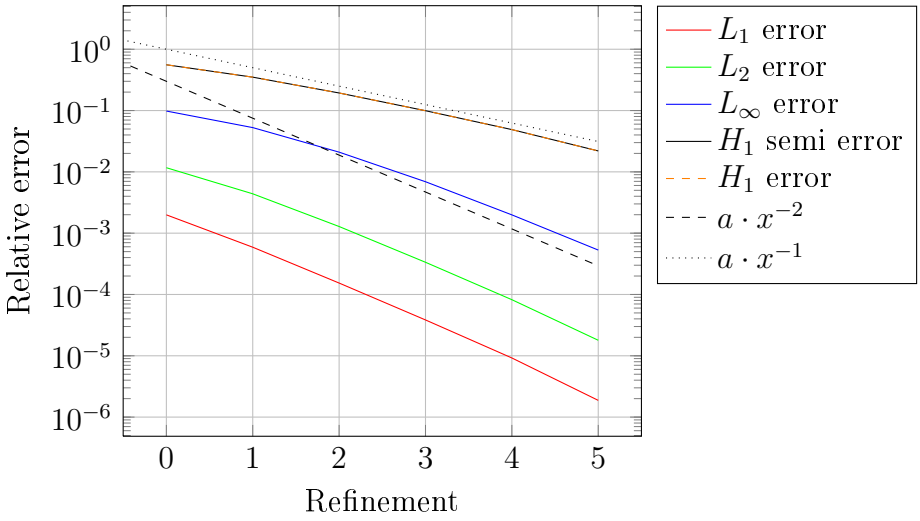

(a) Convergence of the concentration and potential functions.

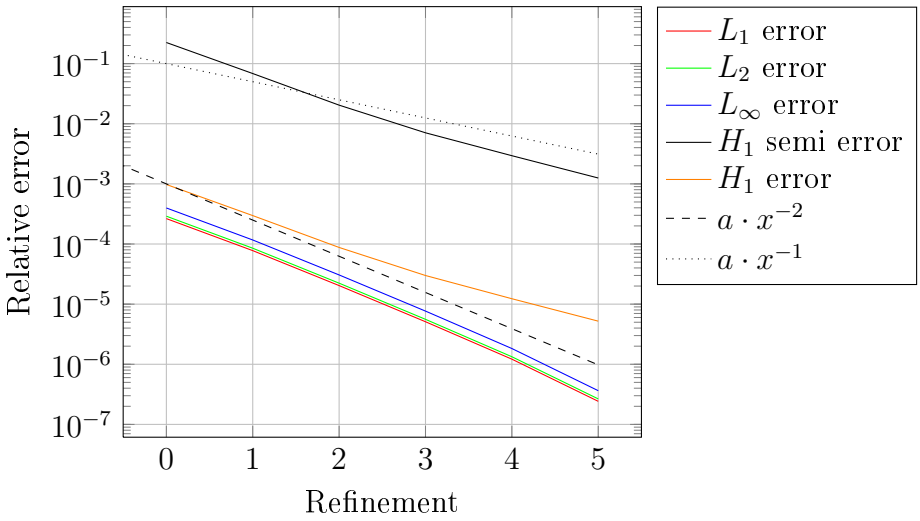

(b) Convergence of the temperature function.

Figure 5.19: Convergence of the coupled Heat-Poisson-Nernst-Planck system on uniform grids.

Relative error of concentration and potential functions						
#cells	δt	L_1	L_2	L_∞	H_1 semi	H_1
320	1	$1.99 \cdot 10^{-3}$	$1.17 \cdot 10^{-2}$	$9.82 \cdot 10^{-2}$	$5.58 \cdot 10^{-1}$	$5.58 \cdot 10^{-1}$
640	$2.50 \cdot 10^{-1}$	$5.90 \cdot 10^{-4}$	$4.39 \cdot 10^{-3}$	$5.27 \cdot 10^{-2}$	$3.51 \cdot 10^{-1}$	$3.50 \cdot 10^{-1}$
1280	$6.25 \cdot 10^{-2}$	$1.54 \cdot 10^{-4}$	$1.28 \cdot 10^{-3}$	$2.10 \cdot 10^{-2}$	$1.93 \cdot 10^{-1}$	$1.93 \cdot 10^{-1}$
2560	$1.56 \cdot 10^{-2}$	$3.84 \cdot 10^{-5}$	$3.35 \cdot 10^{-4}$	$6.90 \cdot 10^{-3}$	$9.94 \cdot 10^{-2}$	$9.94 \cdot 10^{-2}$
5120	$3.91 \cdot 10^{-3}$	$9.22 \cdot 10^{-6}$	$8.22 \cdot 10^{-5}$	$1.99 \cdot 10^{-3}$	$4.89 \cdot 10^{-2}$	$4.89 \cdot 10^{-2}$
10240	$9.77 \cdot 10^{-4}$	$1.87 \cdot 10^{-6}$	$1.79 \cdot 10^{-5}$	$5.30 \cdot 10^{-4}$	$2.19 \cdot 10^{-2}$	$2.19 \cdot 10^{-2}$

Relative error of temperature function						
#cells	δt	L_1	L_2	L_∞	H_1 semi	H_1
320	1	$2.64 \cdot 10^{-4}$	$2.90 \cdot 10^{-4}$	$3.98 \cdot 10^{-4}$	$2.24 \cdot 10^{-1}$	$9.77 \cdot 10^{-4}$
640	$2.50 \cdot 10^{-1}$	$7.76 \cdot 10^{-5}$	$8.51 \cdot 10^{-5}$	$1.17 \cdot 10^{-4}$	$6.84 \cdot 10^{-2}$	$2.97 \cdot 10^{-4}$
1280	$6.25 \cdot 10^{-2}$	$2.03 \cdot 10^{-5}$	$2.23 \cdot 10^{-5}$	$3.06 \cdot 10^{-5}$	$2.04 \cdot 10^{-2}$	$8.77 \cdot 10^{-5}$
2560	$1.56 \cdot 10^{-2}$	$5.10 \cdot 10^{-6}$	$5.59 \cdot 10^{-6}$	$7.66 \cdot 10^{-6}$	$7.07 \cdot 10^{-3}$	$2.99 \cdot 10^{-5}$
5120	$3.91 \cdot 10^{-3}$	$1.22 \cdot 10^{-6}$	$1.33 \cdot 10^{-6}$	$1.83 \cdot 10^{-6}$	$2.94 \cdot 10^{-3}$	$1.23 \cdot 10^{-5}$
10240	$9.77 \cdot 10^{-4}$	$2.42 \cdot 10^{-7}$	$2.65 \cdot 10^{-7}$	$3.64 \cdot 10^{-7}$	$1.25 \cdot 10^{-3}$	$5.21 \cdot 10^{-6}$

Table 5.10: Relative error of the coupled Heat-Poisson-Nernst-Planck system.

shows the same behavior as in the test cases with constant temperature. The solution to the heat equation shows similar behavior, as the $L_.$ norms converge with second order. The H_1 norm and seminorm initially show an error reduction which is closer to second than to first order, however after some refinement steps the slope is reduced and shows standard behavior. Compared to the concentration and potential functions we notice that the H_1 norm and seminorm curves are clearly separated, indicating that the absolute values of the error in the derivative are clearly not as dominant.

5.4.1 Convergence on Graded Grids

As we can see in figure 5.18, the dominant changes in the solution functions occur on the boundary of the domain. As discussed in section 4.4.3 of the previous chapter, this was to be expected and leads to the assumption of non-uniform error distribution on the domain, which we counter by grading the distribution of degrees of freedom.

As an initial approach we investigate a grading function, which distributes all additional degrees of freedom towards the boundary and leaving the interior points static.

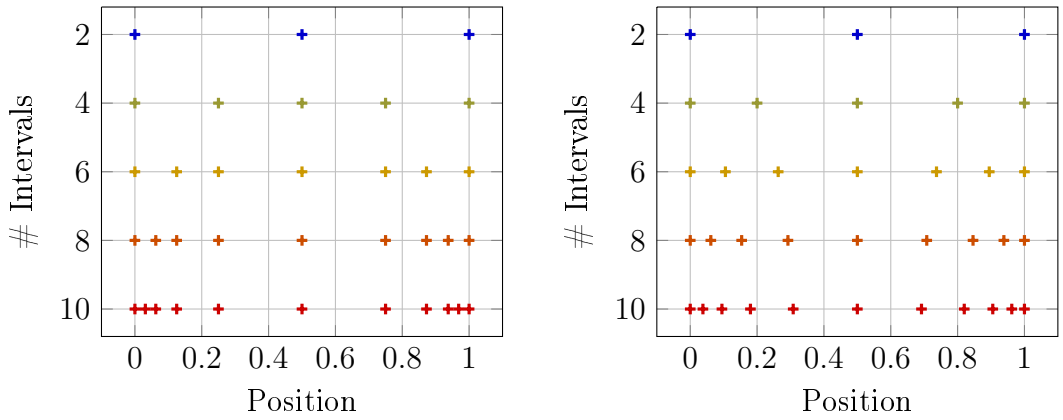

Figure 5.20: Comparison of first five instances of graded grids, 'naive' grading left, improved grading right. It can be clearly seen that the naive grading exclusively refines towards the interval boundary, while the improved grading refines all elements of the grid.

For an interval $[a, b]$ we let N be an even number and set the grid points

$$x_j = \begin{cases} a & \text{if } j = 0 \\ a + \frac{b-a}{2} \cdot 2^{-\left(\frac{N}{2} - j\right)} & \text{if } 0 < j \leq \frac{N}{2} \\ b - \frac{b-a}{2} \cdot 2^{-\left(j - \frac{N}{2}\right)} & \text{if } \frac{N}{2} < j < N \\ b & \text{if } j = N \end{cases}$$

which are exponentially finer towards the boundary of the domain, compare figure 5.20.

Comparing these grids among themselves by the scheme used in the previous section, figure 5.21a initially seems to indicate that exponential convergence could be achieved. Even the error in the $L_\cdot$ norms of the temperature function appears to decrease, despite the fact the error in the solution of the heat equation is expected to be uniform on the domain. However, this measurement is incomplete. A comparison of the solution on the refined graded grids to the full grid solution results in stagnation after a certain point, indicating that the series of solutions on the graded grids converges to a different solution than those on the full grids, compare figure 5.21b.

Since additional degrees of freedom are spent exclusively towards the boundary, the error on the interior is not reduced and consequently the solution does not converge to the full grid solution. Thus we present the following improved distribution of finite

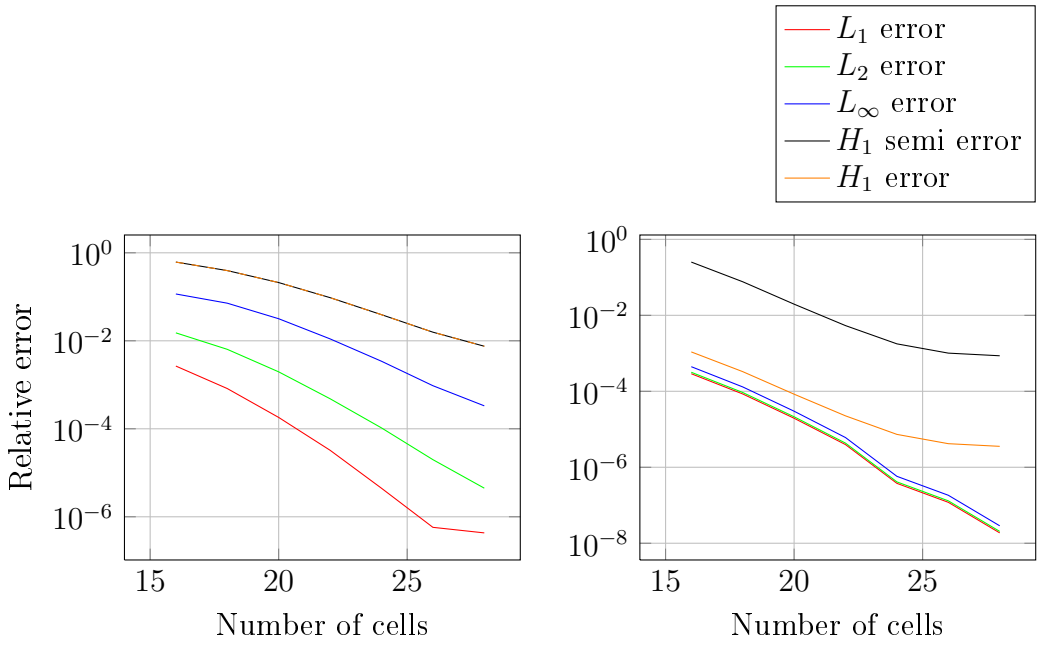

(a) Comparison with finest graded grid, PNP left, heat right.

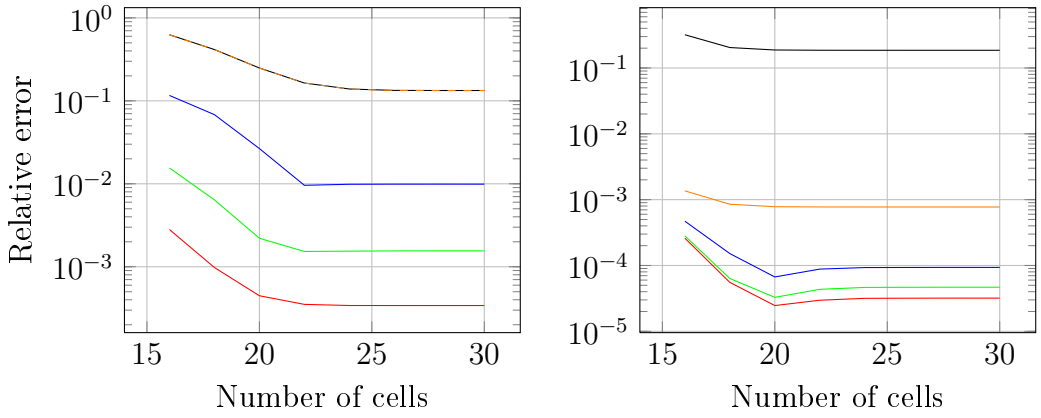

(b) Comparison with finest full grid, PNP left, heat right.

Figure 5.21: (Failing) convergence on naively graded grids.

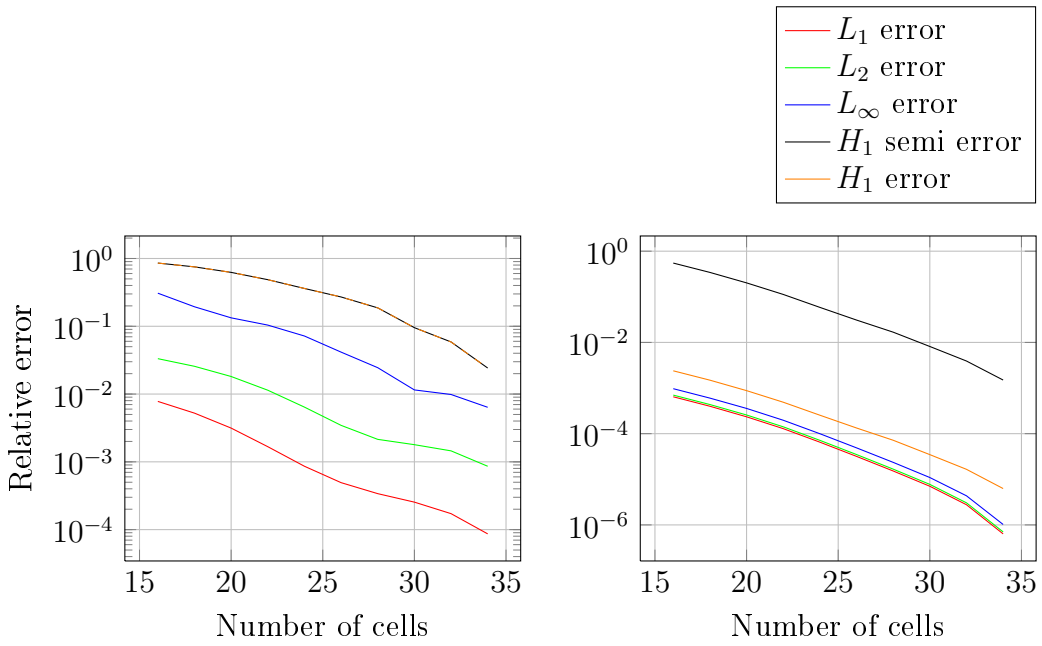

(a) Comparison with finest graded grid. PNP left, heat right.

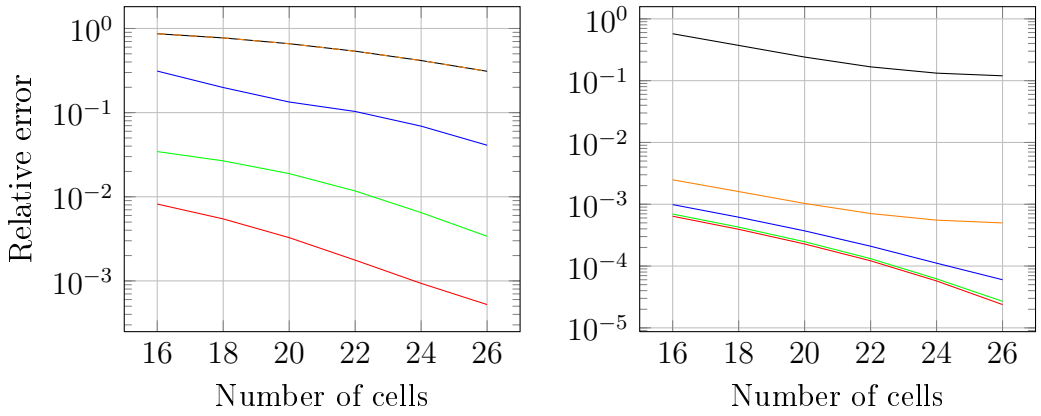

(b) Comparison with finest full grid. PNP left, heat right.

Figure 5.22: Convergence on grids with improved grading.

element points

$$x_j = \begin{cases} a & \text{if } j = 0 \\ a + \frac{(b-a)}{2} \cdot \left(2^{\frac{N}{2}-1} \cdot \frac{a_j}{a_{\frac{N}{2}} \cdot 2^{\frac{N}{2}-1}} \right) & \text{if } 0 < j \leq \frac{N}{2} \\ b - \frac{(b-a)}{2} \cdot \left(2^{\frac{N}{2}-1} \cdot \frac{a_{(N-j)}}{a_{\frac{N}{2}} \cdot 2^{\frac{N}{2}-1}} \right) & \text{if } \frac{N}{2} < j < N \\ b & \text{if } j = N \end{cases}$$

$$a_i = \frac{\left(\frac{3}{2}\right)^i - 1}{\frac{3}{2} - 1} = 2 \cdot \left(\frac{3}{2}\right)^i - 2.$$

This grading still refines the grid exponentially towards the boundary, but with a factor of $\frac{2}{3}$ instead of $\frac{1}{2}$. As a direct result, subsequent grids do not have identical grid points, but all intervals/finite elements are refined, see figure 5.20.

When comparing this new grading against the finest graded grid, we notice that we are not achieving the same – seemingly ideal – rates as the naively graded grids, compare 5.22a. However, we need to remind ourselves that the exponential convergence of the naive grids was only achieved compared to grids of the same type, while comparison with the full grid showed stagnation of the error. In contrast, the solution functions on the better graded grids converge not only towards the solution of the fines graded grid, but also towards the solution of the finest full grid, as demonstrated in figure 5.22b. The convergence rates are an improvement compared to the convergence rates on the uniformly refined grids, see table 5.11. There we see, that the convergence rates initially increase with additional degrees of freedom. However hopes for exponential convergence are not fulfilled, as the convergence rates drop infrequently. Nevertheless, the reduction in error compared to the effort in degrees of freedom is substantial. The low amounts of ressources spent on the refined graded grids allows us to reach far higher levels of refinement compared to the uniform grid refinement.

5.4.2 Adaptive Refinement

Finally, we compare the performance of the graded grids with an adaptive refinement based on the Kelly error estimator [KGZB83], which we already introduced in section 4.4.3. Several different approaches to adaptivity and the underlying error estimation can be taken. In this case, we let the solver take ten timesteps on the current coarse grid before estimating the error on this grid and refining a preset fraction of the cells for which the estimated error is largest. Selecting a fixed fraction of the cells allows to retain control of the degrees of freedom accumulated over several iterations of the refinement procedure. Furthermore, the absolute value of the error estimated by the Kelly procedure does not necessarily coincide with the actual error, since it is based on the generalized poisson problem. In our particular test case we set this fraction to

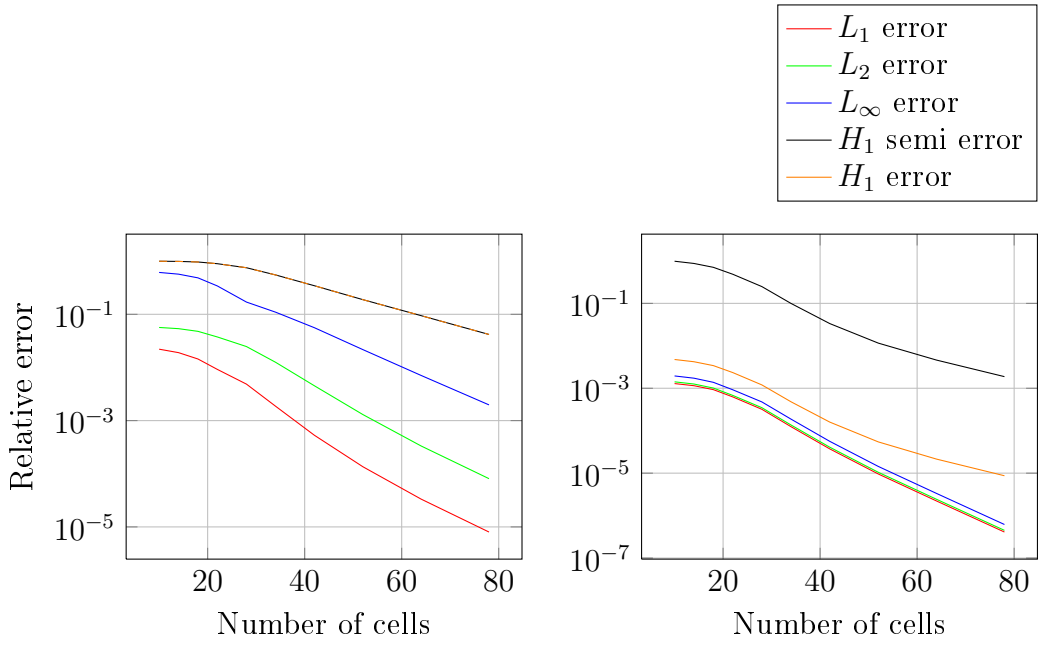

(a) Comparison with finest adaptive refinement, PNP left, heat right.

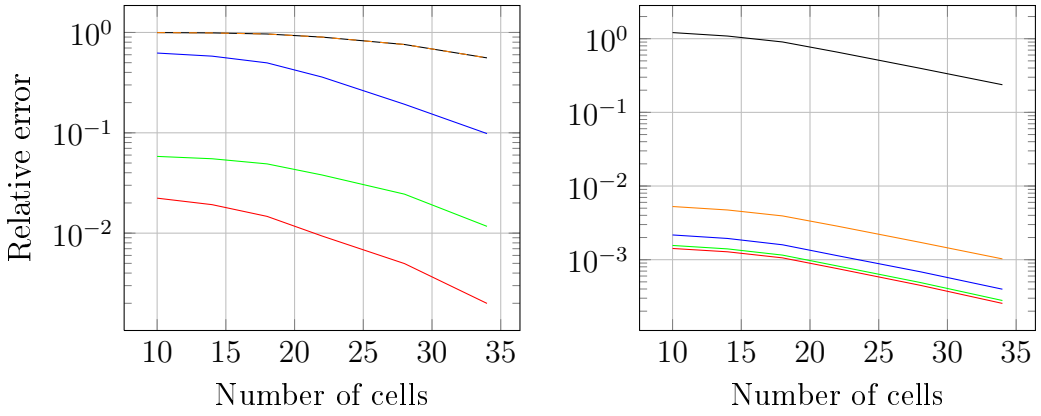

(b) Comparison with finest full grid, PNP left, heat right.

Figure 5.23: Convergence on adaptively refined grids.

Convergence rates						
#cells	δt	L_1	L_2	L_∞	H_1 semi	H_1
16	1	3.38	2.20	3.92	1.10	1.10
18	$2.50 \cdot 10^{-1}$	4.82	3.29	3.57	1.78	1.78
20	$6.25 \cdot 10^{-2}$	6.63	4.89	2.58	2.60	2.60
22	$1.56 \cdot 10^{-2}$	7.64	6.60	4.26	3.43	3.43
24	$3.91 \cdot 10^{-3}$	6.96	7.75	6.83	3.61	3.61
26	$9.77 \cdot 10^{-4}$	5.04	6.42	7.14	4.99	4.99
28	$2.44 \cdot 10^{-4}$	4.18	2.62	1.09	9.75	9.75
30	$6.10 \cdot 10^{-5}$	6.06	3.25	2.40	7.51	7.51
32	$1.53 \cdot 10^{-5}$	11.38	8.63	7.18	14.60	14.60

Table 5.11: Table of convergence order $p = \ln\left(\frac{\epsilon_{i-1}}{\epsilon_i}\right) \Big/ \ln\left(\frac{n_i}{n_{i-1}}\right)$ on grids with improved grading. Note the low increase in cell numbers.

20%, while at the same time setting $\delta t^{k+1} = \frac{\delta t^k}{2}$. For the next step the refined grid becomes the current coarse grid and the procedure is iterated.

In figure 5.23a we have plotted the convergence of the refined error. Compared to the previous results from the graded grids, we are able to produce much lower relative error values. However, this result is only achieved at some cost, when we compare the number of cells used for each result. Just by counting the degrees of freedom, the improved graded grids and the adaptive refinement achieve results where the error is of the same order. In order to construct the adaptive refinement however, we needed to solve the problem several times on the coarser grids, adding additional computational expenses. Thus we conclude that for suitable problems, where the location of the error can be estimated to be on or close to the boundaries, the grids relying on improved grading are the premium choice, while the adaptive grids have their merits for problems with unknown characteristics.

5.5 Computation of Derived Properties and Sensitivity Analysis

Similarly to the fact that in the molecular dynamics simulation the individual trajectories are not the final objective of the simulation, scientists involved in physical or material research are ultimately interested in values derived from the solutions to the macroscopic Differential Equations, which characterize a specific performance property which they intend to improve. Actual application of simulation to engineering problems also carries additional challenges. Often input data is not a single set of

exact values, either due to missing information, inaccurate measurements or varying production results. In order to quantify the uncertainty of the resulting values in dependence of the input uncertainty, it is important to identify critical parameters which have a strong influence on the output, as opposed to parameters whose influence on the measured values are insignificant.

In the following section we will compute solutions to the PNP with physical parameters and boundary conditions geared towards a specific objective in the field of battery research. In particular, we will use the potential and concentration profiles to compute the conductivity of the simulated ion solution, as well as the relative contributions of the individual ions to the current, which is generally known as the transference number.

Furthermore, we will use some tools from the field of uncertainty quantification to study the influence of input parameters on the resulting variables. The results of the sensitivity analysis are not only relevant for this particular application, but allow general considerations which parameters have the strongest influence on the simulation results.

Most of the work described in this chapter was carried out within contract for BASF[6].

The scope of the project was

- to investigate transport parameters with methods based on finite elements,
- specifically to obtain the conductivity and transference number in dependence of the salt concentration
- and to perform sensitivity analysis on the results.

Specifications for the design of the experiment and the material parameters used were provided by BASF. The permission of BASF to publish the results of this work in the scope of this thesis is gratefully acknowledged.

5.5.1 Parameters and Design of Experiment

The simulation is intended to reproduce experiments of lithium hexafluorophosphate ($LiPF_6$) salt in 1:1 ethylene carbonate (EC) and dimethyl carbonate (DMC) electrolyte, a mixture which is commonly found in current battery systems.

The diffusion and chemical potential parameters for different concentrations were provided by BASF, see table 5.12.

[6] BASF SE is an internationally operating company with its headquarters in Ludwigshafen, Germany. The company was founded 1865 as "Badische Anilin und Soda Fabrik" producing dyes. Since then it has significantly expanded its portfolio, providing chemical solutions to a wide range of industrial areas. As of 2015, approximately 112,000 employees produced a revenue of 70,449 million € [BAS].

Salt concentration $\left[\frac{mol}{l}\right]$	Diffusion $\left[10^{-10}\frac{m^2}{s}\right]$		Chemical potential $\left[\frac{kJ}{mol}\right]$	
	Li	PF_6	Li	PF_6
0.1	4.67	7.03	−5.45468	2.38352
0.3	3.87	6.12	−5.16606	2.25229
0.5	3.43	5.03	−4.93180	2.14444
0.7	3.02	4.30	−4.73788	2.05417
0.9	2.58	3.53	−4.57703	1.98041
1.0	2.24	3.29	−4.50650	1.94811
1.1	2.00	2.94	−4.44203	1.91882
1.3	1.67	2.51	−4.32887	1.86804
1.5	1.39	1.84	−4.23319	1.82647
1.7	1.12	1.63	−4.15168	1.79188

Table 5.12: Diffusion and chemical potential of $LiPF_6$ in 1:1 EC:DMC at 25°C as measured by BASF.

Further parameters are

- the length of a cell $L = 0.5mm$,
- the voltage $U_0 = 0.01V$,
- the dielectricity constant $\varepsilon_r = 25$,
- the double layer capacitance $\hat{C} = 10\frac{\mu f}{cm^2}$.

The first two of these parameters are exact, as they are external parameters of the setup. The parameters ε and $\hat{C}$ however are potentially inaccurate, as they were only estimated. The dielectricity is known for pure EC:DMC mixture (measured to be 36), but the value of the dielectricity will decrease as soon as salt is added to the mixture. Therefore, we use an estimated value of 25 and will need to pay special attention to the sensitivity of the results to the dielectricity. Similarly, the capacitance of the double layer at the electrode is an estimate established with the experts at BASF during the course of the project [Gol14].

5.5.2 Results

Conductivity

The simulations are carried out with isolating boundary conditions for the ion flux, setting

$$D_i \left(\nabla c_i + \frac{z_i F}{RT} c_i \nabla \Phi + \frac{1}{RT} c_i \nabla \mu_i \right) = 0$$

at the electrode positions. For the electric field Robin boundary conditions as introduced in section 4.3.4 are used with the coefficients derived from the capacitor equations on the electrode surface [LFJ11]

$$\nabla \Phi \cdot \vec{n} = \frac{\hat{C}}{\varepsilon} \Phi - \frac{\hat{C}}{\varepsilon} \Phi_0,$$

where $\Phi_0(0) = 0$ and $\Phi(L) = U_0$.

For the computation of the conductivity, the current I is measured in the bulk over the simulation time of $0.1s$ and its decreasing curve is fitted to $I(t) = I_0 \cdot exp(-\frac{t}{\tau})$, the charging current of a capacitor. The conductivity follows from the quotient $\frac{I_0 \cdot L}{U_0 \cdot A}$ [Moo10]. For the projected cross section on the 1D simulation we use an area of $1m^2$.

In the simulation results presented in figure 5.24a we observe a monotonous increase of the conductivity between the concentration values $0.1\frac{mol}{l}$ and $0.95\frac{mol}{l}$. At $0.95\frac{mol}{l}$ a maximum of $1.97 \cdot 10^{-2}\frac{S}{cm}$ is reached. For higher concentrations the conductivity shows a decreasing tendency, however it is not monotonous, displaying another local maximum at $1.25\frac{mol}{l}$.

Comparison of simulation results of conductivity with experimental values is only possible to a limited extend. While the input parameters for the PNP were measured at 25°C, the conductivity measurements were carried out at 35°C. In order to address this mismatch, the simulation was carried out with the input values as reported, however the simulation temperature was set to 35°C. Nevertheless, we expect some deviation in the quantitative results, as critical values such as diffusion coefficients and chemical potential are expected to vary with such a significant increase in temperature. In order to address this issue, extended analysis of simulation uncertainty is performed.

Furthermore, the density of experimentally obtained samples is considerably lower than the one of the simulation results (11 vs. 65 data points, compare tables 5.18 and 5.17). In the experiment no individual error estimates for the data points were obtained, but the general accuracy of the method was estimated to be around 1.5% [Eid16].

Nevertheless, the two plots of the respective data show considerable similarity in their qualitative behavior, see figure 5.24. The graph presenting the experimental results also shows two local maxima, $1.52 \cdot 10^{-2}\frac{S}{cm}$ at $0.9\frac{mol}{l}$ and $1.55 \cdot 10^{-2}\frac{S}{cm}$ at $1.1\frac{mol}{l}$, the locations of which are in very good agreement with the locations of the

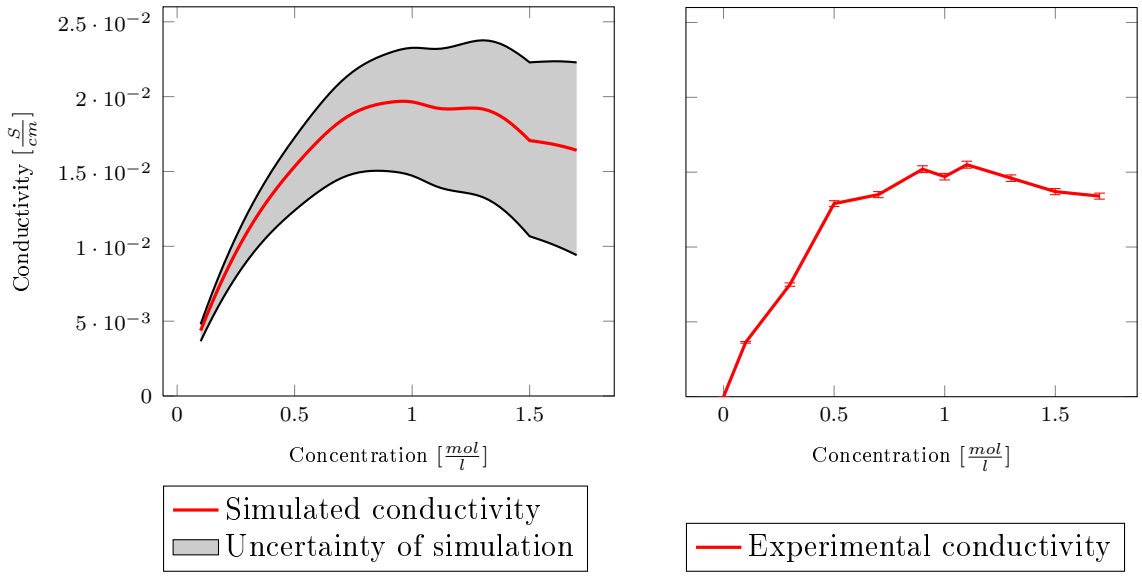

(a) Simulation results with uncertainty from input values. A complete list of results can be found in table 5.18.

(b) Experimental results with an error estimate of 1.5%. A complete list of results can be found in table 5.17.

Figure 5.24: Conductivity in dependence on concentration.

maxima in the simulated results. Further similarity can be seen in the subsequent decrease of the conductivity for higher concentrations, as both curves show a final increase in the slope.

Despite the mismatch in the experimental temperature, we observe a high agreement in the qualitative behavior of the conductivity data for simulation and experiment. The quantitative results are measurably lower in the experiment, however still within the region of uncertainty, which is more than was to be expected for the mismatching coefficients.

Transference Number

In the following, we precede the computation of the transference number t^+ with a computation of the conductivity at the corresponding concentration at isolating boundary conditions as described in the previous chapter in order to obtain the conducted current. However, in contrast to the simulations in the previous section, here we used a simulation temperature of 25°C, which coincides with the temperature at which the input coefficients were obtained.

In a follow up simulation, we use the obtained current I_0 to set the appropriate

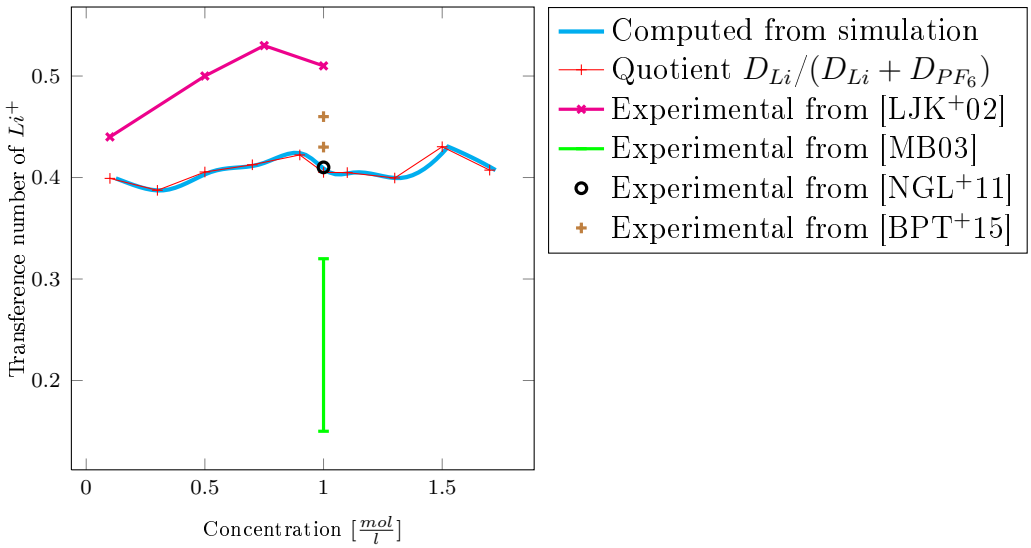

Figure 5.25: Transference number in dependence of concentration. Numeric results can be found in table 5.19.

boundary conditions for the Li-current

$$D_i \left(\nabla c_i + \frac{z_i F}{RT} c_i \nabla \Phi + \frac{1}{RT} c_i \nabla \mu_i \right) = I_0$$

in order to have a proper representation of non-isolating electrodes on the boundary for the computation of the transference number [Zug11]. As before, we assume a cross section of $1m^2$ for the 1D projection.

In order to compute the transference number, the ion flux of the individual species is measured in the bulk. The transference number is the quotient $\frac{I_{Li}}{I_{total}}$ [Zug11].

The transference number of the lithium ion derived from the simulation does not show clear dependence on the concentration. The expectation on this behavior is disputed in the literature. While some experiments observe no significant variation [VR05], others report a clear trend in concentration dependence [ZFA+11]. However, the latter survey does not give error indicators and the quantitative trend is lower than the errors indicated in other works.

In comparison with the quotient of the diffusion coefficients $D_{Li}/(D_{Li}+D_{PF_6})$, a very high qualitative and quantitative similarity of the curves can be noticed, compare figure 5.25. This relation can be expected for dissociated electrolytes and furthermore corresponds with the experimental method for measurement of the transference number via NMR spectroscopy [Zug11].

Other experimental data from [NGL+11] fits exceptionally well with our results, although we need to point out, that values given in the literature vary significantly, with e.g. [LJK+02], [BPT+15] and [MB03] giving values for the transference number

both higher and lower than our results. However we would like to draw attention to the fact that the more recent experimental results are closer to our simulation output.

Together with the results of the sensitivity analysis, which we present in the following section, we obtain the impression of close – and in its tendency distinct – dependency of the transference number values on the relation of diffusion coefficients.

5.5.3 Sensitivity Analysis

In this section we will analyze the effect that possible deviations of the input data would have on the simulation results. We will achieve this by various repetitions of the simulations with varying input parameters within the range of the estimate of inaccuracy established with the experts from BASF during the course of the project [Gol14].

The following parameters will be varied:

- Dielectricity constant ε in the interval $[20;\ 30]$
- Double layer capacity C in the interval $[0.05;\ 0.15]$
- Constant deviation of the diffusion coefficient α_{D_i} in the interval $[-0.5 \cdot 10^{-10};\ 0.5 \cdot 10^{-10}]$
- Linear deviation of the diffusion coefficient β_{D_i} in the interval $[-0.05;\ 0.05]$
- Linear deviation of the chemical potentials β_{μ_i} in the interval $[-0.05;\ 0.05]$

For the concentration dependent coefficient functions $f(c)$, the modification will be of the type $\alpha + \beta \cdot f(c)$ with $f \in \{D_i, \mu_i\}$ and $i \in \{Li, PF_6\}$. We do not vary the chemical potential function by a constant, as only its gradient is present in the PNP system, and as such any constant deviation is irrelevant in the scope of this equation system.

To investigate the sensitivity we compute the simple Pearson correlation matrix and the partial correlation matrix. We chose 1.0 $\frac{mol}{l}$ as basis concentration, as this is on the maximum plateau and a common reference value in the literature. For general interpretation of coefficient matrix results, we would like to point the reader to [HJSS06], and also to [Ans73], where several intriguing examples for misleading correlation values were constructed. With these examples in mind, we will expand our analysis to include partial correlation results which will at least remove the influence from the other varied parameters.

In the following section we turn to variance analysis of the results, in order to quantify the relative strength of the contribution of the different variables, identifying relevant design parameters compared to negligible influences on the measured properties.

Pearson correlation matrix										
	ϵ	C	$\beta_{\mu_{Li}}$	$\beta_{\mu_{PF}}$	$\alpha_{D_{Li}}$	$\beta_{D_{Li}}$	$\alpha_{D_{PF}}$	$\beta_{D_{PF}}$	t^+	Λ
ϵ	1.0									
C	0.0	1.0								
$\beta_{\mu_{Li}}$	0.0	0.0	1.0							
$\beta_{\mu_{PF}}$	0.0	0.0	0.0	1.0						
$\alpha_{D_{Li}}$	0.0	0.0	0.0	0.0	1.0					
$\beta_{D_{Li}}$	0.0	0.0	0.0	0.0	0.0	1.0				
$\alpha_{D_{PF}}$	0.0	0.0	0.0	0.0	0.0	0.0	1.0			
$\beta_{D_{PF}}$	0.0	0.0	0.0	0.0	0.0	0.0	0.0	1.0		
t^+	1.1_{-6}	4.1_{-18}	0.0	0.0	5.4_{-1}	1.8_{-1}	-8.0_{-1}	-1.8_{-1}	1.0	
Λ	1.4_{-2}	5.1_{-19}	0.0	0.0	6.8_{-1}	2.2_{-1}	6.8_{-1}	1.5_{-1}	-1.7_{-1}	1.0

Table 5.13: Pearson correlation matrix of input and output parameters. The subscript denotes the exponent of scientific notation to the base 10.

Correlation Matrices

Following [HD00], the entries of the Pearson correlation matrix will be computed by

$$Corr(x,y) = \frac{\sum_i (x_i - \langle x \rangle)(y_i - \langle y \rangle)}{\sqrt{\sum_i (x_i - \langle x \rangle)^2 \sum_i (y_i - \langle y \rangle)^2}}.$$

The partial correlation indizes can be computed from these values by regression as decribed in [HJSS06]. Both provide a measure for the strenght of the linear relation between the respective variables. The partial correlation accounts for correlations between the other involved variables and removes these influences in order to have the pure relation between the variables for which the partial relation is computed.

The results in table 5.13 give clear indication of independence of both – conductivity Λ and transference number t^+ – of the chemical potential parameters β_{μ_i}. While the correlation with the capacitance C is non-zero, the low magnitude of the coefficients allows the same conclusion for this variable. The coefficients for the dielectricity ε and diffusion scaling parameters β_{D_i} similarly suggest a non-relation, however given the variation of multiple variables at the same time, this is inconclusive from the Pearson correlation alone. Similarly, the constant additions to the diffusion parameters α_{D_i} indicate a relation to conductivity and transference number, but here the values are small enough to warrant suspicion.

When checking the results from the partial correlation in table 5.14, the previous suspicion is proved justified in all three instances. The results indicate a close to linear

Partial correlation matrix		
	t^+	Λ
ϵ	$1.26124 \cdot 10^{-5}$	$9.87690 \cdot 10^{-1}$
C	$4.87601 \cdot 10^{-17}$	$2.29721 \cdot 10^{-16}$
$\beta_{\mu_{Li}}$	0.0	0.0
$\beta_{\mu_{PF}}$	0.0	0.0
$\alpha_{D_{Li}}$	$9.88396 \cdot 10^{-1}$	$9.99995 \cdot 10^{-1}$
$\beta_{D_{Li}}$	$9.05353 \cdot 10^{-1}$	$9.99950 \cdot 10^{-1}$
$\alpha_{D_{PF}}$	$-9.94589 \cdot 10^{-1}$	$9.99995 \cdot 10^{-1}$
$\beta_{D_{PF}}$	$-9.05586 \cdot 10^{-1}$	$9.99893 \cdot 10^{-1}$

Table 5.14: Partial correlation matrix between input and output.

correlation from the respective changes in the diffusion coefficients α_{D_i} and β_{D_i} with both the values of the conductivity Λ and the transference number t^+. The change of sign for the correlation of the PF_6 compared to the Li diffusion coefficient is expected, as a higher mobility of the PF_6 ions increases their relative contribution to the current and equivalently reduces the Li contribution. While we notice that the dielectricity ε does have an almost linear correlation with the conductivity Λ, this does not hold for the transference number t^+. Furthermore, the values of the double layer capacitance C and the chemical potential β_{μ_i} do not show evidence of a linear correlation, also confirming the results of the simple correlation matrix.

Analysis of Variance

In addition to analyzing the correlations between the input and output values, which only catch linear dependencies, we perform variance-based decomposition in order to determine the sensitivity of the output to changes in the various input values and check for indications of non-linear correlations.

We compute two parameters, the so-called Sobol indizes, the "main effect sensitivity" S_i and "total effect index" T_i, compare [ABB+13a, ABB+13b] and for additional information and interactions of higher order [TIE10]. Both indices measure the proportion of the variance in the simulated result which stems from the variation of the corresponding parameter with index i. The value S_i determines the influence of the variable i by itself, while T_i determines the influence of i in connection with other

Conductivity		
S_i (main effect sensitivity)	T_i (total effect index)	
$1.880 \cdot 10^{-3}$	$1.902 \cdot 10^{-3}$	ϵ
$3.891 \cdot 10^{-34}$	$4.358 \cdot 10^{-32}$	C
$3.891 \cdot 10^{-34}$	$1.283 \cdot 10^{-31}$	$\beta\mu_{Li}$
$9.727 \cdot 10^{-33}$	$2.361 \cdot 10^{-31}$	$\beta\mu_{PF}$
$4.676 \cdot 10^{-1}$	$4.676 \cdot 10^{-1}$	$\alpha_{D_{Li}}$
$2.276 \cdot 10^{-2}$	$2.276 \cdot 10^{-2}$	$\beta_{D_{Li}}$
$4.592 \cdot 10^{-1}$	$4.592 \cdot 10^{-1}$	$\alpha_{D_{PF}}$
$4.857 \cdot 10^{-2}$	$4.857 \cdot 10^{-2}$	$\beta_{D_{PF}}$

Table 5.15: Sobol indizes of first order for conductivity measurements. Shades of green highlight the parameters with the highest sensitivity values.

variables. The two values are defined by

$$S_i \coloneqq \frac{Var_{\mathbf{x}_i}[E(f(\mathbf{x})|\mathbf{x}_i)]}{Var(f(\mathbf{x}))},$$
$$T_i \coloneqq \frac{E(Var(f(\mathbf{x})|\mathbf{x}_{-i}))}{Var(f(\mathbf{x}))} = \frac{Var(f(\mathbf{x})) - Var(E[f(\mathbf{x})|\mathbf{x}_{-i}])}{Var(f(\mathbf{x}))}.$$

For the sensitivity of the conductivity presented in table 5.15, the two types of Sobol coefficients show very little discrepancy, indicating that higher order interactions will be negligible for the simulation. Indeed, when we compute the Sobol indizes of higher order S_{ij}, their values are several orders of magnitudes smaller than those of the relevant singular indices.[7]

From the values of the indices we learn that constant additions to the diffusion coefficients α_{D_i} result in the strongest influence on the conductivity results, and the impact of the coefficients of both species is approximately the same. The second largest influence from linear scaling of the diffusion coefficients β_{D_i} is roughly an order of magnitude lower, however, here we observe a stronger influence of the variance of the diffusion coefficient of hexafluorophosphate. These two facts indicate that absolute changes of either mobility and not their relation are of importance, as the constant changes of the diffusion coefficients are of the same amount, while the linear scaling is dependent on the original values of the diffusion coefficients, providing a scaling to the actual value of change of the input parameters. Since the main effect sensitivity

[7] The highest value for the interaction of dielectricity ε and $\alpha_{D_{PF}}$ was $1.131 \cdot 10^{-5}$, two orders of magnitude below the singular Sobol indices for the dielectricity and four orders of magnitude lower than the indizes for $\alpha_{D_{PF}}$.

Transference number		
S_i (main effect sensitivity)	T_i (total effect index)	
$2.582 \cdot 10^{-12}$	$2.685 \cdot 10^{-10}$	ϵ
$5.827 \cdot 10^{-34}$	$1.253 \cdot 10^{-32}$	C
$5.827 \cdot 10^{-34}$	$1.188 \cdot 10^{-31}$	$\beta_{\mu_{Li}}$
$1.960 \cdot 10^{-32}$	$2.991 \cdot 10^{-31}$	$\beta_{\mu_{PF}}$
$6.401 \cdot 10^{-1}$	$6.407 \cdot 10^{-1}$	$\alpha_{D_{Li}}$
$3.246 \cdot 10^{-2}$	$3.283 \cdot 10^{-2}$	$\beta_{D_{Li}}$
$2.943 \cdot 10^{-1}$	$2.948 \cdot 10^{-1}$	$\alpha_{D_{PF}}$
$3.217 \cdot 10^{-2}$	$3.254 \cdot 10^{-2}$	$\beta_{D_{PF}}$

Table 5.16: Sobol indizes of first order for the transference number. Shades of green highlight the parameters with the highest sensitivity values.

is based on variance, we compare the ratios of the square roots and find

$$\frac{\sqrt{S_{\beta_{D_{Li}}}}}{\sqrt{S_{\beta_{D_{PF_6}}}}} = 0.685 \approx 0.681 = \frac{D_{Li}}{D_{PF_6}},$$

a relation which which supports the previous conclusion, the variance induced by the scaled contributions relate almost exactly as the original base values of the respective input parameters.

Compared to the diffusion coefficients, the other input variables do not have such a strong influence on the outcome of the simulation. The impact of the dielectricity ϵ of the solvent is reduced by one or respectively two orders of magnitude compared to the diffusion values, but still discernible. The Sobol indizes of the capacitance C and chemical potential parameters β_{μ_i} however indicated that their variations have negligible impact on the simulation results. As a result we conclude that no indications of additional non-linear correlations are present.

Analyzing the variance of the transference number, presented in table 5.16, the values of Sobol indices of higher order S_{ij} are again several magnitudes smaller than those of the singular indices[8], while the main effect sensitivity and total effect index are again numerically similar.

The highest contributions to variance in the transference number are as before the constant additions to the diffusion coefficients α_{D_i}, followed by their respective linear scaling β_{D_i}, again with approximately an order of magnitude lower influence. Opposed

[8] The highest value of impact with $3.549 \cdot 10^{-4}$ is now achieved by the interaction of $\alpha_{D_{Li}}$ and $\beta_{D_{Li}}$, respectively two and three orders of magnitude below the relevant singular indices.

to the conductivity results, the variance analysis indicates that the transference number is dependent on relative changes of the diffusion coefficients: this time the indices for the linear scaling distortion are of the same magnitude, while the indizes of the fixed amount distortions are distinct. As before we compare the ratios of the square roots to find that this time

$$\frac{\sqrt{S_{\alpha_{D_{PF}}}}}{\sqrt{S_{\alpha_{D_{Li}}}}} = 1.474 \approx 1.469 = \frac{D_{Li}}{D_{PF_6}}, \tag{5.2}$$

which supports the above conclusion of the dependence on relative changes. As we are comparing the ratio of the constant distortions, their impact is larger in the value which is originally smaller and vice versa, leading to the fact, that in equation (5.2) the ratios of the diffusion coefficients and their main effect sensitivities are inverted.

All other observed input parameters – dielectricity ε, capacitance C and chemical potential β_{μ_i} – are several orders of magnitude lower in their impact on the output variance and can thus be neglected in comparison to the influence of changes in the diffusion values. As before we conclude that no indications of additional non-linear behavior is present.

Conclusion

The correlation matrices and variance analysis support the assumption that the diffusion coefficients of the species have significant influence on both measured values and that distortions of these parameters lead to significant deviations in the simulation results. In particular, we can derive that the conductivity increases roughly proportional to any increase in ion mobility of either charged particle type. This can be based on the correlation indices being close to one and on the relative magnitude of the sensitivity indizes. For the transference number on the other hand it is not the absolute value but the relation between the diffusion coefficients which is important, a result which can not only be deduced from the plot of the transference numbers vs. the ratio of diffusion coefficients itself, but also from the changing sign of the correlation coefficients and the relative magnitude of the sensitivity indices.

For both types of influence, the absolute and the relative one, we have found that the ratios of the sensitivity almost exactly match the ratio of the diffusion coefficients. In both instances, the ratio supports our previous conclusions about the respective influence of the diffusion coefficients – with either their magnitude or their ratio being important.

From the other observed parameters, only the dielectricity of the solution gives indication to have a limited impact on the conductivity value, while changes in either, the capacitance or the chemical potential values, fail to show evidence of correlation in either investigation method.

Higher order influences which result from interactions between different parameters do not seem to be relevant, which is supported by two observations, first the low magnitude of the higher order indices compared to the singular indices, second the conformity of the respective values of S_i and T_i. Additionally we conclude that apart from the linear correlations identified from the correlation matrizes no other significant non-linear correlations can be determined.

We need to point out that the choice of the parameter intervals was based on estimates and raport with the experimental partners, as the actual magnitude and type of error of the input information was unknown. While it may be possible that deviations in orders of magnitude of the input accuracy estimates may lead to shifts in the relative sensitivity with respect to such parameters, the general sensitivity results obtained here will hold. In particular, as long as the parameters are changed in a way that they scale to the same denormalized equations, the sensitivity derived here will stay identical.

5.5.4 Full Result Tables

Concentration $\left[\frac{mol}{l}\right]$	Conductivity $\left[\frac{S}{cm}\right]$
0	$1.39 \cdot 10^{-6}$
0.1	$3.63 \cdot 10^{-3}$
0.3	$7.49 \cdot 10^{-3}$
0.5	$1.29 \cdot 10^{-2}$
0.7	$1.35 \cdot 10^{-2}$
0.9	$1.52 \cdot 10^{-2}$
1	$1.47 \cdot 10^{-2}$
1.1	$1.55 \cdot 10^{-2}$
1.3	$1.46 \cdot 10^{-2}$
1.5	$1.37 \cdot 10^{-2}$
1.7	$1.34 \cdot 10^{-2}$

Table 5.17: Results of experimental conductivity measurements.

Concentration $\left[\frac{mol}{l}\right]$	Conductivity $\left[\frac{S}{cm}\right]$	Concentration $\left[\frac{mol}{l}\right]$	Conductivity $\left[\frac{S}{cm}\right]$
0.1	$4.36693 \cdot 10^{-3}$	0.925	$1.96616 \cdot 10^{-2}$
0.125	$5.34670 \cdot 10^{-3}$	0.95	$1.96887 \cdot 10^{-2}$
0.15	$6.28220 \cdot 10^{-3}$	0.975	$1.96870 \cdot 10^{-2}$
0.175	$7.17380 \cdot 10^{-3}$	1	$1.96477 \cdot 10^{-2}$
0.2	$8.02220 \cdot 10^{-3}$	1.025	$1.95657 \cdot 10^{-2}$
0.225	$8.82830 \cdot 10^{-3}$	1.05	$1.94571 \cdot 10^{-2}$
0.25	$9.59290 \cdot 10^{-3}$	1.075	$1.93437 \cdot 10^{-2}$
0.275	$1.03171 \cdot 10^{-2}$	1.1	$1.92491 \cdot 10^{-2}$
0.3	$1.10017 \cdot 10^{-2}$	1.125	$1.91930 \cdot 10^{-2}$
0.325	$1.16484 \cdot 10^{-2}$	1.15	$1.91725 \cdot 10^{-2}$
0.35	$1.22592 \cdot 10^{-2}$	1.175	$1.91786 \cdot 10^{-2}$
0.375	$1.28365 \cdot 10^{-2}$	1.2	$1.92000 \cdot 10^{-2}$
0.4	$1.33832 \cdot 10^{-2}$	1.225	$1.92244 \cdot 10^{-2}$
0.425	$1.39023 \cdot 10^{-2}$	1.25	$1.92383 \cdot 10^{-2}$
0.45	$1.43977 \cdot 10^{-2}$	1.275	$1.92273 \cdot 10^{-2}$
0.475	$1.48730 \cdot 10^{-2}$	1.3	$1.91763 \cdot 10^{-2}$
0.5	$1.53325 \cdot 10^{-2}$	1.325	$1.90726 \cdot 10^{-2}$
0.525	$1.57796 \cdot 10^{-2}$	1.35	$1.89153 \cdot 10^{-2}$
0.55	$1.62140 \cdot 10^{-2}$	1.375	$1.87077 \cdot 10^{-2}$
0.575	$1.66342 \cdot 10^{-2}$	1.4	$1.84535 \cdot 10^{-2}$
0.6	$1.70377 \cdot 10^{-2}$	1.425	$1.81485 \cdot 10^{-2}$
0.625	$1.74211 \cdot 10^{-2}$	1.45	$1.78131 \cdot 10^{-2}$
0.65	$1.77810 \cdot 10^{-2}$	1.475	$1.74518 \cdot 10^{-2}$
0.675	$1.81126 \cdot 10^{-2}$	1.5	$1.70640 \cdot 10^{-2}$
0.7	$1.84111 \cdot 10^{-2}$	1.525	$1.70128 \cdot 10^{-2}$
0.725	$1.86717 \cdot 10^{-2}$	1.55	$1.69536 \cdot 10^{-2}$
0.75	$1.88954 \cdot 10^{-2}$	1.575	$1.68906 \cdot 10^{-2}$
0.775	$1.90842 \cdot 10^{-2}$	1.6	$1.68202 \cdot 10^{-2}$
0.8	$1.92407 \cdot 10^{-2}$	1.625	$1.67355 \cdot 10^{-2}$
0.825	$1.93683 \cdot 10^{-2}$	1.65	$1.66403 \cdot 10^{-2}$
0.85	$1.94702 \cdot 10^{-2}$	1.675	$1.65347 \cdot 10^{-2}$
0.875	$1.95506 \cdot 10^{-2}$	1.7	$1.64188 \cdot 10^{-2}$
0.9	$1.96136 \cdot 10^{-2}$		

Table 5.18: Results of conductivity simulations.

Concentration $\left[\frac{mol}{l}\right]$	Transference number	Concentration $\left[\frac{mol}{l}\right]$	Transference number
0.1	0.39915	0.925	0.41858
0.125	0.39692	0.95	0.41376
0.15	0.39470	0.975	0.40888
0.175	0.39258	1	0.40506
0.2	0.39067	1.025	0.40327
0.225	0.38907	1.05	0.40314
0.25	0.38790	1.075	0.40395
0.275	0.38729	1.1	0.40486
0.3	0.38739	1.125	0.40512
0.325	0.38829	1.15	0.40470
0.35	0.38991	1.175	0.40380
0.375	0.39210	1.2	0.40260
0.4	0.39471	1.225	0.40133
0.425	0.39755	1.25	0.40022
0.45	0.40043	1.275	0.39953
0.475	0.40314	1.3	0.39952
0.5	0.40544	1.325	0.40043
0.525	0.40715	1.35	0.40226
0.55	0.40832	1.375	0.40499
0.575	0.40909	1.4	0.40856
0.6	0.40962	1.425	0.41293
0.625	0.41005	1.45	0.41805
0.65	0.41056	1.475	0.42388
0.675	0.41133	1.5	0.43034
0.7	0.41257	1.525	0.42784
0.725	0.41441	1.55	0.42524
0.75	0.41668	1.575	0.42254
0.775	0.41911	1.6	0.41973
0.8	0.42140	1.625	0.41681
0.825	0.42324	1.65	0.41376
0.85	0.42426	1.675	0.41059
0.875	0.42408	1.7	0.40727
0.9	0.42226		

Table 5.19: Results of transference number simulations.

5.6 Complex Geometries with Mixed Boundary Conditions

In this section we will provide a numerical example demonstrating several capabilities of the solver in terms of boundary conditions, different grids for the PNP and the heat equation operator and complex geometries. The geometry of the domain of the ion migration is chosen to be a meandering three-dimensional band, coarsely representing a battery cell which is wrought about its electrodes, compare figure 5.26. The domain of the heat equation is a cuboid set to engulf the domain of the ion species $[-0.1, 1.6] \times [-0.1, 0.4] \times [-0.1, 0.2]$.

For the potential function Φ, the dielectricity is chosen as $\varepsilon_r = 4.0$, the boundary condition on Γ_1 is set to homogeneous Neumann conditions and we set Dirichlet boundary conditions on Γ_2 with a value of $\Phi_{\Gamma_2} = 0.0$ and on Γ_3 with $\Phi_{\Gamma_3} = 0.1$. The division of the boundary in $\Gamma_1 \cup \Gamma_2 \cup \Gamma_3$ is depicted in figure 5.26. The parameter settings for the concentration functions are summarized in table 5.20.

For the heat equation we set the thermal diffusivity to $\alpha = 5.8 \cdot 10^{-6}$. The coupling between the Poisson-Nernst-Planck system and the heat equation is defined by

$$\beta = \sum_i c_i |\nabla \Phi|^2,$$

corresponding to the upscaled energy contributions of the convective ion current as introduced in section 3.5.1. The initial temperature was set to 300.

The boundary conditions for the thermal system are assigned for each planar surface, which we indicate by the respective direction in table 5.21. Robin boundary conditions are set according to the combination of Fourier's law of conduction with Newton's law of cooling [Gre14]

$$-\alpha \cdot \nabla T = -a \cdot (T - T_{env}),$$

which can easily be matched to our equation (4.25), where we uniformly set $a = 1$.

Prior to the actual simulation, we adaptively refined the grid of the PNP operator twice, in each step refining 15% of the cells. Effectively this results in a doubling of the degrees of freedom in each refinement step, with the final number of degrees of freedom amounting to 61705 for the Poisson-Nernst-Planck system interpolated by Finite Element functions of degree one and to 19929 for the thermal system, interpolated by Finite Element functions of degree two. Neither the timestep nor the temperature grid were changed in that procedure. The simulation time was 100 units of time with $\delta t = 0.25$.

The results show that the concentration functions and the electric potential almost immediately reach a steady state. From the snapshots collected in figure 5.27 we see that the combination of boundary conditions plays a role on the concentration behavior, as all species show a reduction of concentrations towards boundary Γ_2, but only

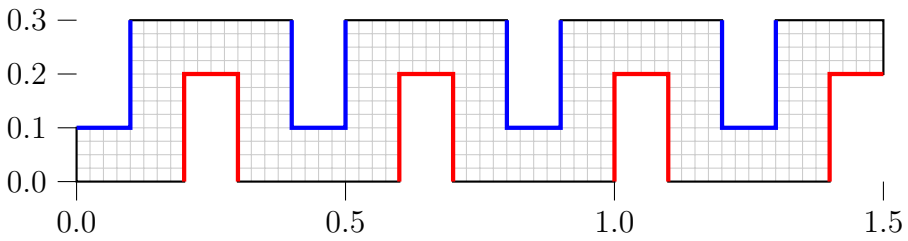

Figure 5.26: 2d projection of basic grid and boundary conditions prior to adaptive refinement: Γ_1 in black, Γ_2 in blue and Γ_3 in red. In x_3-direction the structure extends by 0.1 and is equivalently refined.

Property	Species 0	Species 1	Species 2	Species 3
Charge	$+1$	-1	-2	$+1$
Diffusion coefficient	$1.0 \cdot 10^{-10}$	$1.0 \cdot 10^{-10}$	$2.0 \cdot 10^{-10}$	$5 \cdot 10^{-10}$
Initial concentration	1.0	1.0	0.75	1.5
BC on Γ_1	0.0	0.0	0.0	0.0
BC on Γ_2	0.98_{D}	0.0	0.7_{D}	$1.0 \cdot 10^{-7}$
BC on Γ_3	1.02_{D}	0.0	$-1.0 \cdot 10^{-7}$	1.5_{D}

Table 5.20: Properties of the species used in the complex geometry. Boundary conditions marked with the subscript "$_{\mathrm{D}}$" are of Dirichlet type, all other boundary conditions are of natural type as described in section 4.3.4.

Boundary	Direction	Type	Value
BC on Γ_1	Left	Dirichlet	305
BC on Γ_2	Right	Robin	295
BC on Γ_3	Bottom	Robin	300
BC on Γ_4	Top	Neumann	0
BC on Γ_5	Front	Robin	295
BC on Γ_6	Back	Neumann	0

Table 5.21: Boundary conditions for the heat equation.

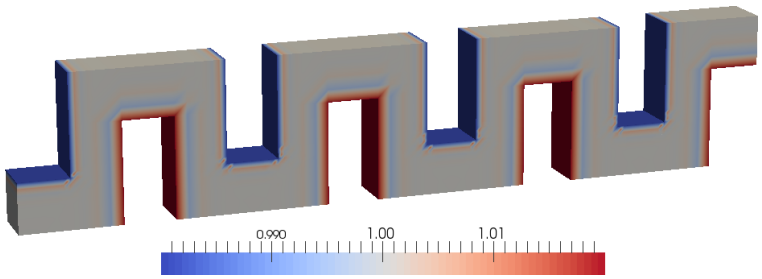

(a) Species 0

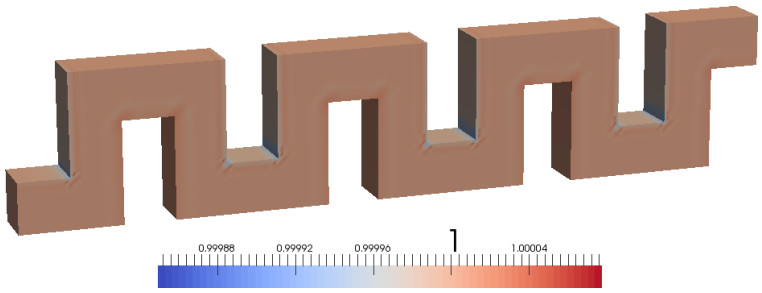

(b) Species 1

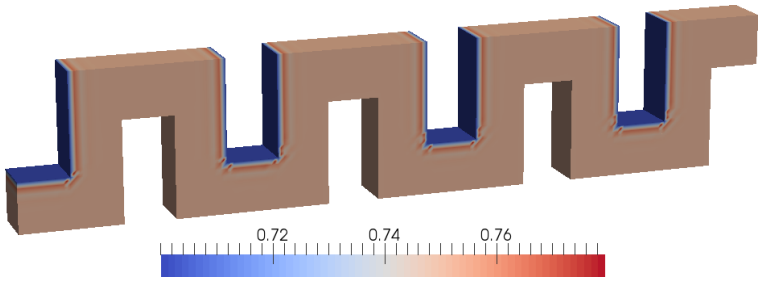

(c) Species 2

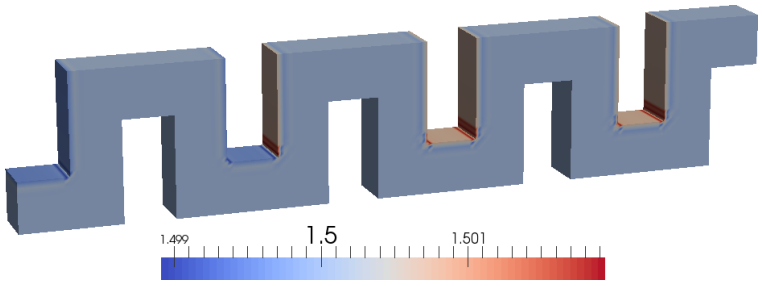

(d) Species 3

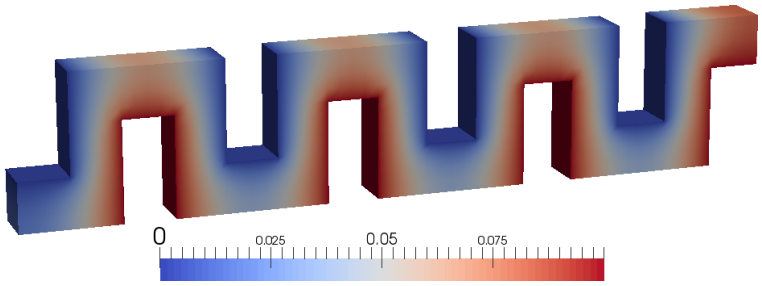

(e) Electric potential

Figure 5.27: Concentration functions and potential function at timestep 20.

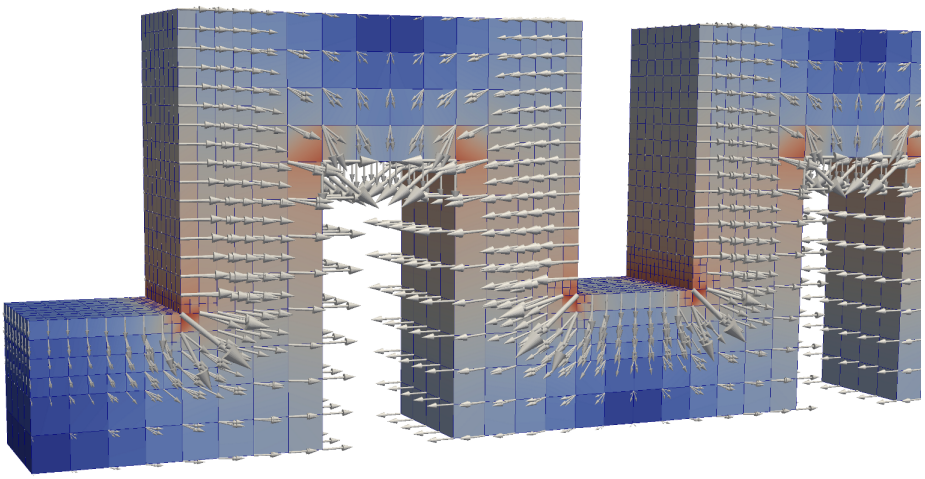

Figure 5.28: Simulated ion flux of species 0. The magnitude of the glyphs is color-coded on the surface of the geometry. The ion flux of the remaining three species follows the same characteristic behavior.

the species with index 0 an equivalent increase towards boundary Γ_3. The remaining three species display the same values as on the interior. While the concentrations appear uniform throughout the interior of the domain, this is not the case for the flux. In figure 5.28 we see that the ion flux is driven by the boundaries Γ_2 and Γ_3 and assumes its highest bulk magnitude between the directly opposing faces of these boundaries, which is expected behavior.

Similarly expected is the behavior of the temperature, the dynamics of which are closely tied to the magnitude of the total flux, see figure 5.29. Initially the temperature is evenly distributed, with the small variations of the temperature introduced by the different boundary conditions, as can be seen by the heating on the right side and the cooling of the front ledge. As the simulation time goes on however, the temperature generated by the ion current in the interior of the domain becomes more dominant. We can easily see in the figures, that the temperature increase is sourced in the domain of the ion migration simulation. Indeed, the heat is not generated uniformly in this domain, but instead there are hotspots and areas with lesser heating. In accordance with our expectations from the source term set for the heat equation, the areas which show the largest increase in temperature correspond to those areas, where the ion flux assumes its highest magnitude, compare figure 5.28 and 5.29. Nevertheless the nature of the boundary conditions continues to play an important role for the characteristics of the temperature solution, as can be seen in figure 5.30. The Robin boundary conditions introduce a cooling effect proportional to the difference to their base magnitude towards their respective direction, whereas the Neumann boundary conditions act as an insulator on their side.

This simulation impressively demonstrates many capabilities of our numerical solver

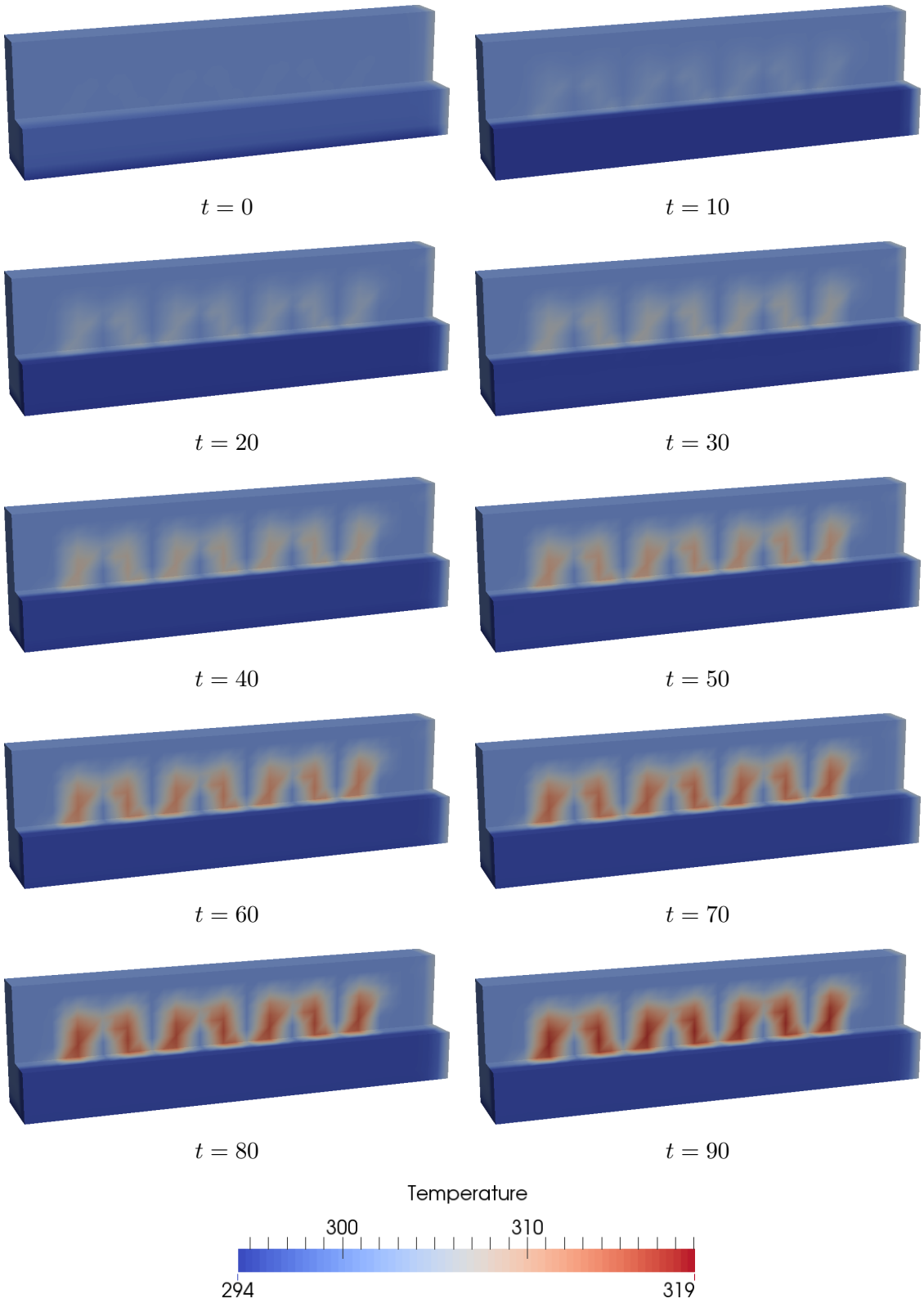

Figure 5.29: Isometric half section of the temperature distribution.

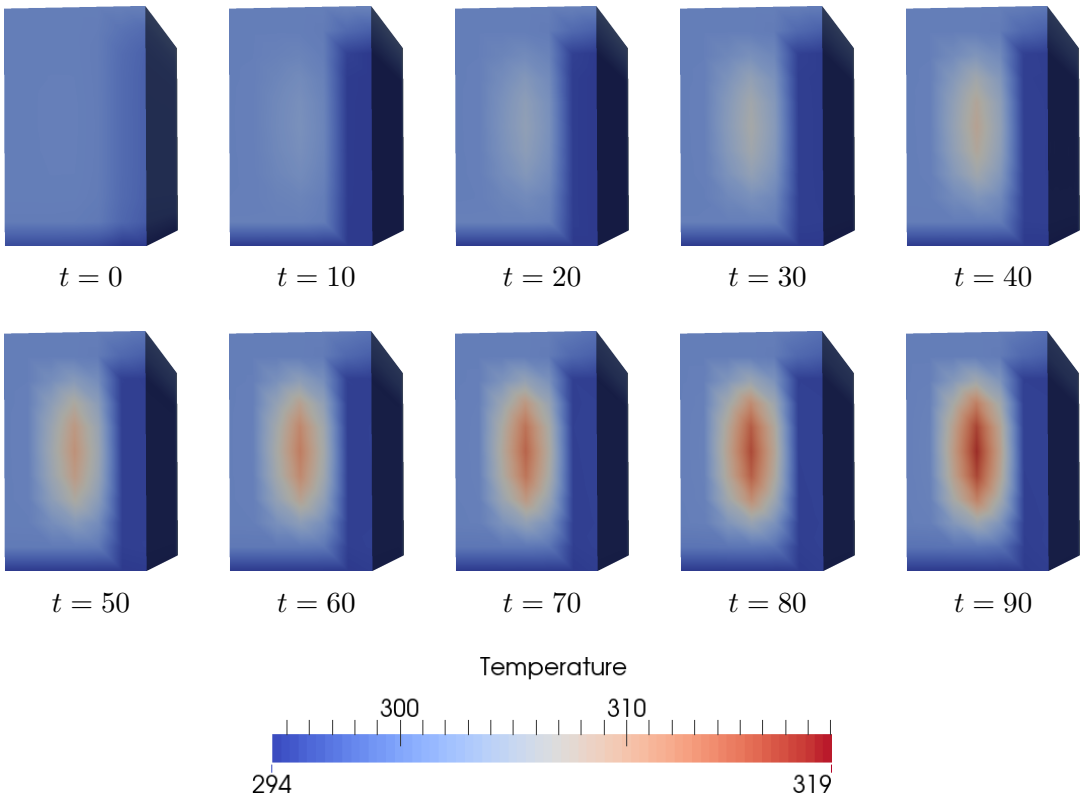

Figure 5.30: Side half section of the temperature distribution.

which have not been included in the previous ensembles. First and foremost it shows the independent treatment of more than two species and the simulation of the combined system on a domain with three-dimensional structure. Furthermore, we demonstrate the handling of several different types of boundary conditions in varying combinations, both for the Nernst-Planck equation, where they may vary for each species and each boundary independently, but also for the heat equation.

The solution of the heat equation clearly shows that the non-linear coupling is transferred among the two different domains and that our approach resolves the local interdependencies very well. The generated heat from the ion migration domain is then transported beyond the confinement of this domain by the heat diffusion. It is exactly this characteristic which we aim for, the ability to identify locally confined buildups of heat which may not only influence the process of ion migration, but have an impact on other surrounding systems.

6 Conclusion

The goal of this thesis was to extend the available tools of numerical simulation to deepen the understanding of ion migration with specific focus on non-equilibrium properties and dynamic temperature development. Towards this end, we treated the simulation of ion migration as a multiscale problem, with particle dynamics on the atomistic scale and with the Heat-Poisson-Nernst-Planck system on the continuous scale. A particular focus of our discussions was placed on the non-equilibrium nature of the thermodynamics involved and on our new approach to simulating the correlation of external forces with the ion flux and the ion flux with the heat generation, which had not been investigated in the literature so far.

We began with the introduction of Molecular Dynamics simulations and their relation to physical systems via macroscopic variables. In particular, we discussed existing non-equilibrium settings and the missing inclusion of external forces in Hamiltonian functions for settings with periodic boundary conditions. In order to address this challenge, we used the duality between a change in potential energy and the work performed on a particle to modify the Hamiltonian function which determines the equations of motion of the particle ensemble. Our approach allowed for the derivation of Hamiltonian equations of motions with external forces and furthermore for the quantification of the external energy transferred into the ensemble. Additionally, external forces modeled with these modifications can be included in various state-of-the-art non-equilibrium ensembles. In particular, we demonstrated the conformity with traditional thermostats and the Parinello barostat.

Following our introduction of the microscale computations we turned to the upscaling of macroscopic variables from the Molecular Dynamics simulations. Besides matching the microstate equations of motion with the macroscale equations and presenting upscaling functions for transport coefficients, which account for non-equilibrium effects, we built on the external energy formulation of the microscale and provided error estimates for the measurement of convection velocities and the transferred external energy. Since this energy is equivalent to a heat transfer we discussed the upscaling of heat and temperature generation within the ensemble and the possibility of steady state detection by comparing the energy transferred from external forces with the energy exchanged with thermostats.

With formulas to compute macroscopic variables from the microscale at our disposal, we turned to the macroscale, where the physical processes are described by partial differential equations. We discussed the modeling of ion migration and temperature dynamics via the Heat-Poisson-Nernst-Planck equation system and intro-

duced a discretized numerical solver based on the Finite Element method which for the first time can treat the coupling of an arbitrary number of ionic species driven by an electrochemical field together with dynamic temperature. We varied the numerical treatment of the equations of the system with the nature of the coupling between the equations, as such the Nernst-Planck equations and Poisson equation were combined into a single operator and treated fully implicitly, while the treatment of the heat equation was achieved by adding a separate operator explicitly coupled to the system.

After these theoretical considerations, we presented several numerical test cases. On the microscopic scale we performed a series of increasingly complex experiments, demonstrating the almost exact quantitative fit of the theoretical predictions in the simple cases and the predicted increasing friction and disturbance of the macroscopic variables with stronger and more complex particle interactions. We demonstrated the different behavior in energy conservation of two variants of implementation. We found that the simulation of physical ensembles encounters several challenges, with typical external forces being several orders of magnitude below the magnitude of internal forces and the high self-diffusion of the electrolyte matrix leading to large a priori error bounds on the estimate of external energy. Nevertheless, the total energy was conserved in all instances and we demonstrated the functionality of the procedure with idealized electrolytes, where the disturbances of the macroscopic values are still small compared to the global trend.

The numerical experiments on the macroscale were begun with an investigation of the conditions of the linear systems created by the discretized operator. We found that the condition numbers vary extremely depending on the input parameters and that input parameters from a typical physical system generate badly conditioned linear systems. We then demonstrated that our numerical solution is able to achieve lower residual values than certain analytical approximations, before producing extensive studies of the convergence behaviors of the solution functions. We found standard convergence rates for uniform refinement of the Finite Element grids and equivalent refinement of the time discretization for both the Poisson-Nernst-Planck and the heat operator. We further improved these results by discussing graded grids, dismissing a misleading naive grading approach which only provided refinement on the boundary. Using an improved grading function, which also expends refinement on the interior, actual convergence can be achieved, which – while not giving exponential rates – still achieves higher rates than those of uniform refinement with far lower numbers of degrees of freedom required. These results were also compared to adaptive refinement, finding the rate of error reduction to be similar, albeit with the adaptive treatment requiring higher computational costs to create the refinement.

While up to this point the studies were artificially constructed for numerical investigations, we continued with an industrial application aiming at ion conductivity in battery settings. There we successfully compared our numerical with experimental results and found them to be in very good agreement. Additionally, we used this setting for a parameter study in the physical relevant regime, identifying the input

parameters which hold the largest quantitative influence on the derived results of conductivity and transference numbers.

We finished the section with a demonstration of additional capabilities of our solver, simulating a complex three-dimensional geometry with non-matching grids for the Poisson-Nernst-Planck operator and the heat equation. The example serves as a showcase for a variety of mixed boundary conditions with several species where we observe that the combination of boundary conditions has a significant impact on the characteristics of the solution functions. Furthermore, we are able to demonstrate successful non-linear coupling from the solutions of the Poisson-Nernst-Planck system to the heat equation across the different grids, fullfilling the final step of our original objective to simulate the dispersion of locally generated heat to regions outside medium of ion transport.

In summary, the methods developed in this thesis close a gap in the connection of the physical modeling of ion migration and temperature dynamics, both on the atomistic and the continuous scale. The methods on the atomistic scale are not restricted to this particular application but open up the analysis and quantification of external energy exchanges for any instance of non-equilibrium Molecular Dynamics. On the macroscale we have provided a tool for the simulation of physical ion migration and temperature systems, which allow for the joint analysis of these connected processes and may ultimately lead to the establishment of increased performance and safety parameters for batteries and other technical systems involving these mechanisms.

6.1 Outlook

The novel approaches presented in this thesis open many opportunities for additional research.

While we have considered our new Hamiltonian formulation for external forces mainly with respect to ion migration, it may certainly be employed in other applications as well. In continuation of our work in this thesis, further groundwork may include to check for the compatibility of the method with additional non-equilibrium Hamiltonian approaches, e.g. with additional types of thermo- and barostats.

The error estimate we presented for the macroscopic value of external energy does not explicitly depend on the number of particles. Nevertheless, it is reasonable to expect from the ergodic theory that the measurements improve by increasing the sampling size. Thus we suggest additional studies to quantify this dependence and we point out that similar studies could be performed for the diffusion coefficient and the dependency of its error estimate on the sampling over time.

During our microscale simulations, we found the computed evolution of the external and kinetic energy in excellent agreement with the prior predictions during the idealized ensembles. Nevertheless, with increasingly complex interactions we noticed growing energy fluctuations, which culminated in the ensemble filled with realisticly

modelled ethylene carbonate. For the method to be suitable for a wide variety of applications instead of a narrow niche, smoothing of the internal energy fluctuations is desirable. The smooth behavior of the variables in the idealized cases suggest that a remedy could be found with reduced models. Mean field approaches, which have been found to allow for successful computations of static macroscopic variables, may permit an ansatz to remove the random disturbances of complex electrolytes and as an additional benefit increase the speed of the computation, see e.g. [Jag07].

On the macroscopic scale, the system of the Heat-Poisson-Nernst-Planck equation as it was derived in this thesis could be extended over its spatial boundaries. Thinking from the perspective of the application, the electrodes encompassing the electrolyte are substantial for the performance of a battery and the intercalation of the ions in the electrodes may have a feedback on the properties in our current simulation domain by providing heat sources and – depending on the material – influencing the simulation domain itself. Furthermore, the material around the cell is modeled with its thermal diffusivity in the heat equation only. By incorporating the intercalation reactions in the electrodes, the sources or sinks of heat could be extended as well, making the model of the thermal dynamics even more accurate.

A seemingly more ambitious endeavour would be the goal to remove the need for the full implicit coupling of the Poisson-Nernst-Planck operator, as the iterative treatment is responsible for much of the computation time. While explicitly restricted to two dimensional systems, the work done by [MG14] might serve as a starting position for a semi-implicit approach to general systems.

Both of the methods here open up new possibilities in material sciences, on the one hand by quantifying heat generation from the ionic fluxes, which enable the creation of a thermal database, and on the other hand by investigating the thermal diffusion and feedback in ion conducting materials in complex setups, identifying critical heat levels which may lead to thermal runaway. Extensive studies of the behavior and the sensitivity of parameters – as demonstrated for an industrial application in section 5.5 – may allow for novel insights for engineers, which may lead to an improvement of the properties and reliability of current applications.

A Implementation Notes on Energy Computation with External Forces

In section 2.3 we have remarked that our approach for the handling of external forces will allow us to observe the conservation of total energy in the context of energy transferred from the exterior of the system. This conservation is based on the assumption that the change of energy of the particles in the external system and internal system are balanced. While this is the case for the continuous trajectories, we need to pay attention in the case of the discretized trajectories.

In the following we will present pseudocode for two different schemes to compute the external energy from the discretized system. The first is subject to a leapfrog shift in the computed energy values which are a half step ahead of the physical energy values. The second approach removes the leapfrog shift, keeping the total of internal and external energy constant at all times.

First Scheme: Energy Leapfrog

The general sequence of events for the first scheme is

- Update x_i and v_i with F_i^n, F_i^{n-1}, ...
- Update all forces $F^n \to F^{n+1}$.
- Update x_i and v_i with F_i^{n+1}, F_i^n, ...
- Update external energy $E_{ext,i}^{n+1} = E_{ext,i}^n + \delta t \cdot v_i^{n+1} F_{ext,i}^{n+1}$.

We also present the specific updates for the Velocity-Störmer-Verlet algorithm

$$
\begin{aligned}
x_i^{n+1} &= x_i^n + \delta t v_i^n + \frac{\delta t^2}{2m_i} F_i^n \\
F_i^{n+1} &= \nabla_i U(x_1, \ldots, x_n) + F_{ext,i}^{n+1} \\
v_i^{n+1} &= v_i^n + \frac{\delta t}{2m_i} \left(F_i^{n+1} + F_i^n \right) \\
E_{ext,i}^{n+1} &= E_{ext,i}^n + \delta t \cdot v_i^{n+1} F_{ext,i}^{n+1}.
\end{aligned}
$$

Second Scheme: Energy Balanced

The general sequence for the balanced external energy update is

- $E_{ext,i}^{n+\frac{1}{2}} = E_{ext,i}^{n+1} + \frac{\delta t}{2} \cdot v_i^n F_{ext,i}^n$.
- Update x_i and v_i with F_i^n, F_i^{n-1}, ...
- Update all forces $F^n \to F^{n+1}$.
- Update x_i and v_i with F_i^{n+1}, F_i^n, ...
- $E_{ext,i}^{n+1} = E_{ext,i}^{n+\frac{1}{2}} + \frac{\delta t}{2} \cdot v_i^{n+1} F_{ext,i}^{n+1}$

We also present the specific updates for the Velocity-Störmer-Verlet algorithm

$$
\begin{aligned}
E_{ext,i}^{n+\frac{1}{2}} &= E_{ext,i}^{n+1} + \frac{\delta t}{2} v_i^n F_{ext,i}^n \\
x_i^{n+1} &= x_i^n + \delta t v_i^n + \frac{\delta t^2}{2m_i} F_i^n \\
F_i^{n+1} &= \nabla_i U(x_1, \ldots, x_n) + F_{ext,i}^{n+1} \\
v_i^{n+1} &= v_i^n + \frac{\delta t}{2m_i} \left(F_i^{n+1} + F_i^n \right) \\
E_{ext,i}^{n+1} &= E_{ext,i}^{n+\frac{1}{2}} + \frac{\delta t}{2} \cdot v_i^{n+1} F_{ext,i}^{n+1}.
\end{aligned}
$$

A comparison of the results achieved with these two methods can be seen in section 5.1.1. Apart from the Velocity-Störmer-Verlet algorithm we have successfully tested the method for Beeman type integrators up to fifth order and iterative velocity Beeman algorithms.

Bibliography

[ABB+13a] Adams, B. M., L. E. Bauman, W. J. Bohnhoff, K. R. Dalbey, M. S. Ebeida, J. P. Eddy, M. S. Eldred, P. D. Hough, K. T. Hu, J. D. Jakeman, L. P. Swiler, and D. M. Vigil: *DAKOTA, A Multilevel Parallel Object-Oriented Framework for Design Optimization, Parameter Estimation, Uncertainty Quantification, and Sensitivity Analysis: Version 5.4 Theory Manual.* Sandia National Laboratories, 2011. Updated November 2013.

[ABB+13b] Adams, B. M., L. E. Bauman, W. J. Bohnhoff, K. R. Dalbey, M. S. Ebeida, J. P. Eddy, M. S. Eldred, P. D. Hough, K. T. Hu, J. D. Jakeman, L. P. Swiler, and D. M. Vigil: *DAKOTA, A Multilevel Parallel Object-Oriented Framework for Design Optimization, Parameter Estimation, Uncertainty Quantification, and Sensitivity Analysis: Version 5.4 User's Manual.* Sandia National Laboratories, December 2009. Updated November 2013.

[Ans73] Anscombe, F. J.: *Graphs in statistical analysis.* The American Statistician, 27(1):17–21, 1973.

[AT89] Allen, M. P. and D. J. Tildesley: *Computer simulation of liquids.* Oxford University Press, 1989.

[AW57] Alder, B. J. and T. E. Wainwright: *Phase Transition for a Hard Sphere System.* Journal of Chemical Physics, 27(5):1208–1209, 1957.

[AW59] Alder, B. J. and T. E. Wainwright: *Studies in Molecular Dynamics. I. General Method.* Journal of Chemical Physics, 31(2):459–466, 1959.

[BAS] BASF SE: *We create chemistry for a sustainable future.* `https://www.basf.com/en/company/about-us.html`. Accessed: April 12th 2016.

[BEC93] Baranyai, A., D. J. Evans, and E. G. D. Cohen: *Field-Dependent Conductivity and Diffusion in a Two-Dimensional Lorentz Gas.* Journal of Statistical Physics, 70(5–6):1085–1098, 1993.

[Ber05] Bernstein, D.: *Simulating mesoscopic reaction-diffusion systems using the Gillespie algorithm.* Physical Review E, 71(4):041103, 2005.

[BHK07] Bangerth, W., R. Hartmann, and G. Kanschat: *deal.II – A General-Purpose Object-Oriented Finite Element Library.* ACM Transactions on Mathematical Software (TOMS), 33(4):24, 2007.

[BL07] Bond, S. D. and B. J. Leimkuhler: *Molecular dynamics and the accuracy of numerically computed averages.* Acta Numerica, 16:1–65, 2007.

[BLL99] Bond, S. D., B. J. Leimkuhler, and B. B. Laird: *The Nosé-Poincaré method for constant temperature molecular dynamics.* Journal of Computational Physics, 151(1):114–134, 1999.

[Bol70] Boltzmann, L.: *Über die Beziehung eines allgemeinen mechanischen Satzes zum zweiten Hauptsatze der Wärmetheorie.* In *Kinetische Theorie II*, pages 240–247. Springer, 1970. Originally published 1877 in Sitz.-Ber. Akad. Wiss. Wien (II) 75, 67–73.

[BPT+15] Berhaut, C. L., P. Porion, L. Timperman, G. Schmidt, D. Lemordant, and M. Anouti: *LiTDI as electrolyte salt for Li-ion batteries: Transport properties in EC/DMC.* Electrochimica Acta, 180:778–787, 2015.

[BR03] Bangerth, W. and R. Rannacher: *Adaptive Finite Element Methods for Differential Equations.* Birkhäuser, 2003.

[Bra07] Braess, D.: *Finite elements: Theory, fast solvers, and applications in solid mechanics.* Cambridge University Press, 2007.

[BSMM01] Bronstein, I. N., K. A. Semendjajew, G. Musiol, and H. Mühlig: *Taschenbuch der Mathematik.* Verlag Harri Deutsch, 2001. 5. überarbeitete und erweiterte Auflage.

[CCAO14] Chaudhry, J. H., J. Comer, A. Aksimentiev, and L. N. Olson: *A Stabilized Finite Element Method for Modified Poisson-Nernst-Planck Equations to Determine Ion Flow Through a Nanopore.* Communications in Computational Physics, 15(1):93–125, 2014.

[CCB+95] Cornell, W. D., P. Cieplak, C. I. Bayly, I. R. Gould, K. M. Merz, D. M. Ferguson, D. C. Spellmeyer, T. Fox, J. W. Caldwell, and P. A. Kollman: *A Second Generation Force Field for the Simulation of Proteins, Nucleic Acids, and Organic Molecules.* Journal of the American Chemical Society, 117:5179–5197, 1995.

[CCC+03] Cances, E., F. Castella, P. Chartier, E. Faou, C. Le Bris, F. Legoll, and Turinici G.: *High-order averaging schemes with error bounds for thermodynamical properties calculations by MD calculations.* INRIA Research Report, 4875, 2003.

[CM69] Cuthill, E. and J. McKee: *Reducing the bandwidth of sparse symmetric matrices.* In *ACM '69: Proceedings of the 1969 24th national conference*, pages 157–172. ACM, 1969.

[Coh07] Cohen, E. R.: *Quantities, Units and Symbols in Physical Chemistry.* Royal Society of Chemistry, 2007.

[Dem04a] Demtröder, W.: *Experimentalphysik 1: Mechanik und Wärme.* Springer-Verlag, 2004.

[Dem04b] Demtröder, W.: *Experimentalphysik 2: Elektrizität und Optik.* Springer-Verlag, 2004.

[DH93] Deuflhard, P. and A. Hohmann: *Numerische Mathematik I.* De Gruyter Lehrbuch, 1993.

[DN08] Danilov, D. and P. H. L. Notten: *Mathematical modelling of ionic transport in the electrolyte of Li–ion batteries.* Electrochimica Acta, 53:5569–5578, 2008.

[ECM93] Evans, D. J., E. G. D. Cohen, and G. P. Morriss: *Probability of second law violations in shearing steady states.* Physical Review Letters, 71:2401–2404, 1993.

[ED05] Earl, D. J. and M. W. Deem: *Parallel tempering: Theory, applications, and new perspectives.* Physical Chemistry Chemical Physics, 7(23):3910–3916, 2005.

[EH85] Evans, D. J. and B. L. Holian: *The Nosé-Hoover thermostat.* Journal of Chemical Physics, 83(8):4069–4074, 1985.

[Ehr27] Ehrenfest, P.: *Bemerkung über die angenäherte Gültigkeit der klassischen Mechanik innerhalb der Quantenmechanik.* Zeitschrift für Physik, 45(7–8):455–457, 1927.

[Eid16] Eiden, P.: *Department Materials Modeling – Quantum Chemistry at BASF SE*, 2016. Personal communication.

[EM07] Evans, D. J. and G. P. Morriss: *Statistical Mechanics of Nonequilibrium Liquids.* ANU E Press, 2007.

[ES94] Evans, D. J. and D. J. Searles: *Equilibrium microstates which generate second law violating steady states.* Physical Review E, 50:1645–1648, 1994.

[Fal01] Faller, J.: *Bose-Einstein Condensation in a Dilute Atomic Vapor.* In Lide, D. R. (editor): *A Century of Excellence in Measurements, Standards, and Technology.* CRC Press, 2001.

[Fef00] Fefferman, C. L.: *Existence and smoothness of the Navier-Stokes equation.* The millennium prize problems, pages 57–67, 2000.

[FGJ91] Farrell, P. A. and E. C. Gartland Jr: *On the Scharfetter-Gummel discretization for drift-diffusion continuity equations.* In Miller, J. J. H. (editor): *Computational Methods for Boundary and Interior Layers in Several Dimensions*, volume 1, pages 51–79. Boole Dublin, 1991.

[FS02] Frenkel, D. and B. Smit: *Understanding Molecular Simulation.* Academic Press, 2. edition, 2002.

[Fuh15] Fuhrmann, J.: *Comparison and numerical treatment of generalised Nernst-Planck models.* Computer Physics Communications, 2015.

[Gaj85] Gajewski, H.: *On Existence, Uniqueness and Asymptotic Behavior of Solutions of the Basic Equations for Carrier Transport in Semiconductors.* ZAMM Journal of Applied Mathematics and Mechanics, 65(2):101–108, 1985.

[Gal97] Gale, J. D.: *GULP: A computer program for the symmetry-adapted simulation of solids.* Journal of the Chemical Society, Faraday Transactions, 93(4):629–637, 1997.

[GBR+99] Grandbois, M., M. Beyer, M. Rief, H. Clausen-Schaumann, and H. E. Gaub: *How Strong Is a Covalent Bond?* 283(5408):1727–1730, 1999.

[Ger02] Gerstner, E.: *Second law broken: Small-scale energy fluctuations could limit minaturization.* Nature Online News, 2002.

[GG92] Gajewski, H. and K. Gärtner: *On the iterative solution of van Roosbroeck's equations.* ZAMM Journal of Applied Mathematics and Mechanics, 72(1):19–28, 1992.

[GH06] Griebel, M. and J. Hamaekers: *Molecular Dynamics Simulations of the Mechanical Properties of Polyethylene-Carbon Nanotube Composites.* In Rieth, M. and W. Schommers (editors): *Handbook of Theoretical and Computational Nanotechnology*, volume 9, chapter 8, pages 409–454. American Scientific Publishers, 2006.

[Gil76] Gillespie, D. T.: *A general method for numerically simulating the stochastic time evolution of coupled chemical reactions.* Journal of Computational Physics, 22(4):403–434, 1976.

[Gil77] Gillespie, D. T.: *Exact stochastic simulation of coupled chemical reactions.* Journal of Physical Chemistry, 81(25):2340–2361, 1977.

[GKZC04] Griebel, M., S. Knapek, G. Zumbusch, and A. Caglar: *Numerische Simulation in der Moleküldynamik.* Springer, 2004.

[GLW08] Gravemeier, V., S. Lenz, and W. A. Wall: *Towards a taxonomy for multiscale methods in computational mechanics: building blocks of existing methods.* Computational Mechanics, 41(2):279–291, 2008.

[Gol14] Gollub, C.: *Department Materials Modeling – Quantum Chemistry at BASF SE*, 2014. Personal communication.

[GR94] Großmann, C. and H. G. Roos: *Numerik partieller Differentialgleichungen.* Teubner-Verlag, Stuttgart, 2. edition, 1994.

[Gre14] Greenberg, M. D.: *Ordinary Differential Equations.* Wiley, 2014.

[GRS07] Großmann, C., H. G. Roos, and M. Stynes: *Numerical Treatment of Partial Differential Equations.* Springer, 2007.

[GT09] Golovnev, A. and S. Trimper: *Exact solution of the Poisson–Nernst–Planck equations in the linear regime.* Journal of Chemical Physics, 131:114903, 2009.

[Hac05] Hackbusch, W.: *Theorie und Numerik elliptischer Differentialgleichungen.* Max-Planck-Institut für Mathematik in den Naturwissenschaften, Leipzig, 3. edition, 2005.

[Had99] Hadjiconstantinou, N. G.: *Molecular dynamics simulation with reversible heat addition.* Physical Review E, 59(1):R44, 1999.

[Ham02] Hamaekers, J.: *Ebene-Wellen basiertes, adaptives und paralleles Verfahren für die Dichtefunktionaltheorie.* Diplomarbeit, Institut für Angewandte Mathematik, Universität Bonn, 2002.

[Ham09] Hamaekers, J.: *Tensor Product Multiscale Many-Particle Spaces with Finite-Order Weights for the Electronic Schödinger Equation.* Dissertation, Institut für Numerische Simulation, Universität Bonn, 2009.

[HD00] Helton, J. C. and F. J. Davis: *Sampling-Based Methods for Uncertainty and Sensitivity Analysis.* Technical report, Sandia National Laboratories, 2000. SAND99-2240.

[Her01] Hernández, E.: *Metric-tensor flexible-cell algorithm for isothermal-isobaric molecular dynamics simulations.* Journal of Chemical Physics, 115(22):10282–10290, 2001.

[Her14] Herz, M.: *Mathematical Modeling and Analysis of Electrolyte Solutions.* Dissertation, Erlangen, Friedrich-Alexander-Universität Erlangen-Nürnberg (FAU), 2014.

[HFPH95] Haberlandt, R., S. Fritzsche, G. Peinel, and K. Heinziger: *Molekulardynamik.* Vieweg, 1995.

[HJSS06] Helton, J. C., J. D. Johnson, C. J. Sallaberry, and C. B. Storlie: *Survey of Sampling-Based Methods for Uncertainty and Sensitivity Analysis.* Reliability Engineering & System Safety, 91(10):1175–1209, 2006.

[HRK12] Herz, M., N. Ray, and P. Knabner: *Existence and uniqueness of a global weak solution of a Darcy-Nernst-Planck-Poisson system.* GAMM-Mitteilungen, 35(2):191–208, 2012.

[HTC98] Harvey, S. C., R. K. Z. Tan, and T. E. Cheatham: *The Flying Ice Cube: Velocity Rescaling in Molecular Dynamics Leads to Violation of Energy Equipartition.* Journal of Computational Chemistry, 19(7):726–740, 1998.

[Jag07] Jager, L.: *Fluid density approximation for an implicit solvent model.* Dissertation, Institut für Numerische Simulation, Universität Bonn, 2007.

[Jer85] Jerome, J. W.: *Consistency of semiconductor modeling: an existence/stability analysis for the stationary van Roosbroeck system.* SIAM Journal on Applied Mathematics, 45(4):565–590, 1985.

[KGZB83] Kelly, D. W., J. P. Gago, O. C. Zienkiewicz, and I. Babuska: *A posteriori error analysis and adaptive processes in the finite element method: Part I - Error analysis.* International Journal for Numerical Methods in Engineering, 19:1593–1619, 1983.

[Kub57] Kubo, R.: *Statistical-Mechanical Theory of Irreversible Processes. I. General Theory and Simple Applications to Magnetic and Conduction Problems.* Journal of the Physical Society of Japan, 12(6):570–586, 1957.

[Kub66] Kubo, R.: *The fluctuation-dissipation theorem.* Reports on Progress in Physics, 29:255, 1966.

[LDP08] Lecca, P., L. Dematté, and C. Priami: *Modeling and simulating reaction-diffusion systems with state-dependent diffusion coefficients.* In *Proceedings of World Academy of Science, Engineering and Technology, International Conference on Bioinformatics and Biomedicine*, volume 35, 2008.

[LFJ11] Landstorfer, M., S. Funken, and T. Jacob: *An advanced model framework for solid electrolyte intercalation batteries.* Physical Chemistry Chemical Physics, 13(28):12817–12825, 2011.

[LHMZ10] Lu, B., M. J. Holst, J. A. McCammon, and Y. C. Zhou: *Poisson-Nernst-Planck equations for simulating biomolecular diffusion-reaction processes I: Finite element solutions.* Journal of Computational Physics, 229:6979–6994, 2010.

[Liu05] Liu, W.: *Geometric Singular Perturbation Approach to Steady-State Poisson-Nernst-Planck Systems.* SIAM Journal on Applied Mathematics, 65(3):754–766, 2005.

[Liu09] Liu, W.: *One-dimensional steady-state Poisson-Nernst-Planck systems for ion channels with multiple ion species.* Journal of Differential Equations, 246(1):428–451, 2009.

[LJK+02] Lee, S. I., U. H. Jung, Y. S. Kim, M. H. Kim, D. J. Ahn, and H. S. Chun: *A study of electrochemical kinetics of lithium ion in organic electrolytes.* Korean Journal of Chemical Engineering, 19(4):638–644, 2002.

[LM15] Leimkuhler, B. and C. Matthews: *Molecular Dynamics: With Deterministic and Stochastic Numerical Methods*, volume 39. Springer, 2015.

[LO80] Liszka, T. and J. Orkisz: *The finite difference method at arbitrary irregular grids and its application in applied mechanics.* Computers & Structures, 11(1–2):83–95, 1980.

[Lub08] Lubich, C.: *From Quantum to Classical Molecular Dynamics: Reduced Models and Numerical Analysis.* European Mathematical Society, 2008.

[LWW06] Liu, Z., X. Wu, and W. Wang: *A novel united-atom force field for imidazolium-based ionic liquids.* Physical Chemistry Chemical Physics, 117(8):1096–1104, 2006.

[LZ11] Latz, A. and J. Zausch: *Thermodynamic consistent transport theory of Li-ion batteries.* Journal of Power Sources, 196(6):3296–3302, 2011.

[LZ15] Latz, A. and J. Zausch: *Multiscale modeling of lithium ion batteries: thermal aspects.* Beilstein Journal of Nanotechnology, 6(1):987–1007, 2015.

[LZH+07] Lu, B., Y. C. Zhou, G. A. Huber, S. D. Bond, M. J. Holst, and J. A. McCammon: *Electrodiffusion: A continuum modeling framework for biomolecular systems with realistic spatiotemporal resolution.* Journal of Chemical Physics, 127(13):135102, 2007.

[MAHS+99] Maleki, H., S. Al Hallaj, J. R. Selman, R. B. Dinwiddie, and H. Wang: *Thermal Properties of Lithium-Ion Battery and Components.* Journal of the Electrochemical Society, 146(3):947–954, 1999.

[Map16] Maplesoft, a division of Waterloo Maple Inc.: *Maple, Version 16.02*, 2005–2016. Maple is a trademark of Waterloo Maple Inc.

[MB03] Manzo, M. A. and W. R. Bennett: *Preliminary Evaluations of Polymer-based Lithium Battery Electrolytes Under Development for the Polymer Energy Rechargeable Systems Program.* In *1st International Energy Conversion Engineering Conference (IECEC), Portsmouth, VA*, 2003.

[MB06] Masliyah, J. H. and S. Bhattacharjee: *Electrokinetic and Colloid Transport Phenomena.* John Wiley & Sons, 2006.

[MEA07] Müller, M., P. Erhart, and K. Albe: *Thermodynamics of $L1_0$ ordering in FePt nanoparticles studied by Monte Carlo simulations based on an analytic bond-order potential.* Physical Review B, 76(15):155412, 2007.

[MFG94] Moy, V. T., E. L. Florin, and H. E. Gaub: *Intermolecular Forces and Energies Between Ligands and Receptors.* 266(5183):257–259, 1994.

[MG14] Mirzadeh, M. and F. Gibou: *A conservative discretization of the Poisson–Nernst–Planck equations on adaptive Cartesian grids.* Journal of Computational Physics, 274:633–653, 2014.

[MK02] Majda, A. J. and B. Khouider: *Stochastic and mesoscopic models for tropical convection.* Proceedings of the National Academy of Sciences, 99(3):1123–1128, 2002.

[MKT92] Martyna, G. J., M. L. Klein, and M. Tuckerman: *Nosé-Hoover chains: The canonical ensemble via continuous dynamics.* Journal of Chemical Physics, 97(4):2635–2643, 1992.

[MLK01] Meier, K., A. Laesecke, and S. Kabelac: *A Molecular Dynamics Simulation Study of the Self-Diffusion Coefficient and Viscosity of the Lennard–Jones Fluid.* International Journal of Thermophysics, 22(1):161–173, 2001.

[MNS13] Moučka, F., I. Nezbeda, and W. R. Smith: *Molecular force field development for aqueous electrolytes: 1. Incorporating appropriate experimental data and the inadequacy of simple electrolyte force fields based on Lennard-Jones and point charge interactions with Lorentz–Berthelot rules.* Journal of Chemical Theory and Computation, 9(11):5076–5085, 2013.

[Moo10] Moosbauer, D. J.: *Elektrochemische Charakterisierung von Elektrolyten und Elektroden für Lithium-Ionen-Batterien – Entwicklung einer neuen Messmethode für elektrochemische Untersuchungen an Elektroden mit der EQCM.* Dissertation, Universität Regensburg, 2010.

[MZ83] Machta, J. and R. Zwanzig: *Diffusion in a periodic Lorentz gas.* Physical Review Letters, 50(25):1959, 1983.

[MZRS16] Melcher, A., C. Ziebert, M. Rohde, and H. J. Seifert: *Modeling and Simulation the Thermal Runaway Behavior of Cylindrical Li-Ion Cells – Computing of Critical Parameter.* Energies, 9(4):292, 2016.

[N+16] Neuen, C. *et al.*: *Tremolo-X Manual.* Fraunhofer Institut für Wissenschaftliches Rechnen und Algorithmen SCAI, 2016.

[Nat14] National Transportation Safety Board: *Auxiliary Power Unit Battery Fire, Japan Airlines Boeing 787-8, JA829J*. Washington, DC., 2014.

[NCA+08] Noid, W. G., J. W. Chu, G. S. Ayton, V. Krishna, S. Izvekov, G. A. Voth, A. Das, and H. C. Andersen: *The multiscale coarse-graining method. I. A rigorous bridge between atomistic and coarse-grained models.* Journal of Chemical Physics, 128(24), 2008.

[Neu10] Neuen, C.: *Ein Multiskalenansatz zur Poisson-Nernst-Planck Gleichung - A Multiscale Approach to the Poisson-Nernst-Planck Equation.* Diplomarbeit, Universität Bonn, 2010.

[NGH12] Neuen, C., M. Griebel, and J. Hamaekers: *Multiscale Simulation of Ion Migration for Battery Systems.* In *MRS Proceedings*, volume 1535. Cambridge University Press, 2012.

[NGL+11] Niedzicki, L., S. Grugeon, S. Laruelle, P. Judeinstein, M. Bukowska, J. Prejzner, P. Szczecinski, W. Wieczorek, and M. Armand: *New covalent salts of the 4+ V class for Li batteries.* Journal of Power Sources, 196(20):8696–8700, 2011.

[NMRP13] Neale, C., C. Madill, S. Rauscher, and R. Pomès: *Accelerating Convergence in Molecular Dynamics Simulations of Solutes in Lipid Membranes by Conducting a Random Walk along the Bilayer Normal.* Journal of Chemical Theory and Computation, 9(8):3686–3703, 2013.

[Nos84] Nosé, S.: *A molecular dynamics method for simulations in the canonical ensemble.* Molecular Physics, 52(2):255–268, 1984.

[Nos91] Nosé, S.: *Constant Temperature Molecular Dynamics Methods.* Progress of Theoretical Physics Supplement, 103:1–46, 1991.

[NRLJ10] Neuss-Radu, M., S. Ludwig, and W. Jäger: *Multiscale analysis and simulation of a reaction-diffusion problem with transmission conditions.* Nonlinear Analysis: Real World Applications, 11(6):4572–4585, 2010.

[P+16] Plimpton, S. *et al.*: *LAMMPS user's manual.* Sandia National Laboratory, 2016.

[PJ97] Park, J. H. and J. W. Jerome: *Qualitative properties of steady-state Poisson-Nernst-Planck systems: Mathematical study.* SIAM Journal on Applied Mathematics, 57(3):609–630, 1997.

[PJD+13] Peters, K., C. Jakob, L. Davies, B. Khouider, and A. J. Majda: *Stochastic behavior of tropical convection in observations and a multicloud model.* Journal of the Atmospheric Sciences, 70(11):3556–3575, 2013.

[Pla22] Planck, M.: *Vorlesungen über Thermodynamik.* Walter de Gruyter, 1922.

[PR81] Parrinello, M. and A. Rahman: *Polymorphic transitions in single crystals: A new molecular dynamics method.* Journal of Applied Physics, 52(12):7182–7190, 1981.

[QKB+14] Qomi, M. J. A., K. J. Krakowiak, M. Bauchy, K. L. Stewart, R. Shahsavari, D. Jagannathan, D. B. Brommer, A. Baronnet, M. J. Buehler, S. Yip, *et al.*: *Combinatorial molecular optimization of cement hydrates.* Nature Communications, 5, 2014.

[RH11] Reif, M. M. and P. H. Hünenberger: *Computation of methodology-independent single-ion solvation properties from molecular simulations. IV. Optimized Lennard-Jones interaction parameter sets for the alkali and halide ions in water.* Journal of Chemical Physics, 134(14), 2011.

[Sac88] Sachs, L.: *Statistische Methoden: Planung und Auswertung.* Springer-Verlag, 6. edition, 1988.

[Sal98] Salmon, R.: *Lectures on Geophysical Fluid Dynamics.* Oxford University Press, 1998.

[Sch91] Schwarz, H. R.: *Methode der finiten Elemente: eine Einführung unter besonderer Berücksichtigung der Rechenpraxis.* Teubner, 1991.

[Sch12] Schönke, J.: *Unsteady analytical solutions to the Poisson-Nernst-Planck equations.* Journal of Physics A: Mathematical and Theoretical, 45(45):455204, 2012.

[SDB+13] Shadman Rad, M., D. L. Danilov, M. Bahalha, M. Kazemeini, and P. H. L. Notten: *Adaptive thermal modeling of Li-ion batteries.* Electrochimica Acta, 102:183–195, 2013.

[SE00] Searles, D. J. and D. J. Evans: *The fluctuation theorem and Green–Kubo relations.* Journal of Chemical Physics, 112(22):9727–9735, 2000.

[SK91] Schwetlick, H. and H. Kretzschmar: *Numerische Verfahren für Naturwissenschaftler und Ingenieure, Eine computerorientierte Einführung.* Fachbuchverlag Leipzig, 1991.

[SM97] Souza, I. and J. L. Martins: *Metric tensor as the dynamical variable for variable-cell-shape molecular dynamics.* Physical Review B, 55(14):8733, 1997.

[SM99] Samson, E. and J. Marchand: *Numerical solution of the extended Nernst-Planck model.* Journal of Colloid and Interface Science, 215(1):1–8, 1999.

[SMM98] Soetens, J. C., C. Millot, and B. Maigret: *Molecular Dynamics Simulation of $Li^+BF_4^-$ in Ethylene Carbonate, Propylene Carbonate, and Dimethyl Carbonate Solvents.* Journal of Physical Chemistry, 102(7), 1998.

[SPWS08] Sevick, E. M., R. Prabhakar, S. R. Williams, and D. J. Searles: *Fluctuation Theorems.* Annual Review of Physical Chemistry, 59:603–633, 2008.

[SS86] Saad, Y. and M. H. Schultz: *GMRES: A generalized minimal residual algorithm for solving nonsymmetric linear systems.* SIAM Journal on Scientific and Statistical Computing, 7(3):856–869, 1986.

[SS08] Schröder, K. P. and R. C. Smith: *Distant future of the Sun and Earth revisited.* Monthly Notices of the Royal Astronomical Society, 386(1):155–163, 2008.

[SS15] Samin, A. and V. V. Subramaniam: *Analytical Solutions to the Steady State Poisson-Nernst-Planck Equations in Electrobiochemical Systems.* Applied Physics Research, 7(2):40, 2015.

[SSZL16] Sun, Y., P. Sun, B. Zheng, and G. Lin: *Error analysis of finite element method for Poisson–Nernst–Planck equations.* Journal of Computational and Applied Mathematics, 301:28–43, 2016.

[Sto05] Stoer, J.: *Numerische Mathematik 1.* Springer, 9. edition, 2005.

[TIE10] Tang, G., G. Iaccarino, and M. S. Eldred: *Global Sensitivity Analysis for Stochastic Collocation.* In *Proceedings of the 51st AIAA/ASME/ASCE/AHS/ASC Structures, Structural Dynamics, and Materials Conference (12th AIAA Non-Deterministic Approaches Conference)*, AIAA-2010-2922, 2010.

[TL16] Tveito, A. and G. T. Lines: *Computing Characterizations of Drugs for Ion Channels and Receptors Using Markov Models.* Springer International Publishing, 2016.

[TM11] Tadmor, E. B. and R. E. Miller: *Modeling Materials: Continuum, Atomistic and Multiscale Techniques.* Cambridge University Press, 2011.

[TME12] Tadmor, E. B., R. E. Miller, and R. S. Elliott: *Continuum Mechanics and Thermodynamics: From Fundamental Concepts to Governing Equations.* Cambridge University Press, 2012.

[TTP+12] Taralov, M., V. Taralova, P. Popov, O. Iliev, A. Latz, and J. Zausch: *Report on Finite Element Simulations of Electrochemical Processes in Li-ion Batteries with Thermic Effects.* Scientific Reports of the ITWM, 2012.

[Tuc10] Tuckerman, M.: *Statistical Mechanics: Theory and Molecular Simulation.* Oxford University Press, 2010.

[Two07] Twomey, A.: *On the Stochastic Modelling of Reaction-Diffusion Processes.* Master thesis, University of Oxford, 2007.

[Vas15] Vasyliv, Y. V.: *Development of General Finite Differences for Complex Geometries Using Immersed Boundary Method.* Master thesis, Georgia Institute of Technology, 2015.

[VR05] Valøen, L. O. and J. N. Reimers: *Transport Properties of $LiPF_6$-Based Li-Ion Battery Electrolytes.* Journal of the Electrochemical Society, 152(5):A882–A891, 2005.

[WEL+07] Weinan, E., B. Engquist, X. Li, W. Ren, and E. Vanden-Eijnden: *Heterogeneous multiscale methods: A review.* Communications in Computational Physics, 2(3):367–450, 2007.

[WHHP13] Williard, N., W. He, C. Hendricks, and M. Pecht: *Lessons Learned from the 787 Dreamliner Issue on Lithium-Ion Battery Reliability.* Energies, 6(9):4682–4695, 2013.

[WHWH14] Wang, X. S., D. He, J. J. Wylie, and H. Huang: *Singular perturbation solutions of steady-state Poisson-Nernst-Planck systems.* Physical Review E, 89(2):022722, 2014.

[WSM+02] Wang, G. M., E. M. Sevick, E. Mittag, D. J. Searles, and D. J. Evans: *Experimental Demonstration of Violations of the Second Law of Thermodynamics for Small Systems and Short Time Scales.* Physical Review Letters, 89:050601, 2002.

[ZCW11] Zheng, Q., D. Chen, and G. W. Wei: *Second-order Poisson-Nernst-Planck solver for ion transport.* Journal of Computational Physics, 230(13):5239–5262, 2011.

[ZFA+11] Zugmann, S., M. Fleischmann, M. Amereller, R. M. Gschwind, H. D. Wiemhöfer, and H. J. Gores: *Measurement of transference numbers for lithium ion electrolytes via four different methods, a comparative study.* Electrochimica Acta, 56(11):3926–3933, 2011.

[ZRM09] Zia, R. K. P., E. F. Redish, and S. R. McKay: *Making sense of the Legendre transform.* American Journal of Physics, 77(7):614–622, 2009.

[Zug11] Zugmann, S.: *Messung von Lithium-Ionen Überführungszahlen an Elektrolyten für Lithium-Ionen Batterien.* Dissertation, Universität Regensburg, 2011.